GEORG-AUGUST-UNIVERSITÄT
GÖTTINGEN

Fakultät für
Physik

Master's Thesis

Untersuchung der CP-Natur des Higgs-Bosons in VBF $H \to \tau_{\text{had}}\tau_{\text{had}}$ Zerfällen mit der Optimalen Observablen in 13 TeV Daten

Investigation of the CP nature of the Higgs boson in VBF $H \to \tau_{\text{had}}\tau_{\text{had}}$ decays using the Optimal Observable in 13 TeV data

prepared by

Arthur Linß

from Kassel

at the II. Physikalischen Institut

Thesis number: II.Physik-UniGö-MSc-2017/09

Thesis period: 27th July 2017 until 19th December 2017

First referee: Prof. Dr. Stanley Lai

Second referee: Prof. Dr. Ariane Frey

Abstract

Diese Arbeit präsentiert Sensitivitätsstudien zur CP-Invarianz in der Vektorboson-Fusion Higgs-Boson Produktion mithilfe der Methode der Optimalen Observablen im VBF $H \to \tau_{\text{had}}\tau_{\text{had}}$ Kanal. Die Optimale Observable erster Ordnung $\mathcal{O}_1$ ist eine CP-ungerade Observable und ist damit sensitiv bezüglich CP-ungeraden Kopplungen des Higgs-Bosons zu Vektorbosonen. Diese anormalen Kopplungen können in einer effektiven Feldtheorie durch einen einzelnen Parameter $\tilde{d}$ im Matrixelement parameterisiert werden. Die Berechnung der Optimalen Observablen der ersten und zweiten Ordnung $\mathcal{O}_{1,2}$ aus den Matrixelementen und die Umgewichtung zur Simulation der anormalen Kopplungen werden untersucht. Die erwartete Sensitivität bezüglich $\tilde{d}$ wird duch Monte Carlo Daten mittels Eichkurven und Likelihood Fits abgeschätzt.

Stichwörter: Higgs, Optimale Observable, Eichkurve, Likelihood Fit

Abstract

This thesis presents sensitivity studies of CP invariance in vector boson fusion Higgs boson production using the Optimal Observable in the VBF $H \to \tau_{\text{had}}\tau_{\text{had}}$ channel. The Optimal Observable of first order $\mathcal{O}_1$ is a CP-odd observable and therefore sensitive to CP-odd couplings of the Higgs boson to vector bosons. The anomalous couplings can be parametrised in an effective field theory by a single parameter $\tilde{d}$ in the matrix element $\mathcal{M}$. The calculation of the Optimal Observable of first and second order $\mathcal{O}_{1,2}$ from matrix elements and the reweighting procedure to simulate anomalous couplings are investigated. The expected sensitivity with respect to $\tilde{d}$ is estimated using Monte Carlo data by gauge curves and likelihood fits.

Keywords: Higgs, Optimal Observable, Gauge Curve, Likelihood Fit

Contents

1. Introduction

The Standard Model of particle physics (SM) [1–7] is one of the most successful theories ever developed. It has predicted many phenomena several years before they could be validated experimentally, culminating in the discovery of the Higgs boson [8–10] in 2012 by the ATLAS and CMS collaborations at the LHC [11, 12], roughly 50 years after its theoretical prediction.

The discovery of the Higgs boson was the starting point for several measurements testing the SM and searching for physics beyond the Standard Model (BSM) by comparing the predicted properties of the Higgs boson to experimental data. One important analysis deals with the CP properties of the Higgs boson. The SM predicts a CP-even Higgs boson, while deviations from this might give an explanation of the baryon asymmetry [13] in the observable universe, which is not explained within the SM.

In this thesis, the investigation of a possible anomalous Higgs boson coupling to weak vector bosons in vector boson fusion Higgs boson production is performed in the $H \to \tau_{\text{had}}\tau_{\text{had}}$ decay mode using data recorded with the ATLAS experiment at the LHC in 2015 and 2016 during Run 2 at $\sqrt{s} = 13$ TeV and $L = 36.1$ fb^{-1} using a cut-based approach and the method of the Optimal Observable [14].

An outline of this thesis follows. Chapter two gives an overview of the underlying theory. The third chapter summarises briefly the experimental setup, giving an introduction to the LHC and the ATLAS detector. The fourth Chapter follows describing the used data and Monte Carlo samples and the object definitions. The fifth Chapter presents the event selection and categorisation. In Chapters five and six, the Optimal Observables and the reweighting procedure are investigated for signal and background processes. The sensitivity estimate with respect to $\tilde{d}$, the parameter which describes the CP-nature of the Higgs boson, using gauge curves is described in Chapter eight and a maximum likelihood fit, including systematic uncertainties, is described in Chapter nine. Chapter ten summarises the results and gives an outlook on further studies and possible improvements of the presented analysis.

2. Theoretical Overview

In this chapter a theoretical overview is given. It includes an introduction to the Standard Model of particle physics, electroweak symmetry breaking, the Higgs boson, the Optimal Observable, which is used in the CP analysis of the Higgs boson, and the ATLAS experiment at the LHC.

2.1. Standard Model of Particle Physics

This section gives an introduction to the Standard Model of particle physics and in particular electroweak symmetry breaking.

2.1.1. Particles and Forces

The Standard Model of elementary particle physics (SM) [1–7] describes the elementary particles and their interactions in a relativistic and local-gauge invariant Quantum Field Theory (QFT). The particle content of the SM can be grouped into matter particles, the fermions, and force mediators, the bosons, see Figure 2.1. The elementary fermions of the SM are leptons and quarks, which both occur in three generations. Electrons, muons, τ leptons and the corresponding neutrinos are referred to as leptons. The quarks occur in six different flavours: up, down, charm, strange, top and bottom.

The SM includes three of the four fundamental forces - electromagnetic, strong nuclear and weak nuclear interactions, which are described in renormalizable QFTs [15–17]. The electromagnetic force was the first interaction which was formulated in a QFT, called Quantum Electrodynamics (QED) [18–22]. QED is formulated as an abelian gauge theory with corresponding gauge group $U(1)$. The Lagrangian for a free fermion field with mass m described by a Dirac spinor ψ is given by

$$\mathcal{L}_{QED} = i\overline{\psi}\gamma^{\mu}\partial_{\mu}\psi - m\overline{\psi}\psi, \tag{2.1}$$

where γ^{μ} are the Dirac matrices for $\mu \in \{0, 1, 2, 3\}$ and ∂_{μ} is the derivative with respect to the space-time coordinates x^{μ}. This Lagrangian is invariant under global $U(1)$ gauge

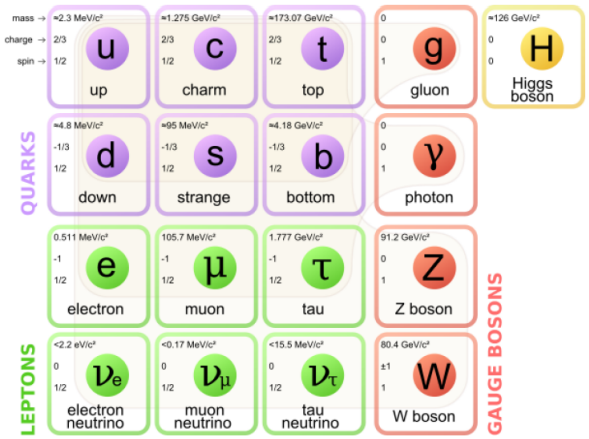

Figure 2.1.: The elementary fermions and force mediators within the SM, leptons and quarks occur in three generations. The gauge vector bosons are the mediators of the three forces described within the SM, which are the $W^{\pm}$ and Z^0 boson of the weak force, the eight gluons g of the strong force and the photon γ of the electromagnetic interaction. Furthermore, there is the Higgs boson, a consequence of the presence of the Higgs field, which in turn is responsible for the masses of the gauge bosons and fermions.

transformations. By replacing the partial derivative ∂_μ by the gauge covariant derivative $D_\mu = \partial_\mu + ieA_\mu$, where A_μ is the gauge field of QED, i.e the photon, which transforms as $A_\mu \rightarrow A_\mu - \frac{1}{e}\partial_\mu \xi$, the Lagrangian $\mathcal{L}_{QED}$ can be transformed into a local gauge-invariant Lagrangian. Therefore, the local gauge-invariant Lagrangian for QED is given by

$$\mathcal{L}_{QED} = i\overline{\psi}\gamma^\mu \partial_\mu \psi - m\overline{\psi}\psi - e\overline{\psi}A_\mu\psi - \frac{1}{4}F^{\mu\nu}F_{\mu\nu}. \tag{2.2}$$

Here, e is the coupling strength in QED and $F_{\mu\nu}$ is the field strength tensor for the gauge field A_μ given by $F_{\mu\nu} = \partial_\mu A_\nu - \partial_\nu A_\mu$. The extension of the global gauge-invariant QED Lagrangian into a local gauge-invariant Lagrangian comes along with an interaction term between the massless gauge field A_μ and the massive spinor field ψ. An additional mass term of the gauge field A_μ would spoil the local gauge invariance of the QED Lagrangian $\mathcal{L}_{QED}$. Therefore, the photon remains massless, which is in accordance with experimental observations.

The strong interaction describes the interaction of particles which carry colour charge, i.e. quarks and gluons. Colour charge occurs in three different orthogonal states, often termed as red, green and blue. While (anti-)quarks carry one (anti-)colour, gluons carry one colour and one anti-colour. Since the eight gluons, the force mediators of strong interactions, carry colour-charges themselves, there is gluon self-interaction. The gauge invariant QFT of strong interactions is called Quantum Chromodynamics (QCD) [7]. The

gauge-invariant Lagrangian of QCD $\mathcal{L}_{QCD}$ is given by

$$\mathcal{L}_{QCD} = i\overline{q}_\alpha(\gamma^\mu D_\mu - m)_{\alpha\beta} q_\beta - \frac{1}{4} G^a_{\mu\nu} G^{\mu\nu}_a, \tag{2.3}$$

with gauge covariant derivative $D_\mu = \partial_\mu + i g_s \frac{\lambda_i}{2} G^i_\mu$, where $G^i_{\mu\nu}$ is the strong gluon gauge field and λ_i are the Gell-Mann matrices. The indices α and β denote the flavour of the quark spinor-field q with mass m in the fundamental representation of $SU(3)$. There is no gluon mass term in the Lagrangian $\mathcal{L}_{QCD}$, which would otherwise spoil the required $SU(3)$ gauge invariance. The energy dependence of $\alpha_s = \frac{g_s^2}{4\pi}$ leads to the phenomena of asymptotic freedom and confinement in QCD, see Section 2.7.4.

The weak interaction is the force responsible for radioactive decays, like the β^--decay. The weak force is the only force which allows a flavour-change for quarks and C as well as CP violation is observed. In contrast to the massless gauge bosons of QED and QCD, experiments show that the force mediators of the weak interaction, the $W^\pm$ and the Z^0 bosons, are massive, which is explained within the SM by the Higgs mechanism, see Section 2.1.2. The behaviour of particles in weak interactions is described by the weak isospin T. Particles are placed in chiral multiplets, which have a different behaviour under $SU(2)$ gauge transformations. Left-handed fermions are placed in weak isospin doublets, with $T^3 = \frac{1}{2}$ for the upper component and $T^3 = -\frac{1}{2}$ for the lower component, while right-handed fermions are placed in weak isospin singlets with $T = 0$, whereby the weak eigenstates of the d, s and b quark are not equal to the mass eigenstates but mixtures of them, described by the CKM matrix [23, 24].

In the 1960s, Glashow, Salam and Weinberg [1–3] developed a theory which unifies the electromagnetic force and the weak interaction, called electroweak unification (EU). The EU is based on the $SU(2)_L \times U(1)_Y$ gauge group. In the EU, the electric charge Q and the third component of the weak isospin T^3 are combined into another quantum number, the hypercharge Y given by $Y = 2(Q - T^3)$. The electroweak Lagrangian $\mathcal{L}_{EW}$, before symmetry breaking and without the terms arising from interactions with the Higgs field, is based on the $SU(2)_L \times U(1)_Y$ gauge symmetry, where L refers to left-handed particles, and can be described by

$$\begin{aligned} \mathcal{L}_{EW} &= \mathcal{L}_{gauge} + \mathcal{L}_{fermions} \\ &= -\frac{1}{4}(W^{\mu\nu}_a W^a_{\mu\nu} + B^{\mu\nu} B_{\mu\nu}) + \overline{Q}_i i \not{D} Q_i + \overline{u}_i i \not{D} u_i + \overline{d}_i i \not{D} d_i + \overline{L}_i i \not{D} L_i + \overline{l}_i i \not{D} l_i, \end{aligned} \tag{2.4}$$

with $\not{D} = \gamma^\mu D_\mu$ and $D_\mu = \partial_\mu + i g W^a_\mu \frac{\sigma^a}{2} + i g' B_\mu \frac{Y}{2}$, where σ^a are the Pauli matrices. The index $a \in \{1, 2, 3\}$ denotes the three gauge fields W^a of $SU(2)$, $B_{\mu\nu}$ is the gauge field

corresponding to $U(1)_Y$, and $i \in \{1, 2, 3\}$ denotes the generations of fermions. The quark fields are Q_i, the left-handed isospin doublets, u_i and d_i, the right-handed singlets up and down, respectively. L_i are the left-handed lepton isospin doublets and l_i the right-handed lepton singlets.

Taking QCD into account, the entire gauge group of the SM is $SU(3)_C \times SU(2)_L \times U(1)_Y$. The Lagrangians of QED, QCD and the weak interaction do not include mass terms of gauge bosons, which would otherwise spoil the required local gauge invariance of the SM. The experimental observed masses of the weak gauge bosons can be achieved within the SM by the Higgs mechanism. Also, the unified description of weak and electromagnetic interactions arises naturally from the Higgs mechanism, which is described in Section 2.1.2.

The SM is very succesful in describing high-energy particle interactions but is not a complete theory that explains the whole universe, as it does not include gravity and cannot explain phenomena like Dark Matter [25], Dark Energy [26], the Hierarchy Problem [27] or the baryon asymmetry [13], which is explained in Section 2.2.2. Therefore, physicists developed theories beyond the SM (BSM) such as Supersymmetry (SUSY) and String Theory.

2.1.2. Electroweak Symmetry Breaking

As mentioned in Section 2.1.1, the SM describes interactions via a local gauge invariant QFT. This symmetry requires the gauge bosons to be massless because otherwise a mass term in the Lagrangian would spoil the required local gauge invariance. This is in contrast to the observed masses of the weak gauge bosons Z^0 and $W^{\pm}$. A solution to this problem was found in 1964 by Brout and Englert [9], Higgs [8] and Guralnik, Hagen and Kibble [10] using the concept of spontaneous symmetry breaking. In case of the $SU(2)_L \times U(1)_Y$ gauge symmetry of the electroweak unification this is called the Brout-Englert-Higgs mechanism or simply the Higgs mechanism. The electroweak theory is based on the $SU(2)_L \times U(1)_Y$ gauge group with four gauge fields - a triplet $W_\mu = (W_\mu^{(1)}, W_\mu^{(2)}, W_\mu^{(3)})$ with coupling constant g_W and B_μ with coupling constant g'. The basic idea to break the electroweak symmetry is to add an additional scalar field, the Higgs field, to the SM-Lagrangian, which has a non-zero vacuum expectation value (VEV) v. In the following, the concept of electroweak symmetry breaking is presented. In order to give mass to the weak gauge bosons using the Higgs mechanism, a complex scalar doublet $\phi(x)$ is introduced, given by

$$\phi(x) = \begin{pmatrix} \phi^+(x) \\ \phi^0(x) \end{pmatrix} = \frac{1}{\sqrt{2}} \begin{pmatrix} \phi_1(x) + i\phi_2(x) \\ \phi_3(x) + i\phi_4(x) \end{pmatrix} \tag{2.5}$$

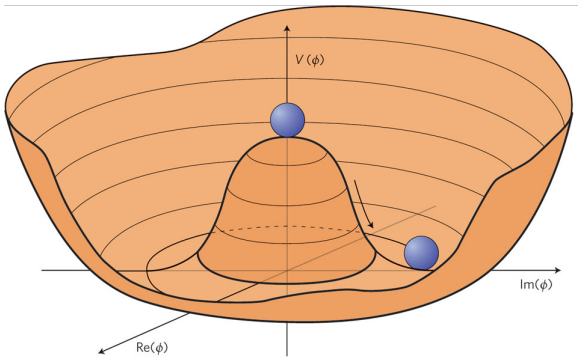

Figure 2.2.: Simplified picture of the Higgs-Potential $V(\phi)$ in the case of $\mu^2 < 0$. This is often called the Mexican hat potential. At the origin there is a unstable maximum. The infinite set of degenerate vacuum states of $V(\phi)$ are located on a circle defined by $\phi^\dagger\phi = -\frac{\mu^2}{2\lambda}$.

with hypercharge $Y_\phi = 1$ and corresponding Lagrangian

$$\mathcal{L} = (D_\mu\phi^\dagger)(D^\mu\phi) - V(\phi) \tag{2.6}$$

with Higgs potential

$$V(\phi) = \mu^2\phi^\dagger\phi + \lambda(\phi^\dagger\phi)^2, \tag{2.7}$$

where λ is a self-coupling parameter and μ is a parameter of mass dimension one. The potential $V(\phi)$ is restricted to this form by $SU(2)_L \times U(1)_Y$ invariance and renormalizability. Vacuum stability requires $\lambda > 0$, corresponding to a potential bounded from below. For $\mu^2 \geq 0$ the potential $V(\phi)$ has a single minimum at $\phi = 0$. For $\mu^2 < 0$, the potential has a local maximum at $\phi = 0$ and an infinite set of minima given by $\phi^\dagger\phi = -\frac{\mu^2}{2\lambda} = \frac{v^2}{2}$, see Figure 2.2, where v is the non-zero VEV of the field given by

$$v^2 = -\frac{\mu^2}{\lambda}. \tag{2.8}$$

Also in Equation (2.6), the covariant derivative

$$D_\mu = \partial_\mu + ig_W\vec{T}\cdot\vec{W}_\mu + \frac{ig'}{2}B_\mu \tag{2.9}$$

is introduced, where W_μ^j and B^μ are the gauge fields of the $SU(2)_L \times U(1)_Y$ gauge symmetry, $T^j = \frac{1}{2}\sigma^j$ are the generators of the $SU(2)$ symmetry group, σ^j are the Pauli matrices, and g_W as well as g' are dimensionless coupling parameters. The covariant derivative D_μ ensures that the Lagrangian in Equation (2.6) respects the local gauge invariance of the electroweak theory. Since after symmetry breaking the photon γ must remain massless,

the VEV must be in the neutral component of the Higgs doublet

$$\langle 0|\phi|0\rangle = \frac{1}{\sqrt{2}}\begin{pmatrix}0\\v\end{pmatrix}. \tag{2.10}$$

This special choice of the vacuum state will break the $SU(2)_L \times U(1)_Y$ symmetry but leaves the gauge group $U(1)$ invariant, resulting in a massless photon. By expanding the Higgs doublet ϕ about the VEV v, setting $\phi_3(x) = v + h(x)$ and using, without loss of generality, the unitary gauge, the Lagrangian of Equation (2.6) offers different mass and coupling terms of the physical fields. The mass terms of the W boson can be identified with

$$\frac{1}{2}m_W^2 W_\mu^{(1,2)} W^{(1,2)\mu}, \tag{2.11}$$

meaning that $m_W = \frac{1}{2}g_W v$ corresponds to the mass of the $W^\pm$ boson, whereby the physical $W^\pm$ boson fields are given by

$$W_\mu^\pm = \frac{1}{\sqrt{2}}(W_\mu^{(1)} \mp iW_\mu^{(2)}). \tag{2.12}$$

Furthermore, the masses of the physical fields Z_μ^0 and A_μ, corresponding to the Z^0 boson and the photon γ, respectively, are given by

$$m_A = 0 \quad m_{Z^0} = \frac{v^2}{2}\sqrt{g_W^2 + g'^2}. \tag{2.13}$$

where the physical fields Z_μ^0 and A_μ are superpositions of the gauge fields, given by

$$\begin{pmatrix}Z_\mu^0\\A_\mu\end{pmatrix} = \begin{pmatrix}\cos\theta_W & -\sin\theta_W\\ \sin\theta_W & \cos\theta_W\end{pmatrix}\begin{pmatrix}W_\mu^{(3)}\\B_\mu\end{pmatrix}, \tag{2.14}$$

where the weak mixing angle θ_W is introduced, defined by

$$\cos\theta_W = \frac{g_W}{\sqrt{g_W^2 + g'^2}} = \frac{g_W}{g_{Z^0}}. \tag{2.15}$$

After symmetry breaking, the part of the Lagrangian in Equation (2.6) containing the Higgs field offers a mass-term and triple as well as quartic self-interaction terms of the Higgs boson. The mass term of the form $\lambda v^2 h^2$ determines the mass of the Higgs boson, given by $m_H = \sqrt{2\lambda}v$. Using the measurements for m_W and g_W, the VEV v of the Higgs field is determined to $v = 246$ GeV, which defines the weak energy scale. Since the self-coupling parameter λ is unknown, there is no theoretical prediction for the mass of the

Higgs boson m_H.

2.1.3. Yukawa Coupling

In order to explain the observed masses of the leptons and quarks within the SM, a coupling between the Higgs doublet ϕ, the left-handed fermion doublets f_L and the right-handed fermion singlets f_R is introduced, called Yukawa coupling. After symmetry breaking and using the unitary gauge, the Lagrangian $\mathcal{L}_f$ describing the fermion masses becomes

$$\mathcal{L}_f = -\frac{g_f v}{\sqrt{2}}(\overline{f}_L f_R + \overline{f}_R f_L) - \frac{g_f h}{\sqrt{2}}(\overline{f}_L f_R + \overline{f}_R f_L). \tag{2.16}$$

The first term in this Lagrangian is the mass term of the fermion, describing the coupling of the fermion to the Higgs field, whereby $m_f = \frac{g_f v}{\sqrt{2}}$ determines the mass of the fermion. The second term describes the coupling of the fermion to the Higgs boson. This coupling is proportional to the mass of the fermion. But this mechanism can only explain the masses of the lower components of the fermion isospin doublets. This problem can be solved by defining a conjugate Higgs doublet by

$$\phi_C = \begin{pmatrix} -\phi^{0*} \\ \phi^- \end{pmatrix} \tag{2.17}$$

with hypercharge $Y = -1$. In an analogous way as in Equation (2.16), a gauge invariant Lagrangian, which generates the mass of the fermions in the upper components of the isospin doublets and describes the coupling of these fermions to the Higgs boson, can be constructed. In conclusion, the framework of the Higgs mechanism is able to generate the masses of both the weak vector bosons and the fermions within the SM using the same Higgs doublet ϕ.

2.2. Parity, Charge Conjugation and CP

This section includes a brief description of the CP symmetry and the connection to the baryon asymmetry in the observable universe.

2.2.1. Symmetries and CP

Symmetries are features of a system which are preserved under a transformation. In general, one can differentiate continuous symmetries and discrete symmetries. Due to

Noether's theorem [28], continuous symmetries, such as translational invariance, rotational invariance or time translation invariance, play an import role in classical mechanics as well as in QFTs since they correspond to conserved quantities such as energy or momentum. But discrete symmetries such as the parity symmetry P and the charge conjugation symmetry C are also an essential part of particle physics. A parity transformation P corresponds to a spatial inversion through the origin. A charge conjugation transformation C replaces a particle with its antiparticle and vice versa by conjugating all of the internal quantum numbers. The combination of P and C transformation is called a CP transformation. For example a CP transformation of a left-handed particle leads to a right-handed antiparticle. A conservation of CP in physics would imply that all physical laws would be the same for matter as well as for antimatter.

2.2.2. Baryon Asymmetry and CP Violation

Assuming that matter and antimatter were produced in equal amounts at the Big Bang 13.8 billion years ago [29], it seems unnatural that the present observable universe is only made of baryonic matter. The measured imbalance of matter and antimatter in the observable universe is called baryon asymmetry. The magnitude of the baryon asymmetry can be expressed by the ratio $\frac{n_B}{n_\gamma} \sim 10^{-9}$, where n_B denotes the mean density of baryons in the universe and n_γ denotes the relic density of photons [30–32]. Sakharov found three conditions to explain a matter-dominated universe [13]: Firstly, there must be a process in the early universe which violates the conservation of baryon number. Secondly, there must be C and CP violating interactions. Thirdly, there must be expansion phases of the universe departure from thermal equilibrium.

Parity is conserved in electromagnetic interactions and strong nuclear interactions but not in weak interactions. In 1956, Wu et al. observed the nonconservation of parity P in β decays [33]. The charge conjugation symmetry C is also maximally violated in weak interactions. A charge conjugation transformation of a left-handed particle would lead to a left-handed antiparticle, which does not participate in weak interactions since within the SM only left-handed particles and right-handed anitparticles participate in the weak interaction. In 1964, Christenson, Cronin, Fitch and Turlay [34] observed the violation of CP conservation in the Kaon system, explained within the weak force sector of the SM by a complex phase in the quark mixing CKM matrix in 1973 by Kobayashi and Maskawa [24]. Later, CP violation was also observed in the B Meson system [35].

However, all observed CP violating effects are not sufficient to explain the huge observed matter-antimatter asymmetry in the universe. In 2012, the last missing particle of the SM, the Higgs boson, was found, giving physicists a new opportunity to search for CP

violating effects in the Higgs boson sector.

2.3. Physics of the Higgs Boson

In the following an introduction to the physics of the Higgs boson is presented. An overview of the properties of the Higgs boson predicted by the SM, e.g. couplings and branching ratios, and a description of the discovery of the Higgs boson are given.

2.3.1. Higgs Boson Production

The most likely Higgs boson production channels at the LHC in proton-proton collisions are gluon gluon fusion (ggF) and vector boson fusion (VBF). The cross sections for different Higgs boson production modes as a function of the center of mass energy $\sqrt{s}$ are shown in Figure 2.3 and Feynman diagrams for dominant Higgs boson production channels at the LHC are displayed in Figure 2.4. The largest cross section is provided by ggF. Since gluons are massless and do not directly couple to the Higgs boson, this production mechanism is mainly mediated by the exchange of virtual top quarks. Experimentally, the search for a Higgs boson produced in ggF is challenging due to large QCD-multi-jet background in this channel. The second largest cross section for Higgs boson production at the LHC is provided by VBF. The experimental advantage in VBF Higgs boson production is a rich kinematic structure - there are two hard jets with a large separation in pseudorapidity η, originating from two scattered quarks in proton-proton collisions. The electroweak nature of the coupling of the quarks to vector bosons leads to a low jet activity in the central detector. This significant topology gives physicists an opportunity to identify the Higgs boson production mode and to separate background and signal events. VBF Higgs boson production plays a major role in this analysis and is discussed in detail in Chapter 2.5. Two other important Higgs boson production channels at the LHC are Higgs-strahlung (associated production with weak vector bosons, VH) and associated production with top quarks (ttH).

2.3.2. Higgs Boson Decay

Since the couplings of the Higgs boson to SM particles increases with the particle's mass, the Higgs boson is more likely to decay into heavy particles. The branching ratios BR of the Higgs boson as a function of the Higgs boson mass are illustrated in Figure 2.5. The dominant decay mode is the decay into bottom quarks $H \to b\bar{b}$, followed by the decay into a pair of $W^{\pm}$ bosons $H \to W^{+}W^{-}$, where one of the produced $W^{\pm}$ bosons is not

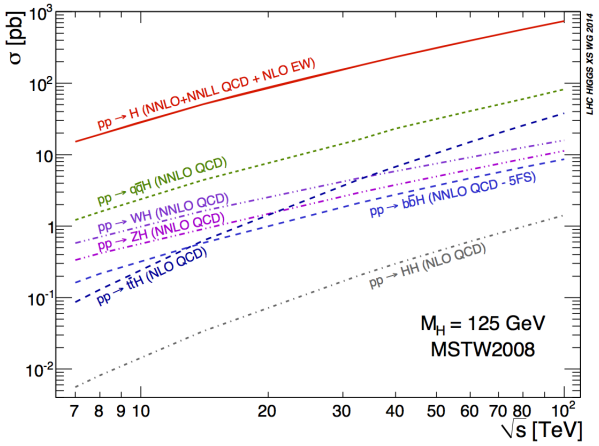

Figure 2.3.: Higgs boson production cross section σ [pb] at the LHC corresponding to a mass of $m_H = 125$ GeV as a function of the center of mass energy $\sqrt{s}$ [TeV].

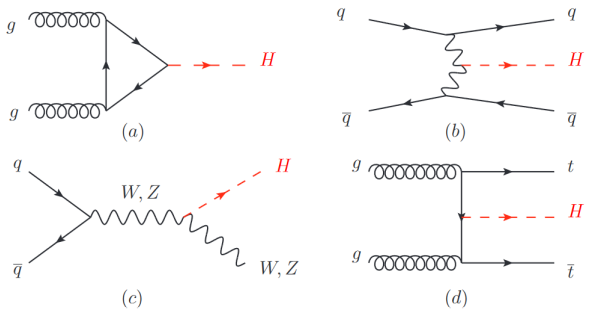

Figure 2.4.: Feynman diagrams at leading order (LO) for Higgs boson production at the LHC: gluon gluon fusion (a), vector boson fusion (b), Higgs-strahlung (c) and associated production with top quarks (d).

on the mass shell, i.e. virtual. The decay mode $H \to Z^0 Z^0$ is also an off-shell decay. Experimentally, the decays $H \to b\bar{b}$ or $H \to c\bar{c}$ are problematic to identify experimentally due to large QCD multi-jet background. Since the Higgs boson does not directly couple to massless particles, decays with the participation of massless particles, such as $H \to \gamma\gamma$, $H \to Z^0\gamma$ and $H \to \gamma\gamma$, are loop induced. The decay mode into two photons has a very small branching ratio but has the big experimental advantage of being very clean. The decay of the Higgs boson into τ leptons, $H \to \tau^+\tau^-$, plays an important role in the physics programme of the LHC since it provides a proof of the Yukawa coupling of fermions to the Higgs boson as well as measurement of the CP quantum numbers of the Higgs boson.

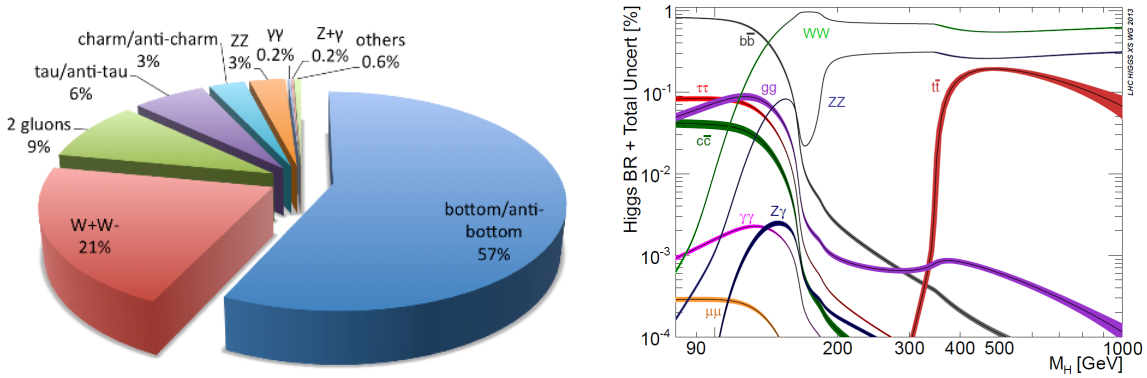

Figure 2.5.: Branching ratios of the decay of a 125 GeV SM Higgs boson (left) and in dependence of the Higgs boson mass, which is a free parameter in the SM (right).

2.3.3. The Discovery of the Higgs Boson

The Higgs boson was discovered by the ATLAS [11] and CMS [12] experiments at the LHC in proton-proton collisions at a center of mass energy $\sqrt{s} = 7$ TeV until 2011 and $\sqrt{s} = 8$ TeV in 2012. The discovery was announced on July 4th, 2012 at CERN. The channels of the discovery were $H \to Z^0 Z^{0*} \to 4l$, $H \to \gamma\gamma$ and $H \to WW^* \to e\nu_e\mu\nu_\mu$. The invariant mass spectrum of the $H \to \gamma\gamma$ channel exhibited a narrow peak over the background, see Figure 2.6. The excess of events near $m_{\gamma\gamma} = 126.5$ GeV about the background prediction is visible. In the $H \to Z^0 Z^{0*}$ decay mode a mass peak over the background distribution of $qq \to Z^0 Z^{0*}$ was found. The channel $H \to Z^0 Z^{0*} \to 4l$ with $l = e, \mu$ provides an event topology with four highly energetic leptons which can be identified and reconstructed leading to a precise determination of the invariant mass of the four lepton system m_{4l}, see Figure 2.6. In addition, background events like di-boson or Z^0+jets events have a relatively low event yield in this channel.

2.3.4. Spin and CP Properties of the Higgs Boson

After the discovery of the Higgs boson it was an important task to investigate the properties of the Higgs boson and measure possible deviations of the Higgs boson characteristics from the SM prediction. In the SM, the Higgs boson is a spin-zero scalar particle with even CP. In general, there are three possible BSM scenarios, described by effective field theories, see Section 2.5.1, characterising the CP properties of the Higgs boson: The observed Higgs boson is a spin-2 particle, the observed Higgs boson is a pure CP-odd particle with spin-0 or the observed Higgs boson is a mixture of the CP-even and the CP-odd state with spin-0. The latter implies CP violation in Higgs physics because in

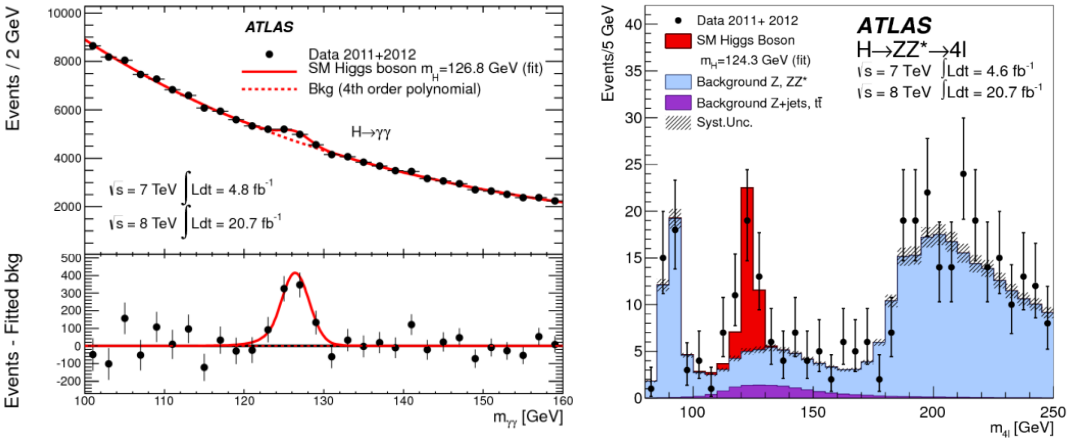

Figure 2.6.: Distribution of the invariant mass $m_{\gamma\gamma}$ of $H \to \gamma\gamma$ candidates (left)[11] and the distribution of the four-lepton invariant mass m_{4l} of $H \to Z^0 Z^{0*} \to 4l$ (right) [36] candidates measured at the LHC by the ATLAS Collaboration.

this case the Higgs boson would be a mass eigenstate but not a CP eigenstate [37]. Spin and parity quantum numbers of the Higgs boson are well tested in experiments in several decay channels [38, 39], in particular in $H \to \tau\tau$, and coincide with the SM prediction. Since the decay of the Higgs boson into two photons is observed, the spin-1 possibility can be excluded due to the Landau-Yang theorem, which states that a massive particle with spin-1 cannot decay into two photons [40]. Further studies using data collected at ATLAS exclude the spin-2 and the negative parity hypothesis at 99.9 % confidence level [38].

2.4. τ Lepton

The τ lepton plays an important role in the presented analysis studying VBF $H \to \tau_{\text{had}}\tau_{\text{had}}$ decays and is introduced in the following.

2.4.1. τ Lepton Properties and Decay

The τ lepton is an elementary fermion with spin $\frac{1}{2}$ and negative electric charge. It is a part of the third generation of the SM particle content, see Figure 2.1, and is unstable with a lifetime of $\tau_\tau = 2.906 \cdot 10^{-13}$ s [41]. Due to its large mass of $m_\tau = 1.77$ GeV [41], the τ lepton can decay into leptons and hadrons, see Figure 2.7. τ leptons decay 35% of the time into leptons, electrons e or muons μ and the corresponding neutrinos ν, and 65% of the time hadronically into mesons, mainly pions π and kaons K, and τ neutrinos ν_τ. The final state in leptonic τ lepton decays involve two neutrinos, while the final state

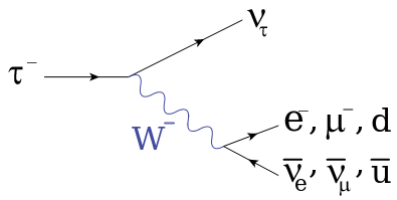

Figure 2.7.: Feynman diagram of main decay modes of a τ lepton mediated by the weak nuclear force.

in hadronic τ lepton decays involve only one neutrino. Hereafter hadronically decaying τ leptons are labelled by τ_{had}, while leptonically decaying τ leptons are labelled by τ_{lep}. Hadronic τ lepton decays are classified by the number of charged mesons in the final state, called prongs. Since the electric charge is conserved in decays, the τ lepton can only decay into an odd number of prongs. The most important hadronic τ-decays are 1-prong with $BR = 0.468$ and 3-prong decays with $BR = 0.143$.

2.4.2. The $H \to \tau\tau$ Decay Mode

At the LHC, the decay $H \to \tau\tau$ offers the best possibility to measure directly the coupling of the Higgs boson to fermions [42]. τ leptons play an important role in Higgs CP quantum number measurements. Therefore, a good τ lepton reconstruction and identification [43] is required. Also, one must separate the decay products of hadronically decaying τ leptons and hadronic jets from QCD processes, which have a very similar kinematic structure, and to find an accurate τ lepton invariant mass reconstruction, which is a big challenge due to produced neutrinos in the decay. The decay $H \to \tau\tau$ is in general separated in three different branches according to several possible classes of τ decays - both leptons decay into hadrons $\tau_{\text{had}}\tau_{\text{had}}$, both leptons decay into leptons $\tau_{lep}\tau_{lep}$ and a mixed τ decay final state $\tau_{\text{lep}}\tau_{\text{had}}$.

2.5. CP Measurement in Vector Boson Fusion Higgs Boson Production

The VBF Higgs boson production mode plays a major role in the VBF CP analysis. An effective Lagrangian framework to describe BSM physics in VBF, in particular regarding anomalous CP couplings at the HVV vertex, is presented. Based on this, the method of the Optimal Observable is introduced and the results of the Run 1 VBF CP analysis are presented.

2.5.1. Effective Lagrangian Framework

When constructing a Lagrangian describing BSM physics, this Lagrangian has to include the well established SM at least in the low energy limit. Assuming that dynamics at low energies are independent of dynamics at high energies, an effective field theory can be used to describe low energy physics [44]. Therefore, it is possible to describe deviations of the Higgs boson couplings from the SM expectation by a model-independent effective Lagrangian framework [45, 46]. The most general form of such a Lagrangian is

$$\mathcal{L}_{eff} = \mathcal{L}_{\mathrm{SM}} + \mathcal{L}_{D=5} + \mathcal{L}_{D=6} + ... \tag{2.18}$$

$\mathcal{L}_{SM}$ is the renormalizable SM Lagrangian containing operators of at most mass dimension four. $\mathcal{L}_{D=5}$ is the part of the effective Lagrangian containing operators of dimension five. However, since $\mathcal{L}_{D=5}$ leads to the violation of lepton number L, this term will be removed [47, 48]. The dimension-six term of the Lagrangian, $\mathcal{L}_{D=6}$, is the interesting part for the study of the CP quantum numbers of the Higgs boson. Possible terms of the Lagrangian $\mathcal{L}_{eff}$ with dimensions larger than six will not be relevant for this study at the present LHC research phase. Therefore, in an expansion of the inverse power of the scale of new physics Λ, the effective Lagrangian can be written as

$$\mathcal{L}_{eff} = \mathcal{L}_{\mathrm{SM}} + \frac{1}{\Lambda^2}\sum_k f_k \mathcal{O}_k \tag{2.19}$$

with the SM Lagrangian $\mathcal{L}_{SM}$, dimensionless Wilson coefficients f_k, which represent the coupling strengths, and dimension-six operators $\mathcal{O}_k$. $\mathcal{L}_{\mathrm{SM}}$ includes the couplings described within the SM. In the following, all interaction of the Higgs boson with other particles of the SM, except weak gauge bosons and photons, are assumed as predicted by the SM. That means that couplings of the Higgs boson to fermions like the τ lepton are given by the SM prediction. An effective Lagrangian [14, 49], which is $SU(2)_L \times U(1)_Y$ invariant, extended by CP-violating operators, can be written in a linear representation as

$$\mathcal{L}_{\mathrm{eff}} = \mathcal{L}_{\mathrm{SM}} + \frac{f_{\tilde{B}B}}{\Lambda^2}\mathcal{O}_{\tilde{B}B} + \frac{f_{\tilde{W}W}}{\Lambda^2}\mathcal{O}_{\tilde{W}W} + \frac{f_{\tilde{B}}}{\Lambda^2}\mathcal{O}_{\tilde{B}} \tag{2.20}$$

with three dimension-six operators

$$\mathcal{O}_{\tilde{B}B} = \phi^\dagger \hat{\tilde{B}}_{\mu\nu}\tilde{B}^{\mu\nu}\phi \tag{2.21}$$

$$\mathcal{O}_{\tilde{W}W} = \phi^\dagger \hat{\tilde{W}}_{\mu\nu}\tilde{W}^{\mu\nu}\phi \tag{2.22}$$

$$\mathcal{O}_{\tilde{B}} = (D_\mu \phi)^\dagger \hat{\tilde{B}}^{\mu\nu} D_\nu \phi \tag{2.23}$$

and the corresponding dimensionless Wilson coefficients $f_{\tilde{B}B}$, $f_{\tilde{W}W}$ and $f_{\tilde{B}}$. B^μ and $W^{j\mu}$ ($j \in \{1,2,3\}$) are the electroweak gauge fields and ϕ is the Higgs doublet. Furthermore, $\hat{V}_{\mu\nu}$ represents the field strength tensors and $\tilde{V} = \frac{1}{2}\epsilon_{\mu\nu\rho\sigma}V^{\rho\sigma}$ denotes the dual field strength tensors, where $V = W^j, B$ and

$$\hat{B}_{\mu\nu} + \hat{W}_{\mu\nu} = \frac{ig'}{2} B_{\mu\nu} + \frac{ig_W}{2}\sigma^j W^j_{\mu\nu}. \tag{2.24}$$

The operator $\mathcal{O}_{\tilde{B}}$ is neglected in the following since $\mathcal{O}_{\tilde{B}}$ corresponds to CP-violating charged triple gauge couplings, which are strongly experimentally constrained [50]. Electroweak symmetry breaking leads to an effective Lagrangian [51, 52] of the form

$$\mathcal{L}_{\text{eff}} = \mathcal{L}_{\text{SM}} + \tilde{g}_{HAA}\tilde{A}_{\mu\nu}A^{\mu\nu} + \tilde{g}_{HAZ}\tilde{A}_{\mu\nu}Z^{\mu\nu} + \tilde{g}_{HZZ}\tilde{Z}_{\mu\nu}Z^{\mu\nu} + \tilde{g}_{HWW}\tilde{W}^+_{\mu\nu}W^{\mu\nu}_- \tag{2.25}$$

where $A_\mu, Z_\mu, W^\pm_\mu$ and H describe the photon γ, Z^0, $W^\pm$ and the Higgs field, respectively, and g_i ($i = HAA, HAZ, HZZ, HWW$) are couplings, which are constrained by the required invariance of the Lagrangian under $SU(2)_L \times U(1)_Y$ gauge transformations, ensuring that only two couplings are independent. The couplings fulfil the relations

$$\tilde{g}_{HAA} = \frac{g}{2m_W}(\tilde{d}\sin^2\theta_W + \tilde{d}_B\cos^2\theta_W) \tag{2.26}$$

$$\tilde{g}_{HAZ} = \frac{g}{2m_W}\sin 2\theta_W(\tilde{d} - \tilde{d}_B) \tag{2.27}$$

$$\tilde{g}_{HZZ} = \frac{g}{2m_W}(\tilde{d}\cos^2\theta_W + \tilde{d}_B\sin^2\theta_W) \tag{2.28}$$

$$\tilde{g}_{HWW} = \frac{g}{m_W}\tilde{d} \tag{2.29}$$

where dimensionless coupling parameters $\tilde{d}$ and $\tilde{d}_B$ are given by

$$\tilde{d} = -\frac{m_W^2}{\Lambda^2} f_{\tilde{W}W} \tag{2.30}$$

$$\tilde{d}_B = -\frac{m_W^2}{\Lambda^2}\tan^2\theta_W f_{\tilde{B}B}, \tag{2.31}$$

respectively. In the following one assumes $\tilde{d} = \tilde{d}_B$ since the different couplings of the Higgs boson to vector bosons cannot be distinguished experimentally in this analysis. This assumption leads to the following relation of the couplings

$$\tilde{g}_{HAA} = \tilde{g}_{HZZ} = \frac{1}{2}\tilde{g}_{HWW} = \frac{g}{2m_W}\tilde{d} \qquad \tilde{g}_{HAZ} = 0. \tag{2.32}$$

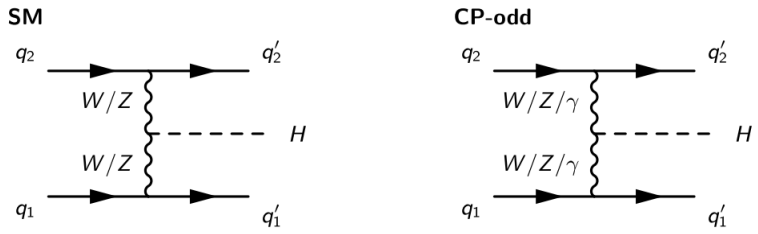

Figure 2.8.: Feynman diagram describing the SM prediction (left) and the BSM prediction described by the effective Lagrangian in Equation (2.25) (right).

Possible couplings of the Higgs boson to vector bosons described by Equation (2.25) are shown in Figure 2.8.

2.5.2. Tensor Structure

The most general tensor structure [49] of the HVV vertex describing the Lorentz invariant interaction of the involved fields is given by

$$T^{\mu\nu}(q_1, q_2) = c_1(q_1, q_2)g^{\mu\nu} + c_2(q_1, q_2)(q_1 q_2 g^{\mu\nu} - q_2^\mu q_1^\mu) + c_3(q_1, q_2)\epsilon^{\mu\nu\rho\sigma} q_{1\rho} q_{2\sigma} \tag{2.33}$$

with the four momenta q_1, q_2 of the gauge bosons $V = W^\pm, Z^0, \gamma$. Here, $g^{\mu\nu}$ denotes the Minkowski metric, $\epsilon^{\mu\nu\rho\sigma}$ is the antisymmetric tensor and c_j ($j \in \{1, 2, 3\}$) are scalar form factors. The form factors c_2 and c_3 describe new physics, thus $c_2 = c_3 = 0$ represents the SM case with $c_1 = 2\frac{m_V^2}{v}$. Couplings which deviate from the SM prediction, which could be experimentally observed in deviations of the Higgs boson production cross section and decay rates, are called anomalous couplings. The terms in Equation (2.33) which include c_1 and c_2 are CP-even, while the term including c_3 is CP-odd. Thus, the SM case corresponds to a CP-even coupling at the HVV vertex. Since this analysis focuses on a search for an additional anomalous CP-odd coupling of the weak gauge bosons to the Higgs boson, one considers $c_1 = \frac{2m_V^2}{v}$, $c_2 = 0$ and $c_3 \neq 0$. Based on the choice $\tilde{d} = \tilde{d}_B$ given in Section 2.5.1, the tensor structure can be written using only the parameter $\tilde{d}$ by

$$T^{\mu\nu} = \sum_{V=W,Z^0} \frac{2m_V^2}{v} g^{\mu\nu} + \sum_{V=W,Z^0,\gamma} \frac{2g}{m_W} \tilde{d} \epsilon^{\mu\nu\rho\sigma} q_{1\rho} q_{2\sigma}, \tag{2.34}$$

where the coefficients c_i in Equation (2.33) are given by

$$c_1 = \frac{2m_V^2}{v} \qquad c_2 = 0 \qquad c_3 = \frac{2g}{m_W}\tilde{d}. \tag{2.35}$$

2.5.3. Matrix Element

The matrix element $\mathcal{M}$ for VBF Higgs boson production is given by

$$\mathcal{M} = \mathcal{M}_{\mathrm{SM}} + \tilde{d} \cdot \mathcal{M}_{CP-\mathrm{odd}}, \tag{2.36}$$

where the CP-odd contribution, parametrised by $\tilde{d}$, is a result of the dimension-six operators occurring in the effective Lagrangian in Equation (2.20). The squared matrix element $|\mathcal{M}|^2$ consists of three terms

$$|\mathcal{M}|^2 = |\mathcal{M}_{\mathrm{SM}}|^2 + \tilde{d} \cdot 2\mathrm{Re}(\mathcal{M}^*_{\mathrm{SM}}\mathcal{M}_{CP-\mathrm{odd}}) + \tilde{d}^2 \cdot |\mathcal{M}_{CP-\mathrm{odd}}|^2. \tag{2.37}$$

Since the squared matrix element $|\mathcal{M}|^2$ is proportional to the differential cross section $d\sigma$, Equation 2.37 can be written as

$$d\sigma = d\sigma_{\mathrm{SM}} + \tilde{d} \cdot d\sigma_{CP-\mathrm{odd}} + \tilde{d}^2 \cdot d\sigma_{CP-\mathrm{even}}. \tag{2.38}$$

The interference term $\tilde{d} \cdot 2\mathrm{Re}(\mathcal{M}^*_{\mathrm{SM}}\mathcal{M}_{CP-\mathrm{odd}})$ in Equation (2.37) is CP-odd and contributes linearly in $\tilde{d}$ to the differential cross section $d\sigma$, whereas $|\mathcal{M}_{\mathrm{SM}}|^2$ and $|\mathcal{M}_{CP-\mathrm{odd}}|^2$ are CP-even. However, the third term $|\mathcal{M}_{CP-\mathrm{odd}}|^2$ in Equation 2.37 increases the total cross section quadratically in $\tilde{d}$, while the total cross section does not depend on the interference term $\tilde{d} \cdot 2\mathrm{Re}(\mathcal{M}^*_{\mathrm{SM}}\mathcal{M}_{CP-\mathrm{odd}})$, since this term vanishes by integrating over a CP-even phase space.

2.5.4. The Optimal Observable

One strategy to investigate CP invariance in VBF Higgs boson production is the method of the Optimal Observable. For small values of the parameter $\tilde{d}$, the Optimal Observable combines information of the entire phase space in one single observable, which has the highest sensitivity for an estimation of the parameter of interest [53]. The method of the Optimal Observable has been used and applied before in several other experimental analyses [37, 50, 54–60], in particular in the Run 1 VBF CP analysis of the Higgs boson [14]. In the investigation of processes occurring in high-energy physics, an important observable is the differential cross section. An expansion of the differential cross section $\frac{d\sigma}{d\Omega}(\tilde{d})$ can be written for small values of $\tilde{d}$ as [53]

$$\frac{d\sigma}{d\Omega}(\tilde{d}) = S^{(0)}(\Omega) + \tilde{d} \cdot S^{(1)}(\Omega) + \tilde{d}^2 \cdot S^{(2)}(\Omega), \tag{2.39}$$

where Ω is the phase space and, in accordance with Equation 2.36, $S^{(0)}, S^{(1)}$ and $S^{(2)}$ are given by

$$S^{(0)} = |\mathcal{M}_{\mathrm{SM}}|^2 \qquad S^{(1)} = 2\mathrm{Re}(\mathcal{M}^*_{\mathrm{SM}}\mathcal{M}_{CP-\mathrm{odd}}) \qquad S^{(2)} = |\mathcal{M}_{CP-\mathrm{odd}}|^2. \tag{2.40}$$

The corresponding likelihood function $\mathcal{L}$ is given by

$$\mathcal{L}(\tilde{d}) = \prod_k^N (S^{(0)}(\Omega_k) + \tilde{d} \cdot S^{(1)}(\Omega_k) + \tilde{d}^2 \cdot S^{(2)}(\Omega_k)) \tag{2.41}$$

where the product runs over the phase space variables Ω_k [58]. Using the method of the maximum likelihood estimation to obtain the best estimate $\hat{\tilde{d}}$ of the true value $\tilde{d}$, one maximises the likelihood function of Equation (2.41). It is customary and usually simpler to maximise the logarithm of the likelihood function $\log(\mathcal{L})$. The condition to determine the maximum can be written as

$$\frac{\partial \log(\mathcal{L})}{\partial \tilde{d}}|_{\tilde{d}=\hat{\tilde{d}}} = 0. \tag{2.42}$$

This leads to

$$\sum_k^N \frac{S^{(1)} + 2\hat{\tilde{d}} \cdot S^{(2)}}{S^{(0)} + \hat{\tilde{d}} \cdot S^{(1)} + \hat{\tilde{d}}^2 \cdot S^{(2)}} = 0. \tag{2.43}$$

This can be rewritten as

$$\sum_k^N \frac{\mathcal{O}_1 + 2\hat{\tilde{d}} \cdot \mathcal{O}_2}{1 + \hat{\tilde{d}} \cdot \mathcal{O}_1 + \hat{\tilde{d}}^2 \cdot \mathcal{O}_2} = 0, \tag{2.44}$$

where

$$\mathcal{O}_1 = \frac{S^{(1)}}{S^{(0)}} = \frac{2\mathrm{Re}(\mathcal{M}^*_{\mathrm{SM}}\mathcal{M}_{CP-\mathrm{odd}})}{|\mathcal{M}_{\mathrm{SM}}|^2} \tag{2.45}$$

and

$$\mathcal{O}_2 = \frac{S^{(2)}}{S^{(0)}} = \frac{|\mathcal{M}_{CP-\mathrm{odd}}|^2}{|\mathcal{M}_{\mathrm{SM}}|^2}. \tag{2.46}$$

Since only $\mathcal{O}_{1,2}$ enter the likelihood function, these two variables include the information of the phase space and can be used to estimate the parameter $\tilde{d}$ instead. Thus, a fitting procedure of the maximum likelihood function in a multi-dimensional phase space can be reduced to a fit of $\mathcal{O}_{1,2}$ in two dimensions with the same sensitivity. Therefore $\mathcal{O}_{1,2}$ are called Optimal Observables of first and second order, respectively. If CP is conserved, corresponding to the SM prediction, one expects $\langle\mathcal{O}_1\rangle = 0$, since $\mathcal{O}_1$ is a CP-odd variable. Violation of CP conservation, corresponding to $\tilde{d} \neq 0$, leads to a shift of the mean value $\langle\mathcal{O}_1\rangle$ from zero, thus $\langle\mathcal{O}_1\rangle \neq 0$ implies CP violation in the Higgs sector. The Optimal

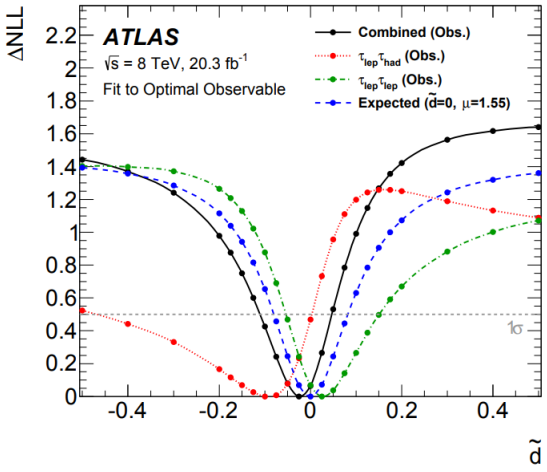

Figure 2.9.: Likelihood fit to $\mathcal{O}_1$ of the VBF CP analysis of the ATLAS experiment in Run 1 [14].

Observable of second order $\mathcal{O}_2$ is a CP-even observable but sensitive to $\tilde{d}^2$.

2.6. Results of the VBF CP Study in Run 1

The Run 1 VBF CP analysis using the Optimal Observable was published in 2016 in the $H \to \tau_{\text{lep}}\tau_{\text{lep}}$ [56] and $H \to \tau_{\text{lep}}\tau_{\text{had}}$ [61] channels using ATLAS data collected at the LHC at $\sqrt{s} = 8$ TeV in 2012 corresponding to an integrated luminosity of 20 fb^{-1} [14]. It excluded the regions $\tilde{d} > 0.05$ and $\tilde{d} < -0.11$ for the CP-mixing parameter $\tilde{d}$ at 68% confidence level (CL) using a maximum likelihood fit to the $\mathcal{O}_1$ distribution, see Figure 2.9, but no 95% confidence level was set. Although it was not published in 2016, the $H \to \tau_{\text{had}}\tau_{\text{had}}$ channel was also investigated [62]. The value of $\tilde{d}$ is constrained on 68% CL by this channel to an interval of [-0.539,-0.0519] using a maximum likelihood fit to $\mathcal{O}_1$. The combination of the three presented channels $H \to \tau_{\text{lep}}\tau_{\text{lep}}$, $H \to \tau_{\text{lep}}\tau_{\text{had}}$ and $H \to \tau_{\text{had}}\tau_{\text{had}}$, to an inclusive VBF $H \to \tau\tau$ channel leads to $\tilde{d} \in [-0.468, 0.053]$ at 95% CL and $\tilde{d} \in [-0.160, -0.014]$ at 68% CL [62].

2.7. Hadron Collider Physics and Phenomenology

In this section an introduction of physics and terminology of particle collider and accelerator is presented.

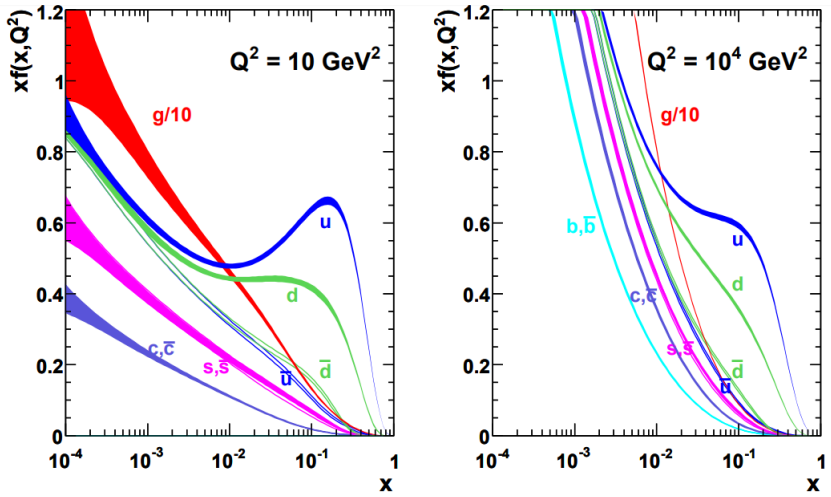

Figure 2.10.: Sketch of NLO PDFs at scales of $Q^2 = 10$ GeV^2 (left) and $Q^2 = 10^4$ GeV^2 (right). The uncertainty bands correspond to a 68% confidence level [65].

2.7.1. Partons and Parton Distribution Functions

The parton model states that all hadrons are composite of point-like particles, quarks and gluons [63, 64]. As the LHC is a proton-proton collider, the interacting particles at the hard scattering process of the proton beams are valence quarks, sea-quarks and gluons, the constituents of the proton, called partons. Each single parton of the proton carries a fraction of the proton's momentum, termed as the Bjorken x. The distribution of parton momenta within the proton is described by Parton Distribution Functions (PDF) [65], which have to be obtained from deep-inelastic scattering experiments and cannot be obtained from perturbative QCD calculations. The PDFs $f(x, Q^2)$ describe the probability density to find a parton with momentum fraction x probed at a squared momentum transfer Q^2 and are sketched in Figure 2.10. Since the flavours and the momenta of the incoming and outgoing partons involved in the hard scattering process cannot be determined experimentally, all possible combinations have to be summed weighted by the corresponding PDF when calculating the corresponding matrix element $\mathcal{M}$ of the process.

2.7.2. Luminosity and Cross Section

An important quantity in collider physics is the instantaneous luminosity $\mathcal{L}$, which connects the rate of proton bunch collisions $\frac{dN}{dt}$ occurring in the collider and the total cross section σ by

$$\frac{dN}{dt} = \sigma \mathcal{L}. \tag{2.47}$$

The luminosity $\mathcal{L}$ can be expressed by

$$\mathcal{L} = \frac{n_1 n_2 f}{A}, \tag{2.48}$$

where $n_{1,2}$ are the number of protons in the colliding bunches, f denotes the frequency of collisions and A is the size of the beams in the transverse plane. Using the integrated luminosity $\mathcal{L}_{\text{int}} = \int \mathcal{L} dt$, the number of events is given by $N = \sigma \mathcal{L}_{\text{int}}$. Theoretically, the cross section σ for a process $ij \to X$ is determined by the matrix element $\mathcal{M}$, describing the probability of a process given the initial and final state, by the factorisation theorem [66]

$$\sigma = \int dx_i dx_j f(x_i, Q^2) f(x_j, Q^2) \sigma_{ij} \tag{2.49}$$

with the partonic cross section $\sigma_{ij} = \int d\Omega F^{-1} |\mathcal{M}(ij \to X)|^2$ where F denotes the particle flux.

2.7.3. Underlying Event and Pile-Up

At each bunch collision, there occur many collision between protons within the bunches but in general not more than one interaction of the partons within a proton-proton collision, the hard scattering, is interesting for the analysis. Other interactions of the proton remnants of this proton-proton collision are referred to as underlying events. Additional proton-proton collisions within the same bunch collision, i.e. overlapping secondary proton-proton collisions, are called in-time pile-up events. Due to the short bunch separation in the collider compared to the read-off time of the detector, it is possible that recorded proton-proton collisions in truth belong to the previous or the following bunch collision than recorded. These events are called out-of-time pile up events [67].

2.7.4. Hadronisaton

As mentioned in Section 2.1.1, the energy-dependence of the strong-coupling constant α_S leads to the phenomenon of colour confinement in QCD. Since α_S increases with decreasing energy, particles carrying colour charge tend to emit quarks and gluons as their energy decreases and form stable colourless hadrons. Therefore, single colour-charged gluons and quarks cannot be directly observed in nature. The mechanism describing the production of hadrons, which are observed in the detector, from quarks and gluons produced in the hard process is called hadronisation.

3. Experimental Setup

An overview of the LHC and the ATLAS detector is presented in this chapter.

3.1. LHC

The Large Hadron Collider (LHC) [68] is a particle accelerator at CERN in Geneva, Switzerland, desgined to be the largest and highest-energy particle accelerator in the world. It lies, protected from cosmic radiation, deep beneath the earth's surface in a tunnel with a circumference of 27 km and it primarily generates proton-proton collisions at four different crossing points of the proton beams. The LHC is the last ring in a chain of several accelerators at CERN boosting the protons step-by-step to the final energy. The first research run from 2010 to 2013 (Run 1) was performed at a center of mass (CM) energy $\sqrt{s}$ of 7 TeV until 2011 and 8 TeV from 2012, culminating in the discovery of the Higgs boson. After an upgrade from 2013 to 2015, Run 2 is started with $\sqrt{s}$=13 TeV from 2015. The four main experiments at the LHC, which are located at the four crossing points of the collider, are ALICE [69], ATLAS [70], CMS [71] and LHCb [72]. The main focus of the ATLAS and CMS physics program is on Higgs boson and top quark physics, establishing the SM of particle physics and searching for BSM physics, e.g. supersymmetric and Dark Matter particles as well as the search for extra dimensions. The ALICE experiment focuses on studying quark-gluon plasma, while the LHCb experiment investigates mainly CP violation in bottom quark physics.

3.2. The ATLAS detector

The ATLAS experiment collects data from events occurring at the LHC with help of the multi-purpose ATLAS detector, see Figure 3.1. The basic components of the ATLAS detector are the Inner Detector (ID), the calorimeter system (CS), the Muon system and the trigger system.

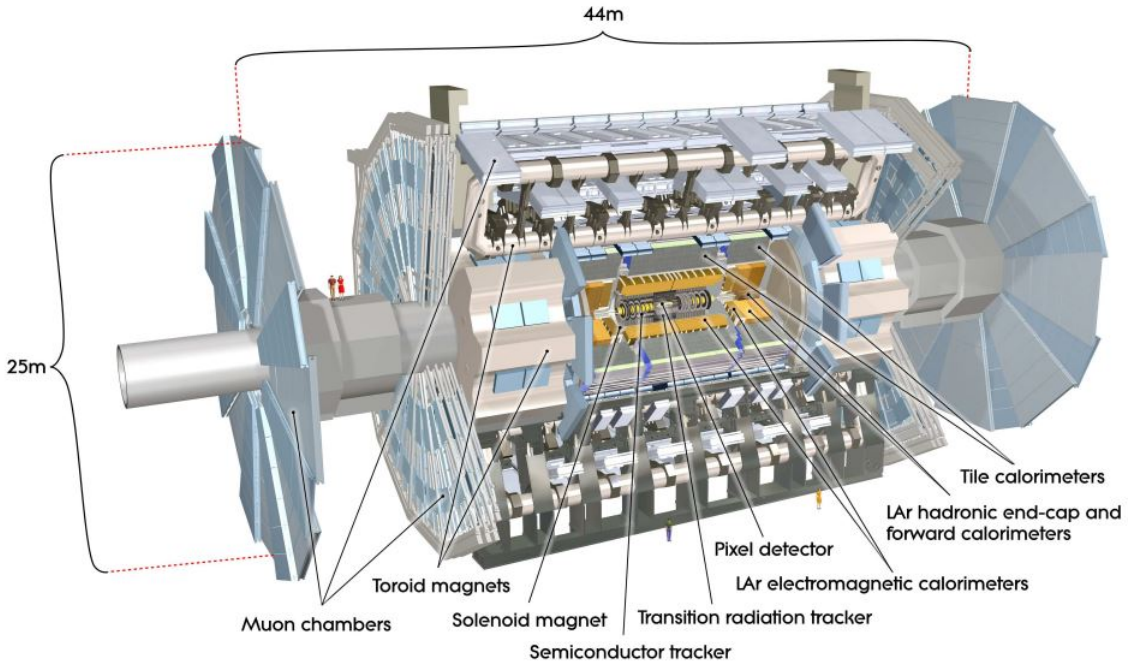

Figure 3.1.: Profile of the ATLAS (A Toroidal LHC Appartus) detector [70]. The ATLAS detector is 46 metres long and 25 metres in diameter. The barrel chambers are arranged cylindrically in three layers around the beam axis and the end-caps are orthogonal to the beam axis.

3.2.1. Coordinate System

A right-handed coordinate system is used to describe events in the ATLAS detector. The interaction point of the colliding particles in the ATLAS detector is the origin of the coordinate system. The z-axis corresponds to the direction of the beam, the y-axis points upwards and the x-axis points to the middle point of the LHC ring. Based on this, polar coordinates can be defined. The azimuthal angle ϕ and the polar angle θ are defined with respect to the z-axis.

Two common used quantities in hadron collider physics are rapidity and pseudorapidity. The rapidity y is defined by

$$y = \frac{1}{2} \ln \left(\frac{E + p_z}{E - p_z} \right) \tag{3.1}$$

where E is the energy and p_z the momentum of the particle in z-direction. If the mass of a jet or a particle can be neglected, one finds $p_z \approx E \cos\theta$ and therefore $y \approx \frac{1}{2} \ln(\frac{1+\cos\theta}{1-\cos\theta}) = \frac{1}{2} \ln(\cot^2(\frac{\theta}{2}))$. Based on this, the pseudorapidity η is defined as

$$\eta = -\ln(\tan(\frac{\theta}{2})) \tag{3.2}$$

where θ is the angle between the particle momentum p and the beam axis. Differences in pseudorapidity are invariant under boosts in z-direction.

To quantify the angular distance between two objects, the quantity

$$\Delta R = \sqrt{(\eta_1 - \eta_2)^2 + (\phi_1 - \phi_2)^2} = \sqrt{(\Delta\phi)^2 + (\Delta\eta)^2}, \tag{3.3}$$

where $\eta_{1,2}$ and $\phi_{1,2}$ are pseudorapidity and azimuthal angle of particle 1 and 2, is used.

3.2.2. Inner Detector

The main task of the ID is to measure the momenta and tracks of charged particles. It lies close to the interaction point of the colliding particles and consists of three subsystems: the Pixel Detector (PXD), the Semi-Conductor Tracker (SCT) and the Transition Radiation Tracker (TRT).

The PXD is built out of an insertable B-Layer (IBL) [73] and three layers of silicon modules [74], which provide a high-precision measurement of the particles' trajectories. The IBL was newly installed for Run 2 and compensates for increasing radiation damage at high luminosity and increases the b-tagging and tracking of the ID. The PXD is surrounded by the SCT [75], consisting of several layers of one-sided p-on-n silicon microstrips. The SCT is a fundamental part of the ATLAS tracking system of the ID. The TRT, the outermost of the tracking subsystems of the ID, uses roughly 400.000 drift tubes, so-called straws, as detector elements. The straws are filled with gas which is ionized by charged particles traversing the TRT. The TRT is an efficient electron identifier and helps to distinguish pions and electrons by detecting transition radiation photons in the gas-mixture, mostly xenon, of the straws. The PXD and the SCT cover a range of $|\eta| < 2.5$, respectively, whereas the TRT covers the range $|\eta| = 2.0$.

Since the main task of the ID is to detect the tracks of charged particles, it is surrounded by a solenoid, which generates a high-precision magnetic field with a field strength of 2 T. This magnetic field forces electrically charged particles on circular paths, from which momenta and charge of these particles can be determined based on information provided by the PXD, SCT and TRT. Efficient algorithms reconstruct the trajectories and momenta of particles with $p_T > 0.5$ GeV. The information of the origin of the tracks, the primary and secondary vertices, and the electric charge can be determined by the ID. The relative resolution of the particle momentum in the ID is given by $\frac{\sigma}{p_T} = (4.83 \pm 0.16) \cdot 10^{-4} \frac{p_T}{\text{GeV}}$ [76].

3.2.3. Calorimeter System

The CS is located in the next layer outside the ID. It consists of different sampling calorimeters and covers the range of $|\eta| < 4.9$. The task of the CS is to measure the energy of particles. In doing so, the basic idea is that particles which enter the calorimeter initialise particle showers which deposit energy in the calorimeters by interacting with the dense absorber material. Alternating dense absorber material with active detector material, where the output signal is created, the deposited energy of the particles in the calorimeter can be measured.

The CS consists of an electromagnetic calorimeter (ECal) and a hadronic calorimeter (HCal) [77]. The ECal is build up of lead as absorber and liquid argon as the active material and is designed to primarily measure the energy of particles which interact via the electromagnetic interaction, i.e. charged particles and photons. The ECal covers a region of $|\eta| < 1.475$ within the barrel and $1.375 < |\eta| < 3.2$ within the end-caps. The designed energy resolution of the ECal is

$$\frac{\sigma_E}{E} = \frac{10\%}{\sqrt{E}} \oplus 0.7\%, \tag{3.4}$$

where the energy E is given in GeV. The HCal is designed to measure the energy of particles which interact via the strong force such as hadrons. The HCal uses steel as the absorber and scintillating tiles as the active material. The designed energy resolution [70] of the HCal in the region $|\eta| < 3.2$ is

$$\frac{\sigma_E}{E} = \frac{50\%}{\sqrt{E}} \oplus 0.7\% \tag{3.5}$$

and in the region $3.1 < |\eta| < 4.9$ the designed energy resolution is

$$\frac{\sigma_E}{E} = \frac{100\%}{\sqrt{E}} \oplus 10\%. \tag{3.6}$$

3.2.4. Muon Spectrometer

Muons with energies up to 100 GeV are minimum ionizing particles, therefore they traverse the calorimeter system without being absorbed. To detect muons, a Muon Spectrometer (MS) is located in the outermost layer of the ATLAS detector. The MS contains three super-conducting air-core toroids, tracking chambers for a precise measurement of the muon momenta and a trigger system. This provides an excellent resolution for the measurements of large momenta and high-precision tracking of muons. The MS is divided

into three subregions, the barrel region covering the range $|\eta| < 1.4$, the end-cap region covering $1.6 < |\eta| < 2.7$ and the transition region covering $1.5 < |\eta| < 1.6$. The MS measures muon tracks in a magnetic field with field strength up to 3.5 T produced by large superconducting toroid magnets, leading also to information about transverse momenta of the muons. The trajectories of muons are mainly measured by Monitored Drift Tubes (MDT) and cathode strip chambers (CSC). The resolution of the muon spectrometer is

$$\frac{\sigma_{p_T}}{p_T} = 10\% \tag{3.7}$$

at a transverse momentum of $p_T = 1$ TeV [70].

3.2.5. Missing Transverse Momentum

The momentum of a particle in the plane transverse to the beam axis, i.e. in the x-y-plane, is called the transverse momentum p_T and is defined by

$$p_T = \sqrt{p_x^2 + p_y^2}, \tag{3.8}$$

where $p_{x,y}$ denotes the momentum of the particle into the x and y direction, respectively. The transverse energy E_T is defined analogously. Using the concept of energy and momentum conservation, missing transverse energy (MET) $\not{E}_T$ in the final state can be used for the identification of undetectable particles such as neutrinos ν since the transverse energy in the initial state is zero. $\not{E}_T$ corresponds to the total transverse momentum of all produced neutrinos since neutrinos have a negligible mass. If more than one neutrino is produced, it is not straight-forward to reconstruct the transverse momenta of the individual neutrinos and demanding methods have to be used, see Section 3.4.2.

3.2.6. Trigger System and Data Acquisition

Due to the high collision rate at the LHC, a highly selective and efficient trigger system [78, 79] is used to select interesting events in the ATLAS experiment. For Run 2, the whole trigger system was upgraded to manage the increased CM energy $\sqrt{s}$ and luminosity L. The improved ATLAS trigger system consists in Run 2 of two independent stages, the level-1 trigger and the high level trigger (HLT). The hardware-based level-1 trigger uses muon trigger chamber and calorimeter signals for a preliminary event selection and identification of Regions of Interest (RoI) for further processing, reducing the event rate from 40 MHz to approximately 100 kHz. The software-based HLT uses fast offline algorithms working

in the RoI, reducing the recorded bunch-crossing rate from 100 kHz to approximately 1 kHz.

3.3. Monte Carlo Simulations at ATLAS

Simulating physical processes at hadron colliders such as the LHC by using Monte Carlo (MC) simulations is an essential part of research in particle physics. Both signal and background simulations play a key role in the comparison and connection of theory and experiment and will help in the interpretation of measurements and rejection of background events. The event generation can be divided into four steps: simulating the hard interaction, parton showers, hadronisation and underlying events. The detector response simulation ensures that simulated objects and measured observables can be reconstructed using the same methods and algorithms as used for real data objects. MC simulations that take into account experimental effects are referred to as being at reconstruction level (reco-level). MC simulations excluding experimental effects are referred to be at truth-level and also provide parton-level information and the flavour of the interacting partons. In the final analysis, the size of the generated MC sample must be weighted corresponding to the integrated luminosity of the recorded data at the ATLAS detector.

The software framework of the ATLAS experiment is called ATHENA [80], which includes many parton level- and general-purpose generators such as PYTHIA [81–85] and SHERPA [86–89], briefly described in Section 4.2, which can be extended and combined using other generators or add-on packages that carry out the fragmentation and hadronisation. The ATLAS detector response is simulated by GEANT4 [90].

3.4. Object Definition and Reconstruction

To perform an accurate analysis in the $H \to \tau_{\text{had}}\tau_{\text{had}}$ decay mode, it is necessary to have efficient identification and reconstruction methods for several objects. The object definition and reconstruction is presented in this chapter. Before the reconstruction in the $H \to \tau_{\text{had}}\tau_{\text{had}}$ channel is described, key algorithms for object reconstruction at the ATLAS experiment such as the anti-k_t jet algorithm and the Missing Mass Calculator are briefly described.

3.4.1. Jet Algorithm

A collimated bunch of hadrons, which fly roughly in the same direction in the detector and arise from the fragmentation of partons, is called a jet. The classification of particles into jets is performed by jet clustering algorithms. Jet algorithms perform a mapping between the hadrons, detectable by energy depositions in the calorimeters, and the partons of the hard scattering process. The anti-k_t algorithm [91] is a sequential jet clustering algorithm, which is based on two distance measures: the distance d_{ij} between two objects (particles or pseudo-jets) i and j and the distance d_{iB} between an object i and the beam B, which are given by

$$d_{ij} = \min(k_{ti}^{-2}, k_{tj}^{-2}) \frac{\Delta_{ij}^2}{R^2} \tag{3.9}$$

$$d_{iB} = k_{ti}^{-2}, \tag{3.10}$$

where $\Delta_{ij}^2 = (y_i - y_j)^2 + (\phi_i - \phi_j)^2$ and k_{ti}, y_i and ϕ_i are the transverse momentum, rapidity and the azimuthal angle of the object i, respectively, and R is the distance parameter (jet radius). The anti-k_t algorithm with a distance parameter $R = 0.4$ is used in this analysis. The inclusive anti-k_t algorithm starts with a list of objects and searches for the minimum of d_{ij} for all possible combinations of objects i and j in the event. If the objects i and j give the minimum of d_{ij}, these objects are merged by summing the momentum vectors. Subsequently, the objects i and j are removed from the list and only the new merged object is kept. Otherwise, if d_{iB} is the minimum, the object i is defined as a final jet and is removed from the list of objects. This procedure is done for all objects of the list. If no object is left, the algorithm ends.

3.4.2. Missing Mass Calculator

It is not trivial to construct the momentum four-vectors of the τ leptons in $H \to \tau_{\text{had}}\tau_{\text{had}}$ decays and to calculate the invariant mass of the $\tau\tau$-system $m_{\tau\tau}$ due to produced neutrinos ν in τ_{had} decays. Since neutrinos ν are not detectable using the ATLAS detector, they can only be identified by a measurement of a transverse energy imbalance. This method is less effective if more than one neutrino is produced as in $H \to \tau_{\text{had}}\tau_{\text{had}}$ decays. In this case the total MET $\not{E}_T$ is given by the transverse momentum of all neutrinos produced in the decay process and therefore it is impossible to reconstruct the momenta of distinct neutrinos produced in the decay.

The Missing Mass Calculator (MMC) [92] is an improved version of the collinear approximation [92, 93] and can be applied to any event topology. The collinear approximation determines $m_{\tau\tau}$ based on two assumptions: the MET in the event is only caused by invis-

ible neutrinos and the neutrinos are approximately collinear to the visible τ lepton decay products, since the τ leptons are highly boosted. Then, $m_{\tau\tau}$ is calculated by

$$m_{\tau\tau} = \frac{m_{vis}}{\sqrt{x_1 x_2}}, \tag{3.11}$$

where m_{vis} denotes the invariant mass of the visible decay products of the τ decay and x_i are the momentum fractions of the visible decay products for $i \in \{1, 2\}$ defined by

$$x_i = \frac{p_{vis_i}}{p_{vis_i} + \not{p}_i}, \tag{3.12}$$

where p_{vis_i} denotes the visible momentum and $\not{p}_i$ denotes the missing momentum. The mass resolution increases with a higher boost of the $\tau\tau$-system, so the collinear approximation is suitable if the Higgs boson is produced in association with hard jets leading to a boost of the $\tau\tau$-system.

The MMC is a likelihood-based tool providing a full reconstruction of the decay event topology originating from a $H \to \tau_{\text{had}}\tau_{\text{had}}$ decay to enable a good reconstruction of $m_{\tau\tau}$. Since there are two neutrinos in the final state in fully hadronic $H \to \tau_{\text{had}}\tau_{\text{had}}$ decays, there are in total six unknown components of the momentum vectors, $(p_x, p_y, p_z)_{\nu_i}$ for each neutrino $i = 1, 2$. These six unknowns are constrained by four quantities: the components of the missing transverse energy $\not{E}_x$ and $\not{E}_y$ and the masses of the decaying τ leptons m_{τ_1} and m_{τ_2}. This leads to an under-determined system of equations. To distinguish more likely solutions from all the other possible solutions, a weighting method based on information provided by the τ decay kinematics is used. More specifically, the MMC algorithm solves the system of equations for the momenta of the two neutrinos and the mass $m_{\tau\tau}$ at points of the $(\phi_{\nu_1}, \phi_{\nu_2})$ grid. For each solution, the three-dimensional angle $\Delta\theta$ between the visible τ lepton decay product and the neutrino ν, given by

$$\Delta\theta = \cos^{-1}\left(\frac{\vec{p}_\tau}{|\vec{p}|} \cdot \frac{\vec{p}_\nu}{|\vec{p}_\nu|}\right), \tag{3.13}$$

can be calculated for each τ lepton [94]. The results of these calculations are then compared to the probability density function (PDF) $\mathcal{P}_i$, which is obtained from simulated events. Using this PDF, each solution of $m_{\tau\tau}$ is reweighted by the probability of the decay event topology $\mathcal{P}$, given by $\mathcal{P} = \mathcal{P}_1 \times \mathcal{P}_2$, where $\mathcal{P}_i$ is an abbreviated notation for $\mathcal{P}(\Delta\theta_i, p_{T,i})$, where $i \in \{1, 2\}$. $\mathcal{P}$ can be used as an additional constraint in the calculation of $m_{\tau\tau}$. The best estimation of $m_{\tau\tau}$ can be obtained by producing distributions of $m_{\tau\tau}$ in which the entry of any scan point in the $(\phi_{\nu_1}, \phi_{\nu_2})$ space is weighted by its probability $\mathcal{P}$. The best estimate of $m_{\tau\tau}$, called $m_{\tau\tau}^{\text{MMC}}$, corresponds to the maximum of the weighted

distribution. To account also for MET resolution effects, resolution functions $\mathcal{P}(\not{E}_{x,y})$ are added to the PDF of the event by $\mathcal{P} = \mathcal{P}_1 \times \mathcal{P}_2 \times \mathcal{P}(\not{E}_x) \times \mathcal{P}(\not{E}_y)$, where the PDFs for the detector resolution $\mathcal{P}(\not{E}_{x,y})$ are given by

$$\mathcal{P}(\not{E}_{x,y}) = \exp(-\frac{(\Delta\not{E}_{x,y})^2}{2\sigma^2}), \tag{3.14}$$

where σ denotes the resolution [95] and $\Delta\not{E}_{x,y}$ is the difference between the measured $\not{E}_{x,y}$ and its value at the point in the parameter space.

3.4.3. Object Reconstruction in $H \to \tau_{\text{had}}\tau_{\text{had}}$

For the VBF Higgs boson production and the fully hadronic decay channel $H \to \tau_{\text{had}}\tau_{\text{had}}$, in particular good identification and reconstruction methods for jets as well as for missing transverse energy due to produced neutrinos in τ lepton decays are needed.

The identification of hadronic τ decays is based on information provided by the ID and energy deposits in the ECal and HCal. Jets are reconstructed using the anti-k_t algorithm [91], described in detail in Section 3.4.1, with a distance parameter $R = 0.4$. The anti-k$_T$ algorithm uses energy depositions in the CS as inputs. τ_{had} candidates have a signature similar to QCD jets. Therefore, Boosted Decision Trees (BDTs) are used to separate hadronically decaying τ leptons from QCD jets using information of the shower shape in the CS. A BDT is a machine learning technique to discriminate signal and background events by combining several observables into one single variable with a high signal-to-background separation power [96]. In addition, τ_{had} candidates are defined, due to conservation of electric charge in the decay, by an odd number of prongs, typically one or three prongs, which also is input into the BDTs. Based on the BDT output, three working points can be defined: tight, medium and loose, corresponding to different τ lepton identification efficiencies [97]. An overlap removal with respect to ΔR is added to increase the quality of the identification of objects with a geometric overlap and to avoid double-counting of detector signatures. The threshold of the value of ΔR depends on the objects where a geometric overlap is measured. The invariant mass of the $\tau\tau$-system $m_{\tau\tau}$ is reconstructed using the missing mass calculator (MMC) [92], described in Section 3.4.2.

4. Data and Monte Carlo Samples

This chapter presents the data and MC samples used in the presented analysis.

4.1. Data

The analysis uses data collected by the ATLAS detector in proton-proton collisions in 2015 and 2016 during Run 2 at the LHC at $\sqrt{s} = 13$ TeV. The collected data corresponds to an integrated luminosity of $L = 36.1$ fb^{-1}. The recorded data must be contained in the good-run-list of the ATLAS experiment, the list of events which satisfy the ATLAS data quality standards and are free of data defects, excluding, amongst others, events where the IBL within the ID was not fully operational and events originating from cosmic radiation.

4.2. Monte Carlo Samples

The same MC samples as in the SM coupling analysis [98] are used to simulate background and signal events produced using the ATLAS simulation infrastructure [80]. The important background processes are discussed in detail in Section 5.3. The generators for signal and background processes are summarised in Table 4.1. The Higgs boson production processes are generated corresponding to a Higgs boson mass of $m_H = 125$ GeV at $\sqrt{s} = 13$ TeV. The VBF, VH and ggF Higgs boson production processes are simulated by POWHEG combined with PYTHIA8 [81–85]. While POWHEG simulates Higgs boson production in hard processes at next-to-leading order (NLO), PYTHIA8 [85] is a generator that carries out simulations of the parton shower (PS), fragmentation and underlying events. The simulation of τ_{had} decays is provided by TAUOLA [99]. The irreducible $Z^0 \to \tau\tau$ background is simulated with SHERPA [86–89]. SHERPA is a general-purpose event generator and can simulate all SM and several BSM processes. The W+jets and di-boson backgrounds are also simulated with Sherpa. Top quark pair production background is simulated using a combination of POWHEG and PYTHIA6. The ATLAS detector response is simulated by GEANT4 [90].

Process	$\mathcal{M}$ generator	PS generator	σ [pb]	order
ggF	POWHEG	PYTHIA8	48.6	N3LO QCD + NLO EW
VBF	POWHEG	PYTHIA8	3.8	NNLO QCD + NLO EW
Z^0H	PYTHIA8	PYTHIA8	0.9	NNLO QCD + NLO EW
WH	PYTHIA8	PYTHIA8	1.4	NNLO QCD + NLO EW
ttH	aMC@NLO	PYTHIA8	0.5	NLO QCD + NLO EW
W+jets	SHERPA 2.2.1	SHERPA 2.2.1	22	NNLO
Z^0+jets	SHERPA 2.2.1	SHERPA 2.2.1	1992	NNLO
Top	POWHEG	PYTHIA6	253	NNLO
Di-Boson	SHERPA 2.2.1	SHERPA 2.2.1	95.4	NLO

Table 4.1.: Summary of the MC generators for the matrix element $\mathcal{M}$ and the parton shower (PS) used for simulating the main signal and background processes at $\sqrt{s} = 13$ TeV [98], the corresponding cross section σ [100, 101] for the 2015 and 2016 datasets and the order at which the processes are generated. The Higgs boson samples are simulated corresponding to a Higgs boson mass of $m_H = 125$ GeV.

5. Event Selection, Categorisation and Background Modelling

This chapter describes the cut-based (CB) event selection, the event categorisation and the background processes based on the SM coupling analysis [98]. Further, a cut on the MMC mass of the $\tau\tau$-system $m_{\tau\tau}^{\mathrm{MMC}}$, which is applied additionally in the VBF CP-analysis, is motivated and described.

5.1. Cut-Based Event Selection

To select the interesting $H \to \tau_{\mathrm{had}}\tau_{\mathrm{had}}$ events from all the collected data, a preselection is performed, followed by an event categorisation to split the selected events into a boosted- and a VBF-enriched region. The preselection region can be used to check the background modelling of the considered background processes, described in Section 5.3, while the event categorisation increases the signal significance in each channel. In this section, the visible decay products originating from a hadronic decay of a τ lepton, i.e. neutral and charged hadrons, are labelled as τ_{vis}.

To define the preselection region, the following cuts are applied, which are summarised in Table 5.1: Exactly two hadronically decaying τ_{vis} candidates which satisfy the tight threshold of the jet rejection BDT (tight ID) with transverse momenta $p_{T_{\tau_{0,\mathrm{vis}}}} > 40$ GeV (leading τ, τ_0) and $p_{T_{\tau_{1,\mathrm{vis}}}} > 30$ GeV (subleading τ, τ_1) are required. Selected events have to fulfil the double-hadronic $\tau\tau$-trigger requirements of ATLAS [79] corresponding to the data taking periods in 2015 and 2016, given by

- in 2015: HLT_tau35_medium1_tracktwo_tau25_medium1_tracktwo_L1TAU20IM_2TAU12IM
- in 2016: HLT_tau35_medium1_tracktwo_tau25_medium1_tracktwo

The trigger requirements in 2016 become more strict in comparison to 2015 due to an increased instantaneous luminosity L in 2016 by requiring, in addition to the p_T thresholds of the two leading τ candidates, a jet with $p_T > 25$ GeV and $|\eta| < 3.2$. The τ leptons originating from a Higgs boson decay must be reconstructed with opposite electric

charges q since the Higgs boson is an electrically neutral particle. Since both τ leptons decay hadronically, two invisible neutrinos ν are produced, leading to missing transverse energy $\not{E}_T$. The range of the opening angle ΔR between the τ_{vis} candidates is limited to $0.8 < \Delta R_{\tau_{0,\text{vis}},\tau_{1,\text{vis}}} < 2.4$ to reject QCD multi-jet events. To reject events with a bad mass resolution, a constraint on the momentum fractions $x_{1,2}$ of the collinear mass approximation, described in Section 3.4.2, defined by $0.1 < x_{1,2} < 1.4$, is added. In order to reject non-resonant background events, one requires $|\Delta\eta_{\tau_{0,\text{vis}},\tau_{1,\text{vis}}}| < 1.5$. Further an orthogonal selection with respect to the leptonic decay channels of the Higgs boson daughter particles is introduced by a veto on the presence of electrons e and muons μ [97].

For the VBF CP analysis, it is useful to define a slightly modified version of the preselection region, called preselection with two jets, defined as the preselection region plus requiring at least two jets, which are an important feature of the VBF topology. The modelling of important kinematic variables in the preselection with two jets region are shown in Figure 5.1 and 5.2 and in Appendix C.1.

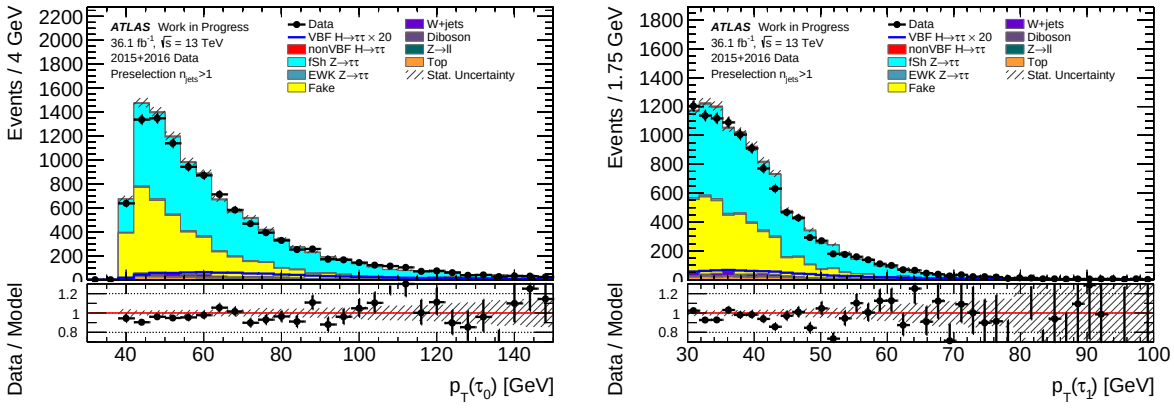

Figure 5.1.: Distribution of the transverse momentum p_T of the leading and subleading τ leptons in the preselection with two jets region.

5.2. Event Categorisation

To increase the sensitivity, events passing the preselection are categorised into the VBF region and the boosted region, as sketched in Figure 5.3, whereby the VBF categorisation is the first in the selection chain. The VBF region includes events where the Higgs boson candidate is mainly produced via VBF and the boosted region includes candidates in which the Higgs boson is produced in ggF with a recoiling hard jet leading to a boosted Higgs boson with high transverse momentum p_T^{Higgs}. Events which do not pass the VBF

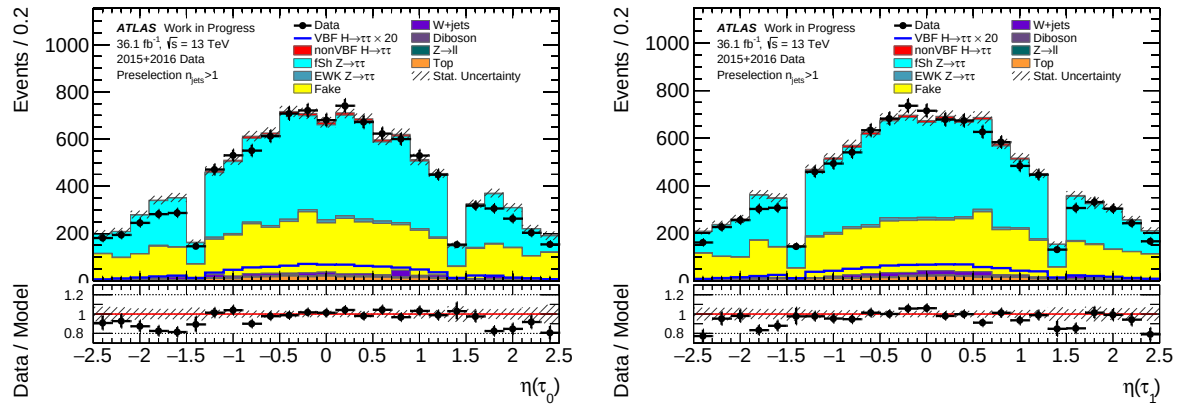

Figure 5.2.: Distribution of the pseudorapidity η of the leading and subleading τ leptons in the preselection with two jets region.

Preselection
$\tau\tau$-trigger
exactly two τ leptons satisfying tight ID
$p_{T,\tau_{0,\text{vis}}} > 40$ GeV
$p_{T,\tau_{1,\text{vis}}} > 30$ GeV
$q_{\tau_0} \cdot q_{\tau_1} = -1$
$\not{E}_T > 20$ GeV
$0.1 < x_{1,2} < 1.4$
$m_{\tau\tau}^{\text{MMC}} > 0.1$ GeV
$0.8 < \Delta R_{\tau_{0,\text{vis}},\tau_{1,\text{vis}}} < 2.5$
odd number of prongs (1 or 3)
veto on presence of e and μ
$\lvert\Delta\eta_{\tau_{0,\text{vis}},\tau_{1,\text{vis}}}\rvert < 1.5$

Table 5.1.: Cuts defining the preselection region.

or the boosted category selection are rejected. Since VBF is the Higgs boson production mechanism studied in this analysis, it will be discussed in more detail in the following.

In VBF Higgs boson production, the two scattered quarks lead to two hard jets with a large separation in η. This process provides a clean signature since, due to the electroweak character of this Higgs boson production process, little gluon radiation and thus a low jet activity in the central region of the ATLAS detector is expected, allowing for strong background-rejection. Since the coupling of massless photons to the Higgs boson are loop-induced and thus supressed, the contribution of photons in VBF Higgs boson production within the SM can be neglected. In contrast, as mentioned in Section 2.5, in BSM scenarios where the Higgs boson is not purely CP-even, contributions from photons in the VBF process must be considered [102]. To define the inclusive VBF region, several

VBF
$p_{T,\text{jet}_0} > 70$ GeV
$p_{T,\text{jet}_1} > 30$ GeV
$\lvert\Delta\eta_{\text{jet}_1,\text{jet}_2}\rvert > 3$
$m_{\text{jet}_0,\text{jet}_1} > 300$ GeV
$\eta_{\text{jet}_0} \cdot \eta_{\text{jet}_1} < 0$
$\eta_{\text{jet}_0} < \eta_{\tau_0} < \eta_{\text{jet}_1}$ or $\eta_{\text{jet}_1} < \eta_{\tau_0} < \eta_{\text{jet}_0}$
$\eta_{\text{jet}_0} < \eta_{\tau_1} < \eta_{\text{jet}_1}$ or $\eta_{\text{jet}_1} < \eta_{\tau_1} < \eta_{\text{jet}_0}$

Table 5.2.: Cuts specifying the VBF inclusive region.

kinematic cuts on each event of the dataset are applied based on the VBF topology. The cuts defining the inclusive VBF region, which are applied on top of the preselection, are summarised in Table 5.2. Two hard jets with transverse momenta of $p_{T,\text{jet}_0} > 70$ (leading jet, jet_0) and $p_{T,\text{jet}_1} > 30$ (subleading jet, jet_1) with $|\Delta\eta_{\text{jet}_0,\text{jet}_1}| > 3$ and $\eta_{\text{jet}_0} \cdot \eta_{\text{jet}_1} < 0$ are required. In addition, the invariant mass of the two leading jets must fulfil $m_{\text{jet}_0,\text{jet}_1} > 300$ GeV and the τ leptons have to lie between the two tagging jets in η. Plots of important kinematic variables can be found in Appendix C.2.

The inclusive VBF region is separated into three subdivisions to further increase the sensitivity. One separates the high p_T^{Higgs} VBF and the low p_T^{Higgs} VBF region. The latter region is further divided into the VBF low p_T^{Higgs} tight and VBF low p_T^{Higgs} loose region. Quantitatively, the VBF subregions are defined by the selection criteria given in Table 5.3. The latter cut in Table 5.3 corresponds to a straight line (diagonal cut) in the $m_{\text{jet}_0,\text{jet}_1}$-$|\Delta\eta_{\text{jet}_0,\text{jet}_1}|$ space of the di-jet system. This cut is motivated by the strong correlation of these two variables $|\Delta\eta_{\text{jet}_0,\text{jet}_1}|$ and $m_{\text{jet}_0,\text{jet}_1}$ for signal events in the VBF region, allowing to define VBF regions with different signal to background ratios.

cut	high p_T^{Higgs}	low p_T^{Higgs} tight	low p_T^{Higgs} loose
$\Delta R_{\tau_0,\tau_1}$	< 1.5	> 1.5	> 1.5
p_T^{Higgs}	>140 GeV	<140 GeV	<140 GeV
$m_{\text{jet}_0,\text{jet}_1}$		$> (-250 \cdot \lvert\Delta\eta_{\text{jet}_0,\text{jet}_1}\rvert + 1550)$	$< (-250 \cdot \lvert\Delta\eta_{\text{jet}_0,\text{jet}_1}\rvert + 1550)$

Table 5.3.: Definition of the VBF subregions: VBF high p_T^{Higgs} (low ΔR), VBF low p_T^{Higgs} tight (high ΔR tight) and VBF low p_T^{Higgs} loose (high ΔR loose).

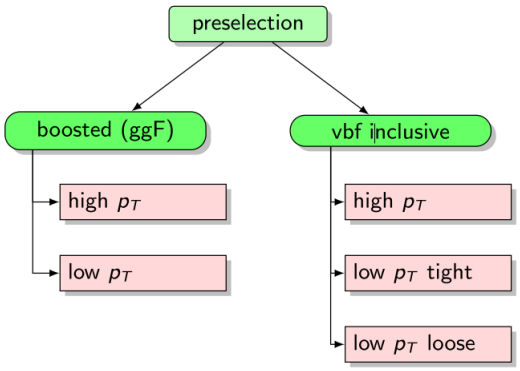

Figure 5.3.: Schematic view of the event categorisation used in the SM $H \to \tau_{\text{had}}\tau_{\text{had}}$ coupling analysis. After preselection, the VBF selection is the first in the selection chain. Events which do not pass the VBF nor the boosted selection criteria are rejected.

5.3. Background Processes and Modelling

There are several background processes which have to be studied and simulated when performing a $H \to \tau_{\text{had}}\tau_{\text{had}}$ analysis. The MC generators for simulating background processes are described in Section 4.2.

The largest and irreducible background originates from fully hadronic $Z^0/\gamma^* \to \tau\tau$ decays, which lead potentially to the same final state with similar topology as signal processes. $Z^0 \to \tau_{\text{had}}\tau_{\text{had}}$ and $H \to \tau_{\text{had}}\tau_{\text{had}}$ events produced in VBF can only effectively be distinguished by the invariant mass distribution $m_{\tau\tau}$, see Figure 5.7. In the VBF production mode, jet-p_T cuts can also lead to a separation of signal and background since most of the Z^0 bosons are not produced in VBF. Since the Higgs boson signal is expected to be located on the right tail of the Z^0 peak, a good reconstruction of the invariant mass is needed, which is problematic due to neutrinos produced in τ lepton decays. In addition, it is not possible to obtain a pure $Z^0 \to \tau\tau$ sample from data without signal events.

Additional background for τ_{had} candidates are hadronic jets (QCD jets), i.e. jets which originate from the hadronisation of quarks and gluons. Therefore, additional background for the $H \to \tau_{\text{had}}\tau_{\text{had}}$ analysis comes from events where at least one jet is misidentified as a τ lepton, e.g. electroweak, top quark and QCD processes. Processes where at least one jet is a misidentified τ lepton are divided into fake background and other background. The fake background consists of events where both τ lepton candidates are misidentified QCD jets. The fake background is estimated using data-driven techniques based on several control regions (CRs), defined in Table 5.4, which are obtained by altering at least one of the $\tau_{\text{had}}\tau_{\text{had}}$ event selection cuts: the τ_{had} candidates are required to be oppositely charged, have one or three tracks matched in $\Delta R < 0.2$ and fulfiling the tight identification working

name	$q(\tau_1) \cdot q(\tau_2)$	number of tracks	maximal ID of subleading τ_{had}
OS	$= -1$	$1, 3$	tight
nOS	$\neq -1$	$1, 2, 3$	tight
OS anti-ID medium	$= -1$	$1, 3$	medium
nOS anti-ID medium	$\neq -1$	$1, 2, 3$	medium
OS anti-ID loose	$= -1$	$1, 3$	loose

Table 5.4.: Summary of the signal region (OS) and control regions used in the SM coupling analysis.

point of the BDT. Since the nOS region provides the highest number of events, it is used to model the fake background: the templates for all variables for the fake background are determined by subtracting the processes with two real τ leptons from the data in this CR. Then, the fake templates of the nOS CR are reweighted to the OS anti-ID medium CR using the $\Delta\phi(\tau_0, \tau_1)$ distribution since the variable $\Delta\phi(\tau_0, \tau_1)$ propagates the differences between the nOS CR region and the OS anti-ID medium CR with the highest efficiency from all tested variables [98]. The OS anti-ID medium CR is the region closest to the OS signal region and is therefore used for the $\Delta\phi(\tau_0, \tau_1)$ reweighting.

Events where at least one real τ lepton is present in the final state are labelled as other backgrounds, e.g. $W^{\pm} \to \tau + \nu_\tau +$ jets, where one of the jets is falsely identified as a hadronic τ lepton decay. Further background contributions come from $t\bar{t}$ production, where a τ_{had} candidate occurs in the decay of the top quarks, and di-boson (VV) processes. These processes are also assigned as other background. Background events referred as other background are estimated using MC simulations. Drell-Yan background processes like $Z^0/\gamma^* \to e^+e^-$ and $Z^0/\gamma^* \to \mu^+\mu^-$ are more important in the leptonic final states of $H \to \tau\tau$ decays but also have a small proportion in the fully hadronic channel $H \to \tau_{\text{had}}\tau_{\text{had}}$. In contrast to the SM coupling analysis, the non-VBF Higgs boson production mechanism such as VH, ttH and ggF are not considered as signal processes for the CP study of the Higgs boson at the HVV vertex in VBF. Possible Feynman-diagrams of important background processes are displayed in Figures 5.4-5.6.

To model the background processes using MC samples, which are described in Chapter 4, a normalisation is obtained in the QCD fit region, which corresponds to the preselection region, defined in Section 5.1, but requiring $|\Delta\eta_{\tau_{0,\text{vis}},\tau_{1,\text{vis}}}| < 2$ rather than $|\Delta\eta_{\tau_{0,\text{vis}},\tau_{1,\text{vis}}}| < 1.5$. The background normalisation occurs by using a fit to the $|\Delta\eta_{\tau_{1,,\text{vis}},\tau_{2,,\text{vis}}}|$ distribution in the QCD fit region, which has a good separation between the fake background and the $Z^0 \to \tau\tau$ background.

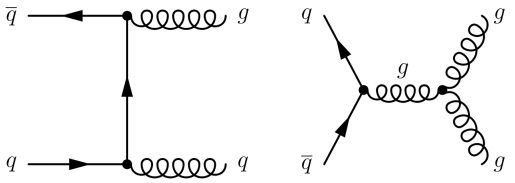

Figure 5.4.: Examples of Feynman-diagrams for QCD multi-jet background processes.

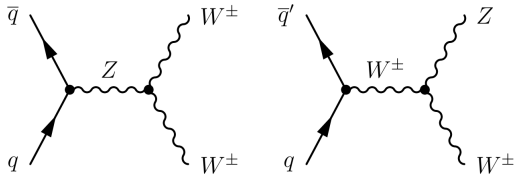

Figure 5.5.: Examples of Feynman-diagrams for di-boson background processes.

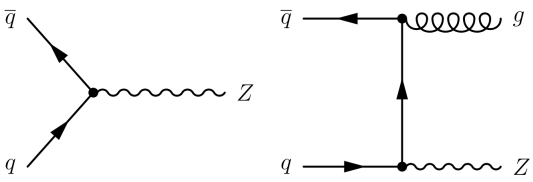

Figure 5.6.: Examples of Feynman-diagrams for Z^0 boson background processes.

5.4. Cut-Flow

The cut-flow for combined data from 2015 and 2016, based on the data and MC samples described in Chapter 4, are shown in the Tables 5.5 and 5.6. The cut-flow corresponds to the July 2017 version of the $H \to \tau_{\text{had}}\tau_{\text{had}}$ framework. The normalisation factors for the $Z^0 \to \tau\tau$ and the fake background are $r_{Z^0} = 0.77 \pm 0.02$ and $r_{QCD} = 0.83 \pm 0.04$, respectively. The VBF category contains mainly events where the Higgs boson candidate is produced via VBF but also contains small contributions from ggF, ttH and VH production. The boosted regions contain only a small amount of VBF events in comparison to ggF events and are not considered in the VBF CP analysis.

Cut	Fake	W+jets	Top	$Z^0 \to \tau\tau$	EWK $Z^0 \to \tau\tau$	VV+$Z^0\ell\ell$
QCD Fit	5993±80	311±28	238±10	8898±92	163.1 ±7.1	96.9±4.4
Preselection	5266±76	288±25	224.6±9.9	8821±91	160.5 ±7.0	95.3±4.1
Preselection $n_{\text{jets}} \geq 2$	3899±65	200±22	216.8±9.7	6313±70	153.4±6.9	87.4±3.9
VBF	281±17	18.9±6.8	10.4±2.0	337±14	25.7 ±2.4	3.3±0.4
VBF Low ΔR	24.8±6.8	3.7±2.4	2.2±1.0	142.8±6.8	14. 1±1.8	1.7±0.3
VBF High ΔR Tight	129±11	5.9±3.0	3.8±1.1	99.9±9.0	9. 7±1.5	0.8±0.2
VBF High ΔR Loose	128±11	9.3±5.6	4.5±1.4	94.4±7.8	1. 9±0.6	0.9±0.2
Boosted	2353±54	196±21	167.2±8.5	6031±58	113.2 ±6.2	69.7±2.5
Boosted Tight	287±24	50.4±9.9	28.2±3.5	2992±35	67.1 ±4.7	39.9±1.5
Boosted Loose	2066±48	145±19	139.1±7.7	3038±47	46.1 ±4.0	29.8±1.9

Table 5.5.: Event yields with statistical uncertainty of the background processes for all categories used in the CB SM $H \to \tau_{\text{had}}\tau_{\text{had}}$ coupling analysis.

Cut	VBF	ggF	ttH+VH	Data	Total Bkg
QCD Fit	52.7±0.4	168.7±2.6	18.9±3.0	15680±130	15700±130
Preselection	51.2±0.4	163.7±2.6	17.7±2.9	14850±120	14860±120
Preselection $n_{\text{jets}} \geq 2$	45.0±0.3	121.4±2.2	17.0±2.9	10620±10	10870±99
VBF	24.7±0.3	12.1±0.7	0.8±0.6	648±26	677±22
VBF Low ΔR	12.5±0.2	5.6±0.5	0.8±0.6	194±14	189±10
VBF High ΔR Tight	9.3±0.2	3.3±0.4	0.0±0.0	241±16	249±15
VBF High ΔR Loose	2.8±0.1	3.2±0.4	0.0±0.0	213±15	239±15
Boosted	20.5±0.2	110.7±2.1	16.7±2.9	9151±96	8929±83
Boosted Tight	10.6±0.2	56.2±1.5	9.4±2.1	3728±61	3464±44
Boosted Loose	9.9±0.2	54.6±1.5	7.3±1.9	5423±74	5465±70

Table 5.6.: Event yields with statistical uncertainty of the Higgs boson production processes, data and total background (Total Bkg), which is the sum of all background processes, for all categories used in the CB SM coupling analysis.

5.5. Optimisation of the Signal Significance in the VBF Regions

As described in Section 5.3, fully hadronic $Z^0 \to \tau\tau$ decays can only be effectively distinguished from fully hadronic $H \to \tau\tau$ decays by the distribution of the invariant mass of the $\tau\tau$-system $m_{\tau\tau}^{\text{MMC}}$. Therefore, to increase the sensitivity in the VBF regions in the VBF CP analysis, different $m_{\tau\tau}^{\text{MMC}}$ mass cuts in the interesting mass region 100 GeV $< m_{\tau\tau}^{\text{MMC}} <$ 155 GeV of the SM Higgs boson are tested. The blinded distributions of the MMC mass of the $\tau\tau$-system $m_{\tau\tau}^{MMC}$ are shown in Figure 5.7. Data is intentionally blinded to avoid a bias of the analysis. The lower mass cut is mainly fixed by the shape of the $Z^0 \to \tau\tau$ peak, while the upper mass cut is set by the width of the signal mass peak. The expected significance is calculated using the Asimov significance Z_{asim} [103] defined by

$$Z_{asim} = \sqrt{2((S+B)\log(1+\frac{S}{B}) - S)}, \tag{5.1}$$

where S and B denote the number of signal events, i.e. VBF $H \to \tau_{\text{had}}\tau_{\text{had}}$, and background events, respectively. The significances are calculated in the VBF inclusive region and in the three VBF subcategories, high p_T^{Higgs}, low p_T^{Higgs} tight and low p_T^{Higgs} loose. The event yields of signal and background are extracted from the corresponding cut-flow tables of the investigated signal region, see Appendix A.1. The calculated significances Z_{asim} with statistical error δZ_{asim} for each VBF regions in the mass window and further information can be found in Appendix B. The mass windows corresponding to the highest sensitivity Z_{asim} with statistical error in the VBF analysis categories are summarised in Table 5.7. By comparing the inclusive VBF region to the subcategories, it is conspicuous

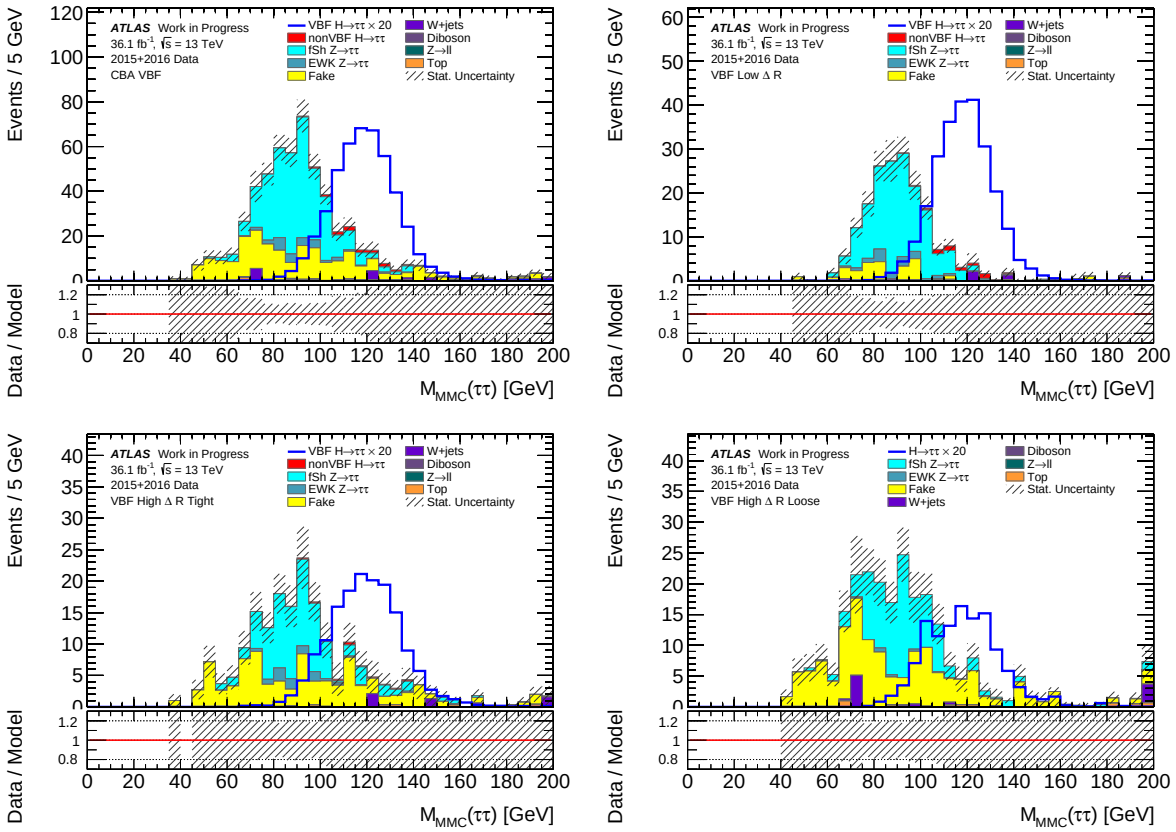

Figure 5.7.: Distribution of $m_{\tau\tau}^{\mathrm{MMC}}$ in the VBF inclusive, high p_T^{Higgs}, low p_T^{Higgs} tight and low p_T^{Higgs} loose region.

that most of the sensitivity originates from the VBF high p_T^{Higgs} region, while the low p_T^{Higgs} categories have low sensitivities.

It is useful to use a uniform mass window for each VBF region. Therefore, the mass window $[110, 140]$ is used for the VBF inclusive region as well as for the three VBF subregions (high p_T^{Higgs}, low p_T^{Higgs} loose and low p_T^{Higgs} tight) since this mass window provides more events in each channel than the alternative mass window $[115, 135]$. The Asimov sensitivities Z_{asim} for each VBF region in the mass range $[110, 140]$ GeV are

VBF region	mass window [GeV]	Z_{asim}
inclusive	$[110, 140]$	$1.89^{+0.09}_{-0.11}$
high p_T^{Higgs}	$[115, 135]$	$2.33^{+0.30}_{-0.49}$
low p_T^{Higgs} tight	$[115, 135]$	$1.01^{+0.11}_{-0.16}$
low p_T^{Higgs} loose	$[110, 140]$	$0.37^{+0.04}_{-0.04}$

Table 5.7.: VBF regions with mass cut corresponding to the highest Asimov significance Z_{asim} with statistical error.

VBF region	mass window [GeV]	Z_{asim}
inclusive	$[110, 140]$	$1.89^{+0.09}_{-0.11}$
high p_T^{Higgs}	$[110, 140]$	$2.16^{+0.17}_{-0.23}$
low p_T^{Higgs} tight	$[110, 140]$	$0.96^{+0.07}_{-0.09}$
low p_T^{Higgs} loose	$[110, 140]$	$0.37^{+0.04}_{-0.04}$

Table 5.8.: Asimov signficance Z_{asim} in VBF regions in the mass window $[110, 140]$ GeV.

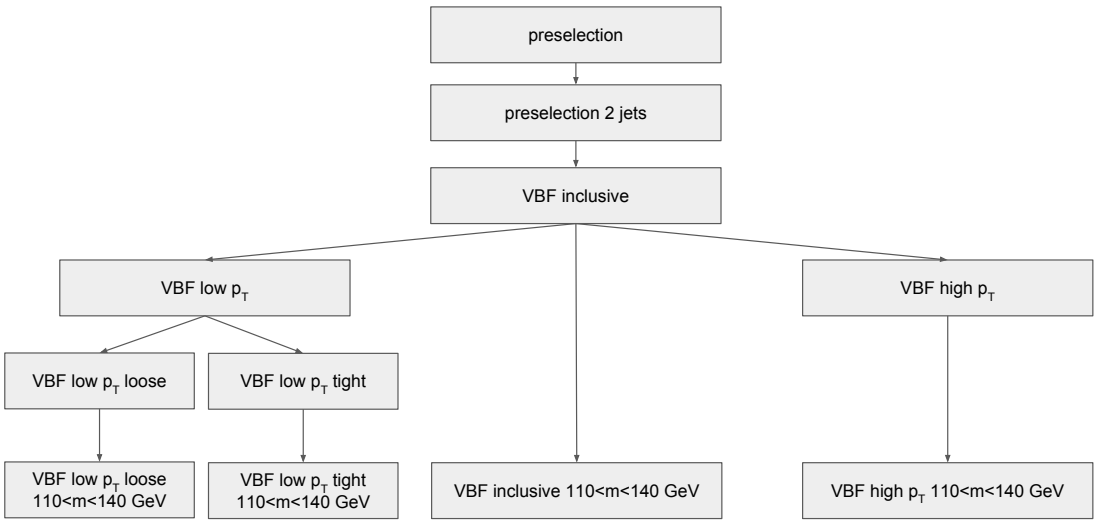

Figure 5.8.: Sketch of the important cut-stages used in the presented VBF Higgs CP analysis. In addition to the cuts used in the SM coupling analysis, a cut on the MMC Higgs boson mass $m_{\tau\tau}^{\text{MMC}}$ is implemented.

summarised in Table 5.8.

In the VBF inclusive region, most of the signal events are contained in the interval $[110, 140]$ GeV, see Figure 5.7. The mass cut $110 < m_{\tau\tau}^{\text{MMC}} < 140$ GeV causes most of the $Z^0 \to \tau\tau$, the QCD multi-jet and the top quark background to be rejected. In the VBF inclusive region and the low p_T^{Higgs} loose region also parts of the W+jets background are rejected. In the high p_T^{Higgs} region and in the low p_T^{Higgs} loose region, the mass cut does not effectively reject the W+jets background. In the high p_T^{Higgs} region, the mass cut $110 < m_{\tau\tau}^{\text{MMC}} < 140$ GeV rejects most of the fake background and $Z^0 \to \tau\tau$ events.

A sketch of the important cut-stages used in the VBF CP analysis is shown in Figure 5.8.

6. Investigation of the Optimal Observables and the Reweighting Procedure

In this chapter the calculation of $\mathcal{O}_{1,2}$ as well as the reweighting procedure of $\mathcal{O}_{1,2}$ to simulate anomalous CP couplings of the Higgs boson are described.

6.1. Calculation of the Optimal Observables

The calculation of the matrix elements $\mathcal{M}_{\mathrm{SM}}$, $\mathcal{M}_{CP-\mathrm{odd}}$ and $\mathcal{O}_{1,2}$ at leading order (LO) are performed using code extracted from HAWK [104–107], a Monte Carlo generator for the production of Higgs bosons coupled to weak bosons. The input variables of this code are given in Table 6.1. To calculate $\mathcal{O}_{1,2}$, the four-vectors of the two tagging jets, the CM energy $\sqrt{s}$ and the Bjorken $x_{1,2}$ values of the incoming partons in the positive and negative z-direction are needed. Also, in order to ensure momentum conservation at the HVV vertex, the Higgs boson momentum four-vector p^{μ}_{Higgs} is needed. Based on the vectorial sum of the four-vectors of the Higgs boson and the two leading jets $p^{\mu}_{\mathrm{jet}_{1,2}}$ given by

$$p^{\mu}_{\mathrm{tot}} = p^{\mu}_{\mathrm{Higgs}} + p^{\mu}_{\mathrm{jet}_1} + p^{\mu}_{\mathrm{jet}_2}, \tag{6.1}$$

the Bjorken $x_{1,2}$ values are calculated by

$$x_{1,2} = \frac{M_{Hjj}}{\sqrt{s}} \exp(\pm y_{Hjj}), \tag{6.2}$$

where M_{Hjj} is the mass and y_{Hjj} is the rapidity of p^{tot}, respectively. Since the flavours of the incoming and outgoing partons taking part in the scattering process are unknown and cannot be measured experimentally, the matrix elements $\mathcal{M}$ are calculated by summing over all possible flavour combinations [14], written as $ij \to klH$, weighted by the leading-

output	input	description
$\mathcal{O}_{1,2}$	$\sqrt{s}$	center of mass energy
	$x_{1,2}$	Bjorken x for incoming parton in $\pm z$ direction
	$f(x_{1,2})$	PDF for incoming parton in $\pm z$ direction
	$p^{\mu}_{\text{jet}_1}$	momentum four-vector of leading jet
	$p^{\mu}_{\text{jet}_2}$	momentum four-vector of subleading jet
	p^{μ}_{Higgs}	momentum four-vector of Higgs boson

Table 6.1.: Input variables on reco-level for the calculation of $\mathcal{O}_{1,2}$ at LO using code extracted from HAWK.

order PDFs $f(x_{1,2})$, i.e.

$$|\mathcal{M}_{\text{SM}}|^2 = \sum_{i,j,k,l} f_i(x_1) f_j(x_2) |\mathcal{M}_{\text{SM}}^{ij\to klH}|^2 \tag{6.3}$$

$$\text{Re}(\mathcal{M}_{\text{SM}}^{*}\mathcal{M}_{CP-\text{odd}}) = \sum_{i,j,k,l} f_i(x_1) f_j(x_2) \cdot \text{Re}((\mathcal{M}_{\text{SM}}^{ij\to klH})^{*} \cdot \mathcal{M}_{CP-\text{odd}}^{ij\to klH}). \tag{6.4}$$

6.2. Reweighting Procedure

A reweighting method is applied to the SM $\mathcal{O}_{1,2}$ distribution to produce distributions of $\mathcal{O}_{1,2}$ for various values of $\tilde{d}$, denoted by $\mathcal{O}_{1,2}(\tilde{d})$. Due to limited computational resources this reweighting method is preferred over directly simulating signal events for different values of $\tilde{d}$ using Monte Carlo generators like VBFNLO [108] or MadGraph5 [109]. The reweighting method was validated in Run 1 [14, 102] and Run 2 [110]. The weight $w(\tilde{d})$ required for the reweighting method is given by the ratio of the CP-mixed matrix element squared $|\mathcal{M}(\tilde{d})|^2$ given by Equation (2.37), and the matrix element squared of the SM prediction $|\mathcal{M}_{\text{SM}}|^2$, i.e.

$$w(\tilde{d}) = \frac{|\mathcal{M}(\tilde{d})|^2}{|\mathcal{M}_{\text{SM}}|^2}. \tag{6.5}$$

The full truth-parton-level information of the MC samples to determine the weight factors $w(\tilde{d})$ is used. Since the MC samples, which are generated using the ATLAS software framework, are at next-to-leading order (NLO), the reweighting can also be performed at NLO. Possible LO and NLO final states for VBF Higgs boson production, displayed in Figure 6.1, are $qQ \to qQH$, $qQ \to qQgH$ and $gQ \to q\bar{q}QH$. The inputs for the HAWK routine which calculates the weights $w(\tilde{d})$ from the matrix elements $\mathcal{M}$ for a chosen value of $\tilde{d} = \tilde{d}_B$ are summarised in Table 6.2. The first incoming parton is defined as the

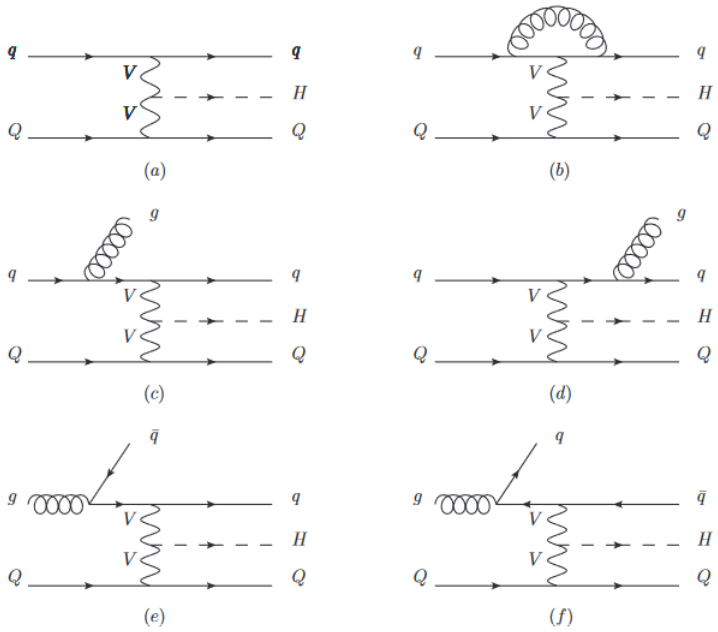

Figure 6.1.: Feynman diagrams contributing to VBF Higgs boson production ($V = W^{\pm}, Z^0$) at NLO showing leading order (a), virtual (b) and real emission (c-f) corrections [112]. The diagrams (c) and (e-f) show inital state radiation (ISR), while (d) displays final state radiation (FSR).

parton flying in positive z-direction, while the second incoming parton flies in negative z-direction. In the final state there are two or three outgoing partons, whereby, if existent, the third parton given to the code must be the gluon. The flavours f of the incoming and outgoing partons are defined by the particle-ID numbering scheme [111]. The Bjorken x values used for the reweighting are determined on parton-level by

$$x_i = \frac{2p_{z,i}}{\sqrt{s}}, \tag{6.6}$$

where $p_{z,i}$, $i \in \{1, 2\}$, denotes the z-component of the momenta of the two incoming partons, participating at the hard scattering.

However, the reweighting procedure can lead to large statistical fluctuations for events where the CP-odd contribution dominates the matrix element $\mathcal{M}$. Ideally, events with a weight factor $w(\tilde{d}) > 100$ are eliminated by the event selection or rather do not exist. However, a few events in the dataset with a weight $w(\tilde{d}) > 100$ can disturb the distribution of $\mathcal{O}_{1,2}(\tilde{d})$. To avoid such effects an additional cut on the weight factor $w(\tilde{d}) < 100$, which is used for the reweighting procedure, is applied. The corresponding cut-flow can be found in Appendix A.2. In the following, the weight cut is implicitly added in the VBF inclusive region as well as in the VBF subchannels (high p_T^{Higgs}, low p_T^{Higgs} loose, low p_T^{Higgs} tight)

output	input	description
	$\sqrt{s}$	center of mass energy
	$\vec{\alpha}(\tilde{d})$	set of numbers defining parametrisation of HVV coupling [113]
	$n_{p,fin}$	number of partons in final state (either two or three)
	$\vec{f}$	flavours of the incoming and outgoing partons
$w(\tilde{d})$	$x_{1,2}$	Bjorken x for incoming parton in $\pm z$ direction
	$p^{\mu}_{\text{parton}_1}$	momentum four-vector of final state parton 1
	$p^{\mu}_{\text{parton}_2}$	momentum four-vector of final state parton 2
	$p^{\mu}_{\text{parton}_3}$	momentum four-vector of final state parton 3 (gluon)
	p^{μ}_{Higgs}	momentum four-vector of Higgs boson

Table 6.2.: Input variables for the calculation of the weight factors $w(\tilde{d})$ at NLO using code extracted from HAWK assuming $\tilde{d} = \tilde{d}_B$. The weights $w(\tilde{d})$ are calculated at truth-level.

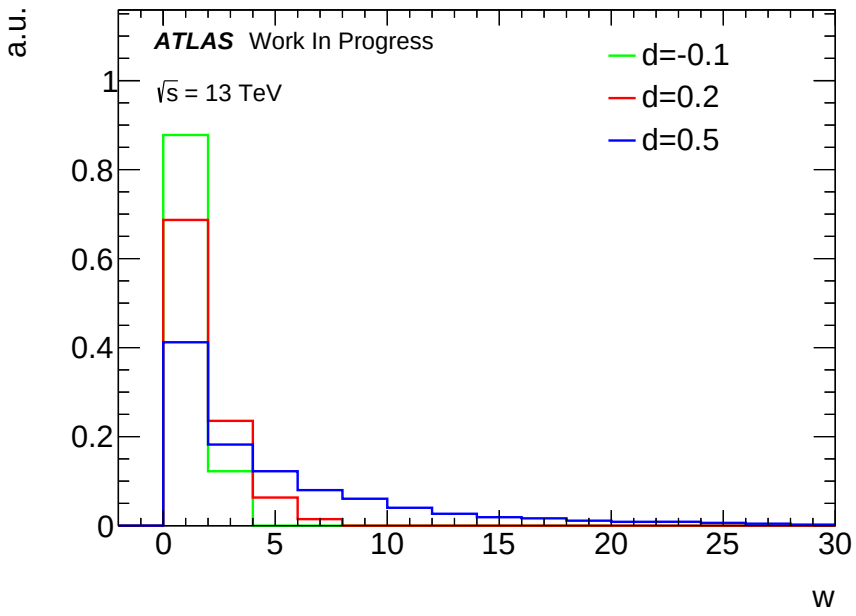

Figure 6.2.: Example distributions of the weight $w(\tilde{d})$ for $\tilde{d} = -0.1$ (green), $\tilde{d} = 0.2$ (red) and $\tilde{d} = 0.5$ (blue) in the VBF inclusive region.

unless it is explicitly specified that no weight cut is applied. Example distributions of the weight $w(\tilde{d})$ for $\tilde{d} \in \{-0.1, 0.2, 0.5\}$ are displayed in Figure 6.2.

6.3. Distribution of the Optimal Observables for Signal Only

The distributions of $\mathcal{O}_1$ and $\mathcal{O}_2$ for $\tilde{d} \in \{-0.5, 0, 0.2\}$ are shown in Figure 6.3. The distribution of $\mathcal{O}_1(\tilde{d} = 0)$ is not exactly symmetric with respect to $\mathcal{O}_1 = 0$ due to statistical fluctuations in the VBF signal regions. The shape of the $\mathcal{O}_2$ histogram is independent of the sign of $\tilde{d}$ since $\mathcal{O}_2$ is, in accordance with Equation (2.46), only sensitive to $\tilde{d}^2$. The reweighting of the $\mathcal{O}_2$ histogram leads to a shift of its mean towards larger values. For $\tilde{d} > 0$, the mean value $\langle \mathcal{O}_1 \rangle$ is shifted towards positive values, while for $\tilde{d} < 0$ $\langle \mathcal{O}_1 \rangle$ is shifted towards negative values. Also, the variance of the reweighted distribution changes for $\tilde{d} \neq 0$. This behaviour is quantified in Table 6.3. The dependency of $\mathcal{O}_1$ from $\tilde{d}$ is expected for small values of $\tilde{d}$ from theory since the mean value $\langle \mathcal{O} \rangle_1$ of the normalised $\mathcal{O}_1$ distribution can be written, using Equation (2.38), as

$$\langle \mathcal{O}_1 \rangle = \frac{1}{\int d\sigma} \int \mathcal{O}_1 d\sigma = \frac{\tilde{d} \cdot \int \mathcal{O}_1 d\sigma_{CP-\text{odd}}}{\int d\sigma_{\text{SM}} + \tilde{d}^2 \cdot \int d\sigma_{CP-\text{even}}}. \tag{6.7}$$

Equation (6.7) implies that $\langle \mathcal{O}_1 \rangle$ depends linearly on $\tilde{d}$ for sufficiently small values of $\tilde{d}$. Since $\langle \mathcal{O}_1 \rangle$ also depends on $\tilde{d}^{-2}$, the mean value $\langle \mathcal{O}_1 \rangle$ will vanish for a pure CP-odd scenario [56, 62].

The $\mathcal{O}_1$ distribution of the SM hypothesis ($\tilde{d} = 0$) exhibits a two-peak structure. As discussed in [102], the double-peak structure of the $\mathcal{O}_1$ distribution arises from the coupling of the Higgs boson to photons γ. If the photon couplings to the Higgs boson in VBF Higgs boson production are considered in the matrix element $\mathcal{M}$, which is obtained from the effective Lagrangian described in Equation (2.25), the CP-odd matrix element in Equation (2.36) becomes more important, reducing events with $\mathcal{O}_1 \approx 0$.

Scatter plots are used to investigate the correlation of $\mathcal{O}_{1,2}$ on reco- and truth-level. A high correlation of $\mathcal{O}_{1,2}$ on reco- and truth-level is crucial for the reweighting procedure since the weights $w(\tilde{d})$ are calculated on truth-level. The scatter plots visualizing the Optimal Observable on truth-level $\mathcal{O}_{1,2}^{\text{truth}}$ against $\mathcal{O}_{1,2}$ on reco-level for $\tilde{d} \in \{0.0, 0.2, -0.5\}$ are shown in Figures 6.4-6.6. $\mathcal{O}_{1,2}$ and $\mathcal{O}_{1,2}^{\text{truth}}$ are calculated using the first two leading jets fulfilling the VBF selection criteria and the reweighting is performed at NLO. The correlation factor α is used to quantify the correlation on reco- and truth-level, see Table

	$\tilde{d}$	$\langle\mathcal{O}\rangle$	σ
$\mathcal{O}_1$	0.0	0.013	3.772
	0.2	2.697	3.435
	-0.5	-1.73	4.425
$\mathcal{O}_2$	0.0	21.318	20.609
	0.2	27.330	32.020
	-0.5	31.54	23.684
$\mathcal{O}_1^{\text{truth}}$	0.0	0.013	3.717
	0.2	2.876	3.226
	-0.5	-1.8896	4.364
$\mathcal{O}_2^{\text{truth}}$	0.0	12.506	27.821
	0.2	27.821	23.478
	-0.5	32.243	23.666

Table 6.3.: Mean value $\langle\mathcal{O}\rangle$ and standard deviation σ of the $\mathcal{O}_{1,2}$ distributions on reco- and truth-level corresponding to $\tilde{d} \in \{0.0, 0.2, -0.5\}$.

6.4. The correlation of reco- and truth-level is for $\mathcal{O}_2$ slightly higher than for $\mathcal{O}_1$. There are small deviations between $\mathcal{O}_{1,2}$ and $\mathcal{O}_{1,2}^{\text{truth}}$ since events on reco-level include experimental influences like a limited detector resolution leading to a Gaussian smearing of the observed physical properties in comparison to truth-level events. It is also possible that on reco-level a gluon-initiated jet is falsely used for the calculation of $\mathcal{O}_{1,2}$, leading to larger deviations of $\mathcal{O}_{1,2}$ and $\mathcal{O}_{1,2}^{\text{truth}}$.

	$\tilde{d}$	α
$\mathcal{O}_1, \mathcal{O}_1^{\text{truth}}$	0.0	0.83
	0.2	0.87
	-0.5	0.759
$\mathcal{O}_2, \mathcal{O}_2^{\text{truth}}$	0.0	0.823
	0.2	0.88
	-0.5	0.87

Table 6.4.: Correlation factor α quantifying the correlation between $\mathcal{O}_{1,2}$ and $\mathcal{O}_{1,2}^{truth}$. The correlation of $\mathcal{O}_2$ is slightly higher than for $\mathcal{O}_1$.

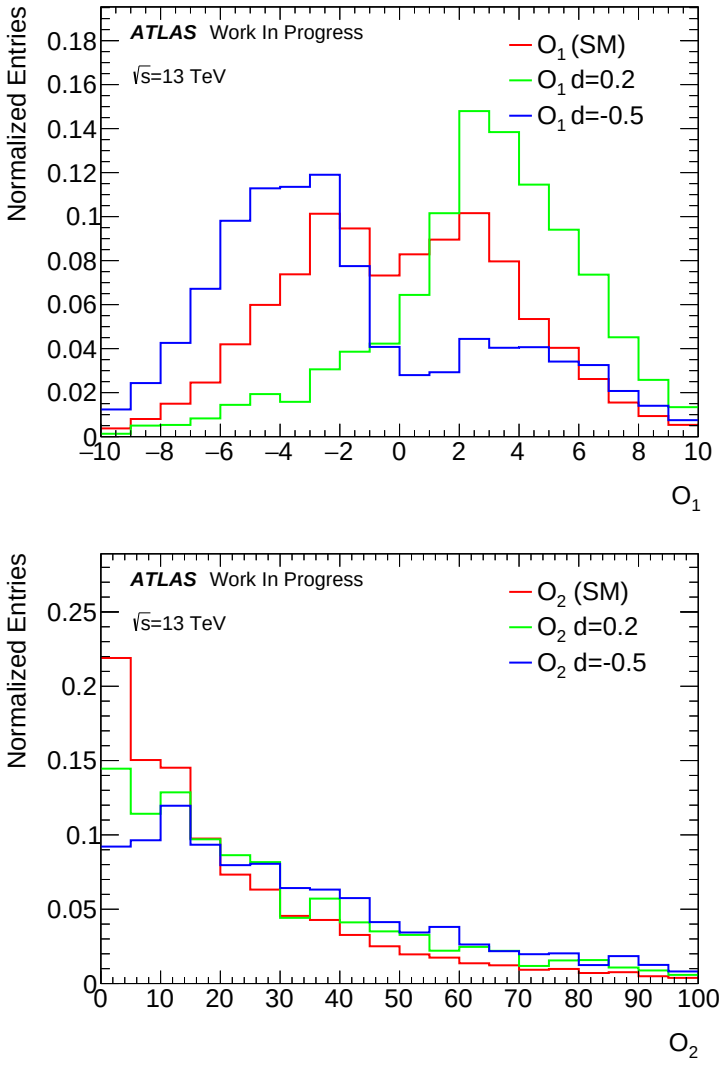

Figure 6.3.: Normalised distributions of $\mathcal{O}_1$ (left) and $\mathcal{O}_2$ (right) for the SM hypothesis of $\tilde{d} = 0$ (red) and reweighted corresponding to $\tilde{d} = 0.2$ (green) and $\tilde{d} = -0.5$ (blue) on reco-level.

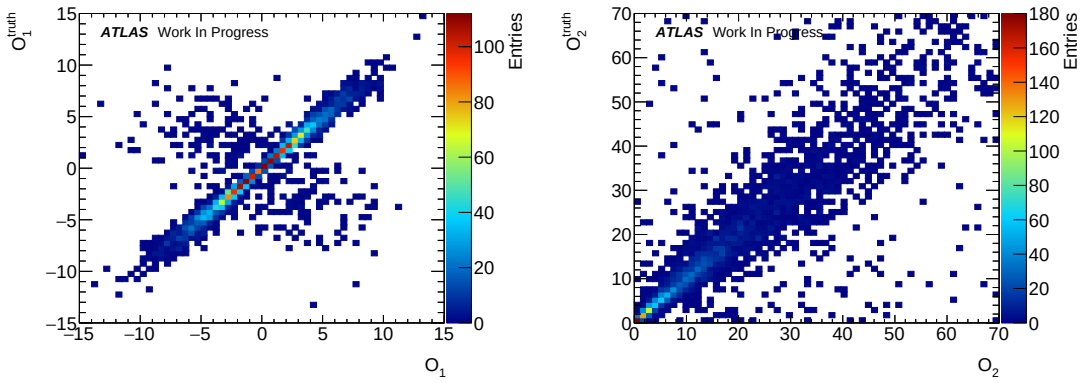

Figure 6.4.: Scatter plots showing the correlation of $\mathcal{O}_1$ (left) and $\mathcal{O}_2$ (right) on reco- and truth-level for the SM hypothesis of $\tilde{d} = 0$.

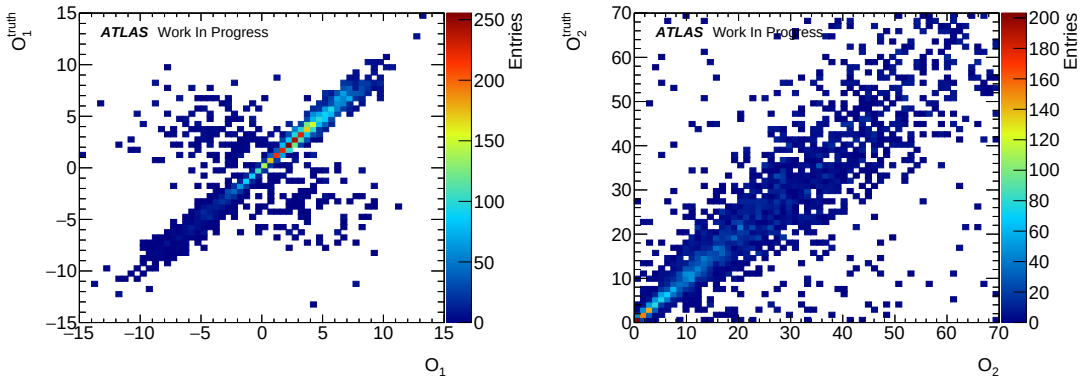

Figure 6.5.: Scatter plots showing the correlation of $\mathcal{O}_1$ (left) and $\mathcal{O}_2$ (right) on reco- and truth-level for the BSM hypothesis of $\tilde{d} = 0.2$.

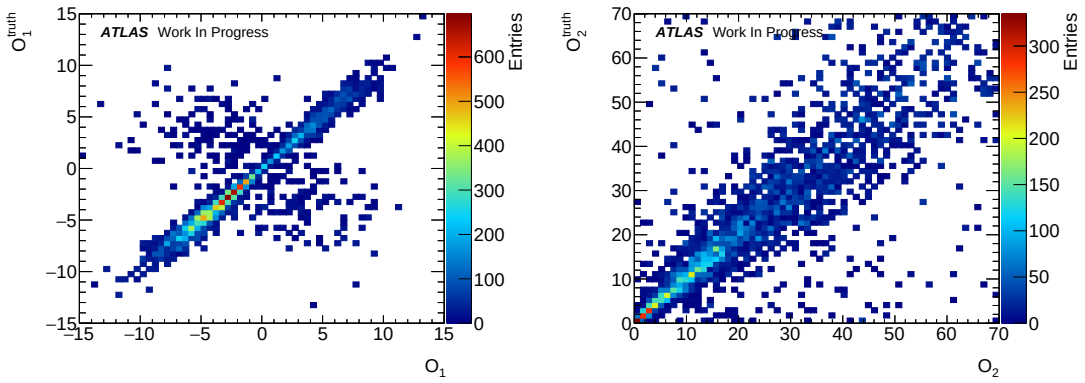

Figure 6.6.: Scatter plots showing the correlation of $\mathcal{O}_1$ (left) and $\mathcal{O}_2$ (right) on reco- and truth-level for the BSM hypothesis of $\tilde{d} = -0.5$.

7. The Optimal Observables in the VBF $H \to \tau_{\text{had}}\tau_{\text{had}}$ Channel

This chapter presents the distribution of $\mathcal{O}_1$ and $\mathcal{O}_2$ for signal and background processes. Also distributions of $\mathcal{O}_1$ and $\mathcal{O}_2$ after applying the mass cut $110 < m_{\tau\tau}^{\text{MMC}} < 140$ GeV are discussed.

7.1. Distributions of the Optimal Observables

The distribution of $\mathcal{O}_{1,2}$ is investigated after the preselection with two jets and in the VBF categories: inclusive VBF, high p_T^{Higgs}, low p_T^{Higgs} tight and low p_T^{Higgs} loose. The modelling of the distributions of important kinematic variables, in particular of those variables needed for the calculation of $\mathcal{O}_{1,2}$, are presented for the preselection with two jets and in the VBF inclusive region. The corresponding plots can be found in Appendix C.1 and C.2, respectively. The distributions of $\mathcal{O}_1$ and $\mathcal{O}_2$ are shown in Figures 7.1- 7.5 in different VBF regions.

In Figure 7.1, the distributions of $\mathcal{O}_1$ and $\mathcal{O}_2$ are shown in the preselection region with $n_{\text{jets}} \geq 2$, a region which is dominated by Z^0 and fake background events. The modelling of the shape of $\mathcal{O}_1$ and $\mathcal{O}_2$ is very good in this region.

The distribution of $\mathcal{O}_1$ in the VBF inclusive region is displayed in Figure 7.2. Data is intentionally blinded to avoid a bias of the analysis. It shows that most events of the $\mathcal{O}_1$ distribution are contained in the interval $[-10, 10]$ and the typical two-peak structure of the $\mathcal{O}_1$ distribution, which is discussed in Section 6.3, is visible when using a fine binning. The background is expected to have a mean value in the $\mathcal{O}_1$ distribution of zero since the background processes are CP invariant within the SM. The background in the $\mathcal{O}_1$ distribution in the VBF inclusive region and the VBF subregions is asymmetric with respect to the y-axis. The W+jets background is also highly asymmetric in the VBF regions except for the low p_T^{Higgs} tight region. The origin of the background asymmetry is not fully understood but it is assumed that statistical fluctuations in the background cause the observed asymmetry. The mean values of $\mathcal{O}_1$ of the signal and background processes

in the VBF regions are shown in Figure 7.6. The mean values in each region are consistent with $\langle \mathcal{O}_1 \rangle = 0$ within statistical uncertainties except for the W+jets background in the VBF inclusive region, in the VBF high p_T region and in the VBF low p_T loose region. Figure 7.3 shows that the high p_T^{Higgs} region is dominated by the $Z^0 \to \tau\tau$ background, while the low p_T^{Higgs} regions, see Figures 7.4 and 7.5, are dominated by both the fake and the $Z^0 \to \tau\tau$ background.

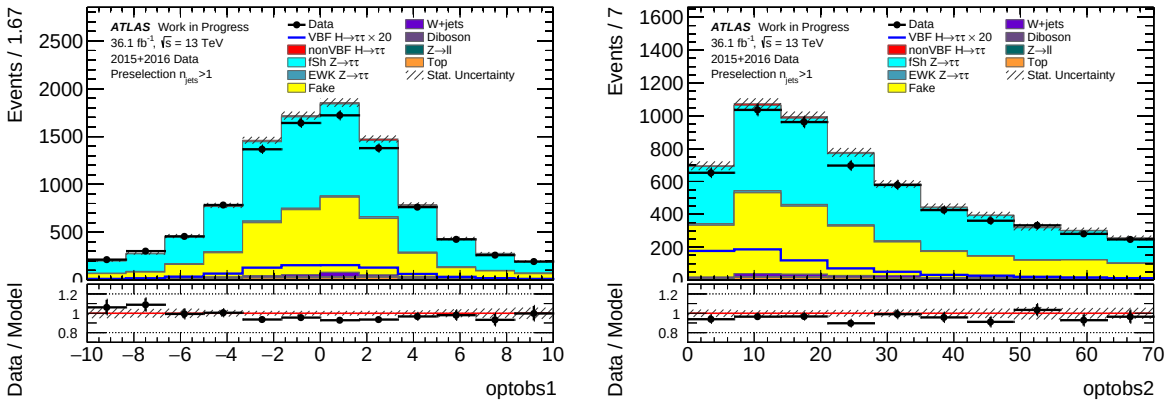

Figure 7.1.: Distribution of $\mathcal{O}_1$ (left) and $\mathcal{O}_2$ (right) in the preselection with $n_{\text{jets}} \geq 2$ region. The black dots represent the data.

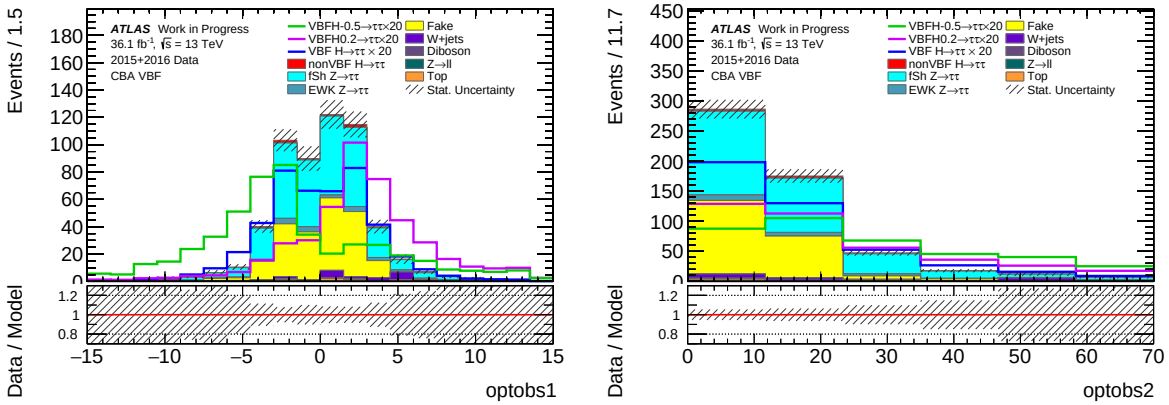

Figure 7.2.: Optimal Observable $\mathcal{O}_1$ (left) and $\mathcal{O}_2$ (right) in the VBF inclusive region. The SM signal process VBF $H \to \tau_{\text{had}}\tau_{\text{had}}$ (blue) is reweighted corresponding to $\tilde{d} = 0.2$ (violet) and $\tilde{d} = -0.5$ (black).

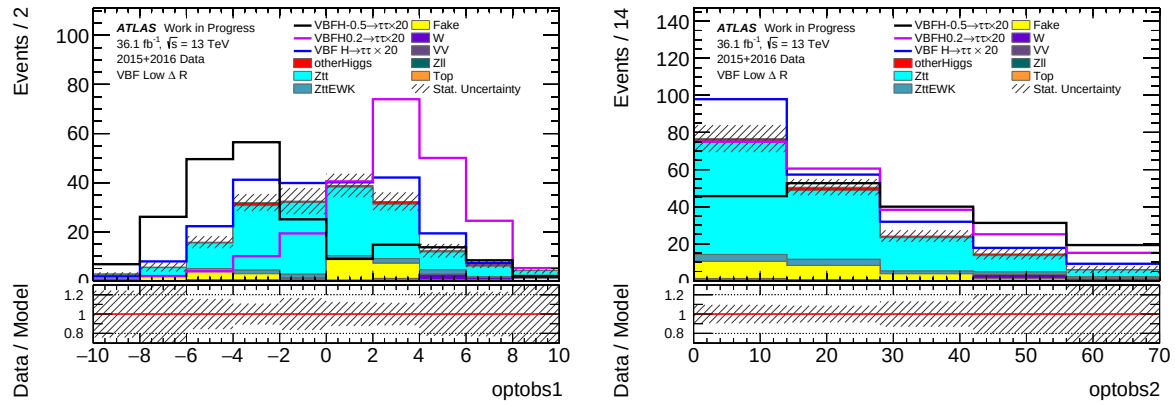

Figure 7.3.: Distribution of $\mathcal{O}_1$ (left) and $\mathcal{O}_2$ (right) in the high p_T^{Higgs} region. The SM signal process VBF $H \to \tau_{\text{had}}\tau_{\text{had}}$ (blue) is reweighted corresponding to $\tilde{d} = 0.2$ (violet) and $\tilde{d} = -0.5$ (black).

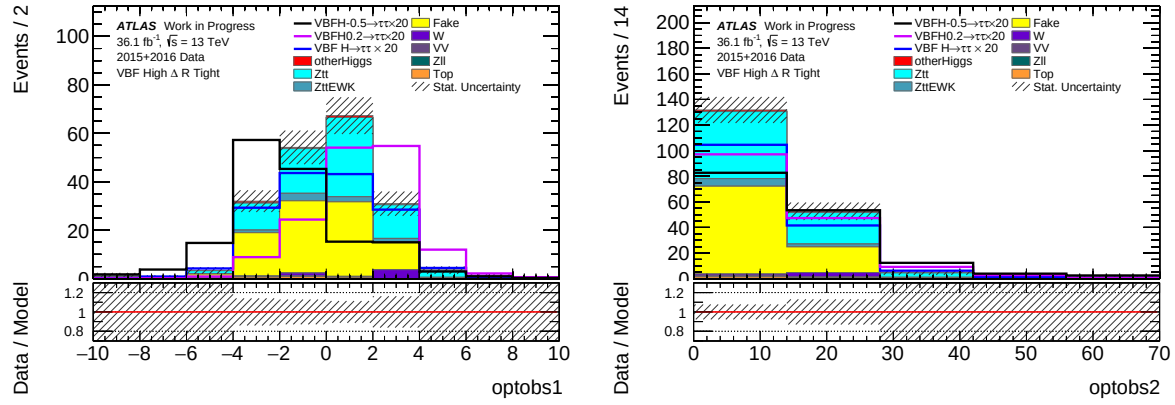

Figure 7.4.: Distribution of $\mathcal{O}_1$ (left) and $\mathcal{O}_2$ (right) in the VBF low p_T^{Higgs} tight region. The SM signal process VBF $H \to \tau_{\text{had}}\tau_{\text{had}}$ (blue) is reweighted corresponding to $\tilde{d} = 0.2$ (violet) and $\tilde{d} = -0.5$ (black).

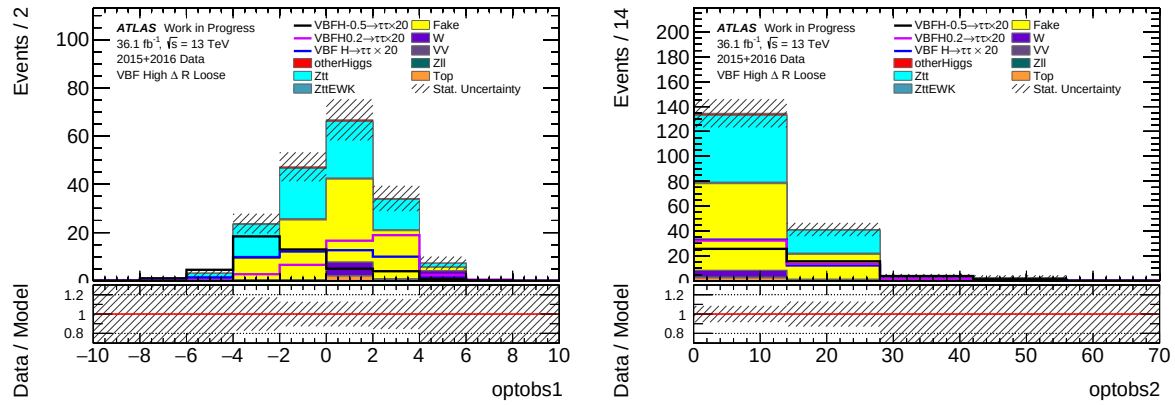

Figure 7.5.: Distribution of $\mathcal{O}_1$ (left) and $\mathcal{O}_2$ (right) in the VBF low p_T^{Higgs} loose region. The SM signal process VBF $H \to \tau_{\text{had}}\tau_{\text{had}}$ (blue) is reweighted corresponding to $\tilde{d} = 0.2$ (violet) and $\tilde{d} = -0.5$ (black).

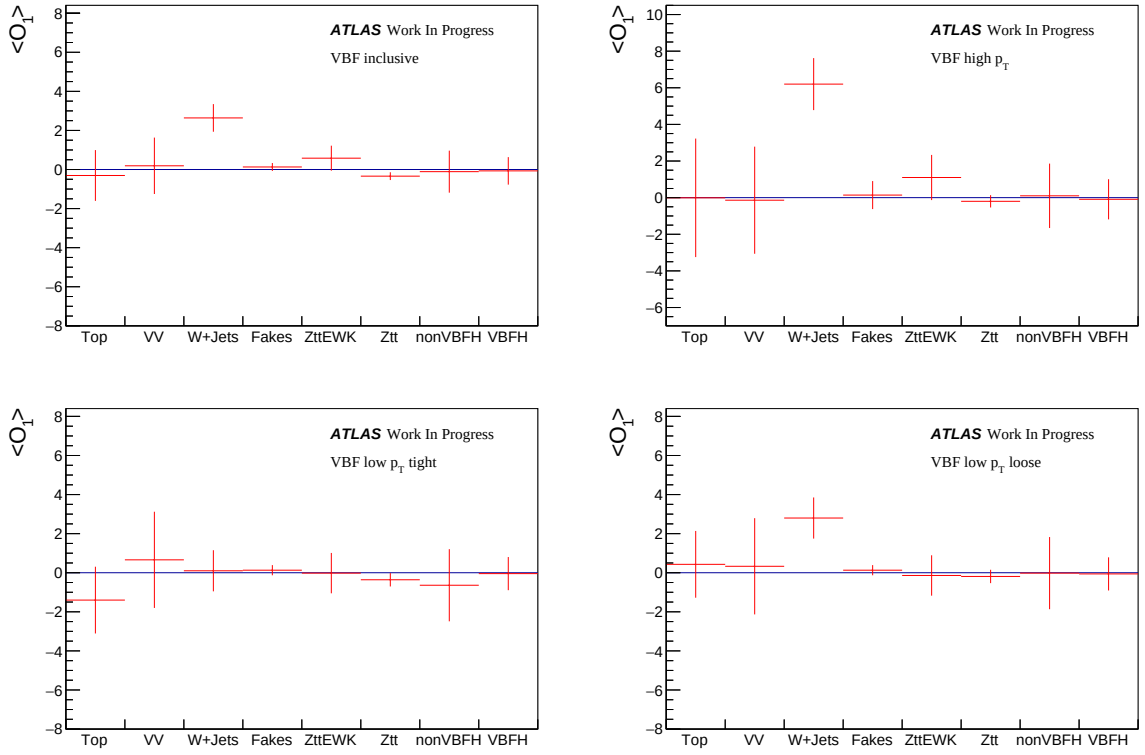

Figure 7.6.: Mean values with statistical uncertainty of the background and SM signal of the $\mathcal{O}_1$ histogram in the VBF regions.

7.2. Distributions of the Optimal Observables with Mass Cut

The mass window [110, 140] GeV was identified as the most sensitive common mass window of the VBF regions, as discussed in Section 5.5. The MMC mass of the $\tau\tau$-system $m_{\tau\tau}^{\mathrm{MMC}}$ is shown in Figure 5.7 in the VBF regions. The distributions of $\mathcal{O}_{1,2}$ in the VBF regions in the mass window [110, 140] GeV are shown in Figures 7.7-7.10. It is hard to make a shape prediction for $\mathcal{O}_1$ in these regions with low statistics, especially in the VBF subregions. The W+jets background is not significantly affected by applying the mass cut $110 < m_{\tau\tau}^{\mathrm{MMC}} < 140$ GeV in the high p_T^{Higgs} region, see Figure 7.8, and in the low p_T^{Higgs} tight region, see Figure 7.9, leading to an asymmetric background distribution. The mean values in the VBF regions for the most important background processes are shown in Figure 7.11. The background asymmetry of the W+jets background is statistically significant in all VBF regions except for the VBF low p_T^{Higgs} loose region. In addition, the fake background deviates statistical significant from $\langle \mathcal{O}_1 \rangle = 0$ in the VBF regions except for the VBF high p_T^{Higgs} region. In the low p_T^{Higgs} loose region also the top quark and the di-boson background significantly deviate from $\langle \mathcal{O}_1 \rangle = 0$.

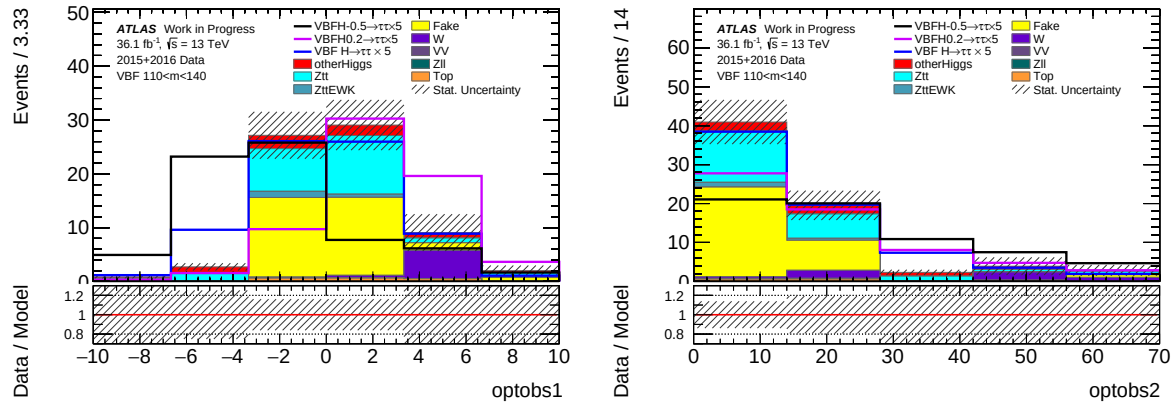

Figure 7.7.: Distribution of $\mathcal{O}_1$ (left) and $\mathcal{O}_2$ (right) in the mass window]110, 140] GeV in the VBF inclusive region. The SM signal process VBF $H \to \tau_{\mathrm{had}}\tau_{\mathrm{had}}$ (blue) is reweighted corresponding to $\tilde{d} = 0.2$ (violet) and $\tilde{d} = -0.5$ (black).

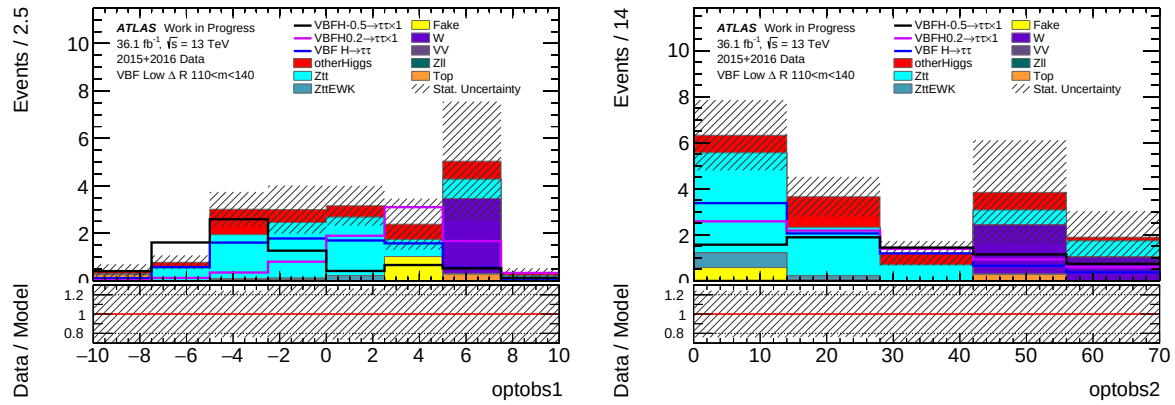

Figure 7.8.: Distribution of $\mathcal{O}_1$ (left) and $\mathcal{O}_2$ (right) in the mass window $]110, 140]$ GeV in the VBF high p_T^{Higgs} region. The SM signal process VBF $H \to \tau_{\text{had}}\tau_{\text{had}}$ (blue) is reweighted corresponding to $\tilde{d} = 0.2$ (violet) and $\tilde{d} = -0.5$ (black).

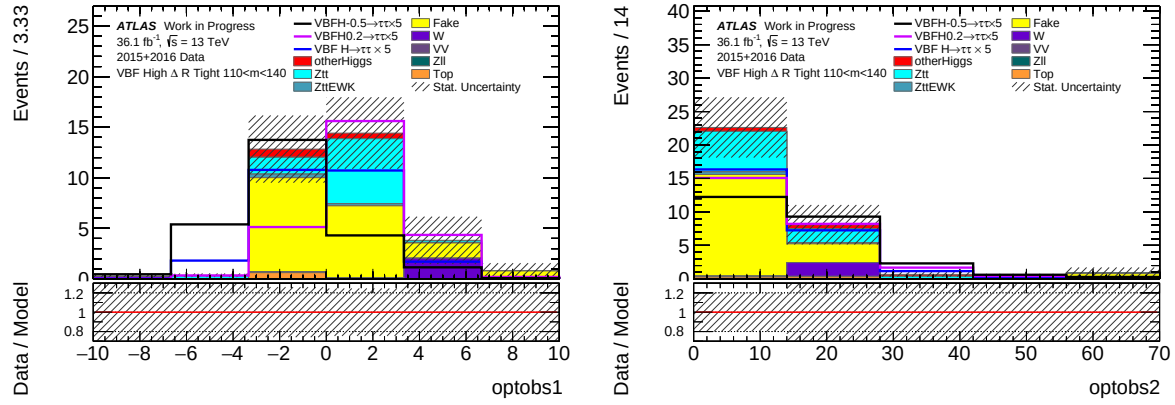

Figure 7.9.: Distribution of $\mathcal{O}_1$ (left) and $\mathcal{O}_2$ (right) in the mass window $]110, 140]$ GeV in the VBF low p_T^{Higgs} tight region. The SM signal process VBF $H \to \tau_{\text{had}}\tau_{\text{had}}$ (blue) is reweighted corresponding to $\tilde{d} = 0.2$ (violet) and $\tilde{d} = -0.5$ (black).

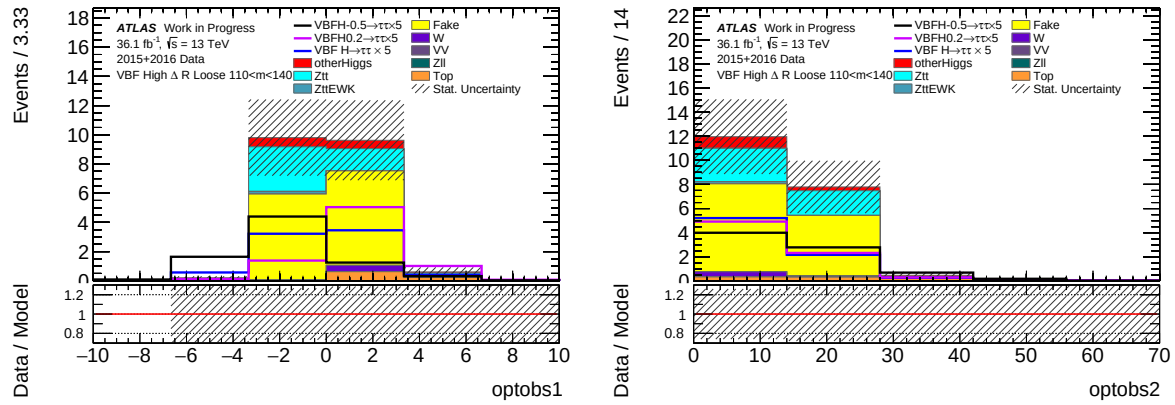

Figure 7.10.: Distribution of $\mathcal{O}_1$ (left) and $\mathcal{O}_2$ (right) in the mass window $]110, 140]$ GeV in the VBF low p_T^{Higgs} loose region. The SM signal process VBF $H \to \tau_{\text{had}}\tau_{\text{had}}$ (blue) is reweighted corresponding to $\tilde{d} = 0.2$ (violet) and $\tilde{d} = -0.5$ (black).

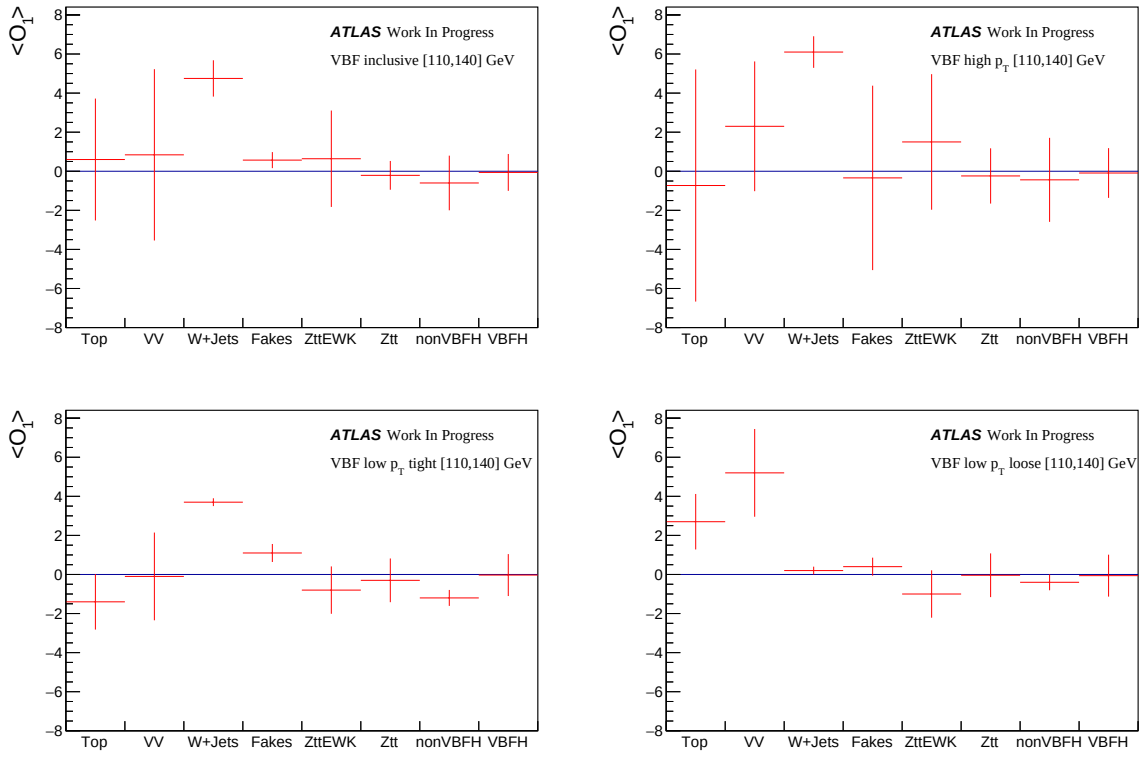

Figure 7.11.: Mean values with statistical uncertainty of the background and SM signal of the $\mathcal{O}_1$ histogram in the VBF inclusive region and the VBF subregions in the mass window $[110, 140]$ GeV, respectively.

8. Gauge Curves

Gauge curves (GCs) are a mapping of the mean value of the Optimal Observable distribution $\langle \mathcal{O}_{1,2}(\tilde{d}) \rangle$ against the underlying value of $\tilde{d}$ the distribution is reweighted to. Using a Neyman construction [114], GCs can be used for a sensitivity study of $\tilde{d}$ by translating the mean value $\langle \mathcal{O}_{1,2}(\tilde{d}) \rangle$ into a frequentist confidence interval (CI) on the parameter $\tilde{d}$. The CIs include by Neyman's construction the true value of the estimated parameter $\tilde{d}$ at the chosen coverage probability of 68% confidence level (CL).

8.1. Expected Shape of Gauge Curves

GCs are constructed as follows: Distributions of $\mathcal{O}_{1,2}$ are reweighted corresponding to several values of $\tilde{d}$. For each distribution, the mean value $\langle \mathcal{O}_{1,2} \rangle$ is determined and plotted against the corresponding value of $\tilde{d}$. For $\tilde{d} = 0$, the distribution of $\mathcal{O}_1$ is symmetric with $\langle \mathcal{O}_1 \rangle \approx 0$, implying $\lim_{\tilde{d} \to 0} \langle \mathcal{O}_1 \rangle \to 0$. For small values of $|\tilde{d}|$ such as $\tilde{d} \in [-1, 1]$, $\langle \mathcal{O}_1 \rangle$ is shifted as described in Section 6.2. Ideally, neglecting statistical fluctuations, the GCs for $\mathcal{O}_1$ are point-symmetric with respect to the origin, while the GCs for $\mathcal{O}_2$ are symmetrically identical with respect to a vertical line at $\tilde{d} = 0$. Looking at the asymptotic behaviour of $\langle \mathcal{O}_1 \rangle$, the CP-odd matrix element dominates the total matrix element $\mathcal{M}$ in Equation (2.36) for $|\tilde{d}| \to \infty$, as specified in Section 6.3, and the distribution of $\mathcal{O}_1$ is symmetric, i.e. $\lim_{\tilde{d} \to \infty} \langle O_1 \rangle \to 0$. Therefore, the method of using $\mathcal{O}_1$ for a study of the CP nature of the Higgs boson is in particular sensitive for sufficiently small values of $|\tilde{d}|$. GCs of $\mathcal{O}_2$ are not sensitive to the sign of $\tilde{d}$ and are expected to be less sensitive than the GCs which are based on the distribution of $\mathcal{O}_1$ for small values of $|\tilde{d}|$ since $\mathcal{O}_2$ depends on $\tilde{d}^2$, as described in Section 2.5.4.

8.2. Neyman Construction

For a sensitivity study of $\tilde{d}$ using Neyman's construction [114], GCs with CI based on statistical uncertainties of the bin content of the $\mathcal{O}_{1,2}$ distributions are produced. The CI of $\langle \mathcal{O}_{1,2} \rangle$ is determined by creating pseudo-data: SM distributions of $\mathcal{O}_{1,2}$ are produced

and reweighted corresponding to different values of $\tilde{d}$. The resulting histograms of $\mathcal{O}_{1,2}$ are used as a template for the pseudo-data distributions. Reweighted histograms are scaled according to the number of events of the signal histogram for the SM hypothesis ($\tilde{d} = 0$) corresponding to a luminosity $L = 36.1\ \text{fb}^{-1}$. 10000 toy-experiments are generated using the templates for each of the SM ($\tilde{d} = 0$) as well as the reweighted distributions ($\tilde{d} \neq 0$), assuming that the statistical uncertainties on the expected event yield in each bin of the histograms follow a Poisson distribution with mean according to bin content of the histograms scaled at the chosen luminosity. Thus, for every value of $\tilde{d}$ there exist 10000 histograms of $\mathcal{O}_{1,2}$ from which a histogram of the mean values $\langle\mathcal{O}_{1,2}\rangle$ against the underlying value of $\tilde{d}$ is constructed. Using this histogram, the mean value $\langle\mathcal{O}_{1,2}\rangle$ as well as the smallest symmetric range around this mean value which includes 68% of the events, which is the central CI of the mean value $\langle\mathcal{O}_{1,2}\rangle$, are extracted.

The Neyman construction is used to estimate the CI of $\tilde{d}$ for an assumed measurement of $\langle\mathcal{O}_{1,2}\rangle$, making a statement about the relative frequency such that the CI contains the true value of $\tilde{d}$ if the measurement is repeated equally many times. The confidence belt is made up of the $(\tilde{d}, \langle\mathcal{O}_{1,2}\rangle)$-pairs and the corresponding CIs of $\langle\mathcal{O}_{1,2}\rangle$. To get a sufficient estimation of the confidence belt, a small step size for the values of $\tilde{d}$, at least in the interesting region for small $|\tilde{d}|$, must be used. As described in Section 2.6, the Run 1 analysis excluded the regions $\tilde{d} > 0.05$ and $\tilde{d} < -0.11$ at 68% CL. Therefore, the investigation of GCs in this chapter focuses on small values of $|\tilde{d}|$, in particular on the range $\tilde{d} \in [-0.2, 0.2]$. As long as the data is blinded, the boundaries of the CI are determined by the intersection of the expected mean value $\langle\mathcal{O}_{1,2}^{\text{exp}}\rangle$ according to the SM prediction with the confidence belt. If there are more than two intersections of the expected mean value $\mathcal{O}_{1,2}^{\text{exp}}$ with the confidence belt, the overall CI is the union of the single CIs constructed from all intersections.

8.3. Gauge Curves for Signal Only

GCs are constructed as described in Section 8.2 for the VBF $H \to \tau_{\text{had}}\tau_{\text{had}}$ signal process only and background processes are not considered in this section. GCs for signal and background are described in Section 8.4. The confidence interval of $\tilde{d}$ is determined using $\mathcal{O}_1$ as well as $\mathcal{O}_2$ in the two most sensitive VBF regions, the VBF inclusive region and the VBF high p_T^{Higgs} region, with and without a mass cut of $[110, 140]$ GeV, respectively.

The GCs for $\mathcal{O}_1$ and $\mathcal{O}_2$ in the VBF inclusive region are shown in Figure 8.1. The Neyman construction leads to a 68% CI of $[-0.035, 0.047]$ for the SM expectation of $\langle\mathcal{O}_1\rangle = 0$ for $\tilde{d} = 0$. Figure 8.2 shows the corresponding signal only GCs in the VBF

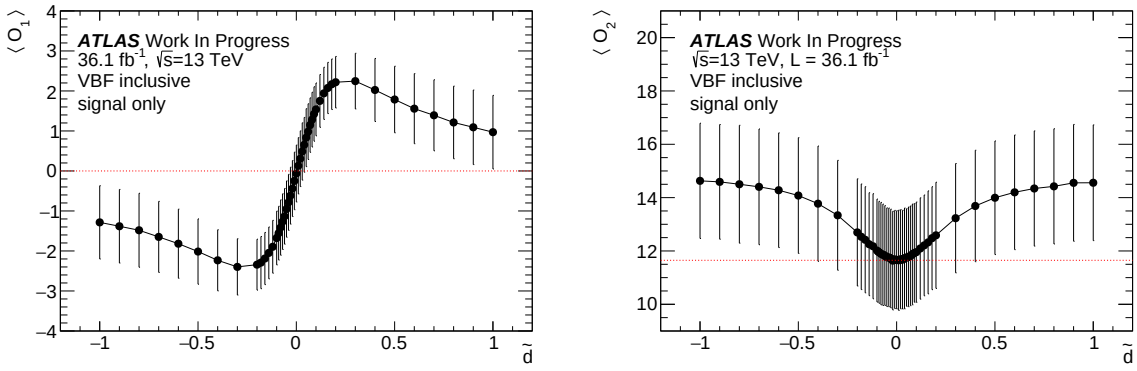

Figure 8.1.: GCs for $\mathcal{O}_1$ (left) and $\mathcal{O}_2$ (right) in the VBF inclusive region for the signal process and statistical uncertainty only.

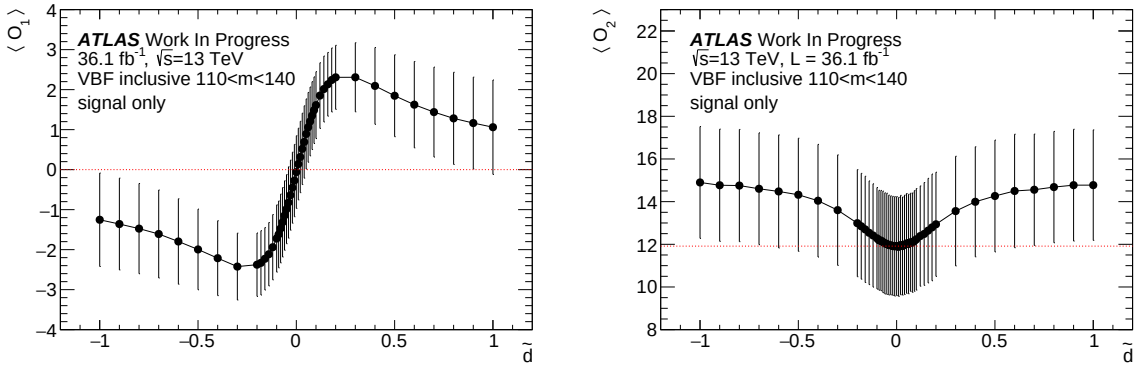

Figure 8.2.: GCs for $\mathcal{O}_1$ (left) and $\mathcal{O}_2$ (right) in the VBF inclusive region in the mass window $[110, 140]$ GeV for the signal process and statistical uncertainty only.

inclusive region with a mass cut $110 < m_{\tau\tau}^{\text{MMC}} < 140$ GeV applied. The expected CI for $\tilde{d}$ is $[-0.041, 0.043]$ at 68% CL for $\mathcal{O}_1$. For GCs using the signal process only, the expected sensitivity is not increased when applying a mass cut in the VBF inclusive region since in the VBF inclusive region with an additional mass cut, the statistical error of the mean values increases because this category includes less events than the VBF inclusive region without mass cut. The GCs for the VBF high p_T^{Higgs} region and the VBF high p_T^{Higgs} region in the mass window $[110, 140]$ GeV can be found in Figures 8.3 and 8.4. Since there are multiple intersectionss of $\langle \mathcal{O}_1^{\text{exp}} \rangle = 0$ with the corresponding confidence belt, exclusion limits can only be set in the VBF inclusive [110,140] GeV region, the VBF high p_T^{Higgs} region and the VBF high p_T^{Higgs} [110,140] GeV region for the signal only GCs. The estimated CIs are summarised in Table 8.1.

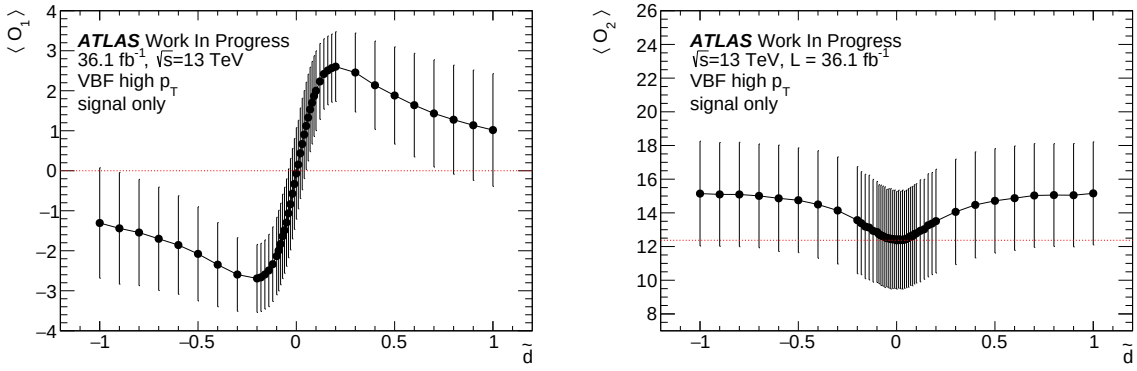

Figure 8.3.: GCs for $\mathcal{O}_1$ (left) and $\mathcal{O}_2$ (right) in the VBF high p_T^{Higgs} region for the signal process and statistical uncertainty only.

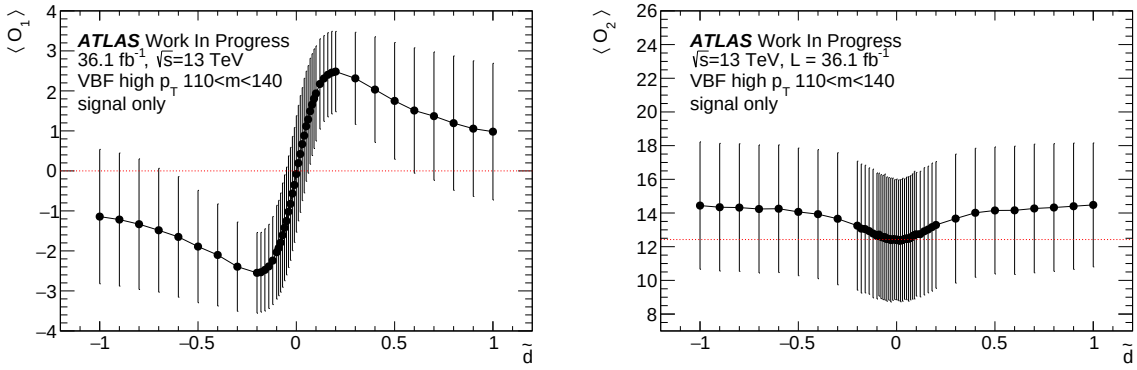

Figure 8.4.: GCs for $\mathcal{O}_1$ (left) and $\mathcal{O}_2$ (right) in the VBF high p_T^{Higgs} region in the mass window $[110, 140]$ GeV for the signal process and statistical uncertainty only.

VBF region	$\mathcal{O}_1$	$\mathcal{O}_2$
inclusive	$\tilde{d} \in$[-0.035,0.047]	$\tilde{d} \in$[-0.41,0.43]
inclusive $[110, 140]$ GeV	$\tilde{d} \notin ([-\infty, -0.05] \cup [0.05, 0.87])$	$\tilde{d} \in$[-0.67,0.68]
high p_T^{Higgs}	$\tilde{d} \notin ([-0.92, -0.06] \cup [0.06, 0.73])$	$\tilde{d} \in [-\infty, \infty]$
high p_T^{Higgs} $[110, 140]$ GeV	$\tilde{d} \notin ([-0.68, -0.06] \cup [0.07, 0.058])$	$\tilde{d} \in [-\infty, \infty]$

Table 8.1.: Summary of the expected 68% CI obtained from GCs considering the signal process only and using the statistical uncertainty only in the investigated VBF regions.

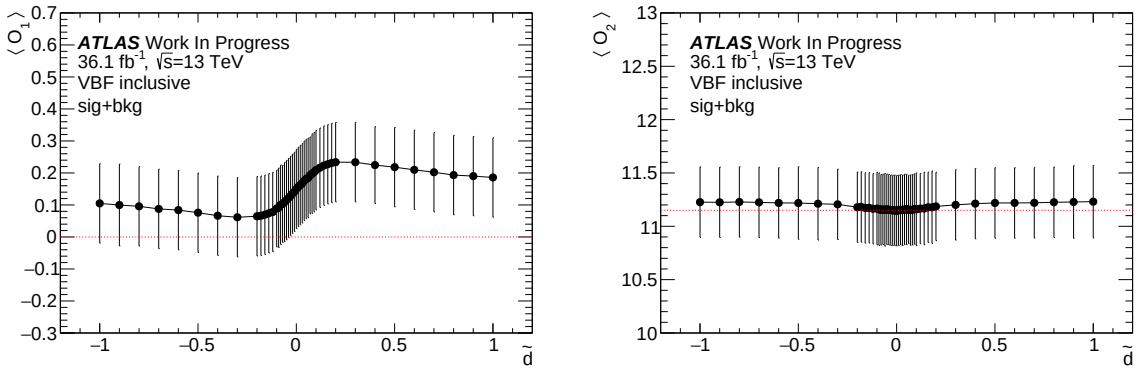

Figure 8.5.: GCs for $\mathcal{O}_1$ (left) and $\mathcal{O}_2$ (right) in the VBF inclusive region for signal and background processes and statistical uncertainty only.

8.4. Gauge Curves for Signal and Background

GCs considering both signal and background processes are investigated in this section. Signal and background histograms are filled into one single histogram, which is used as a template for creating the pseudo-data. In the same manner as for GCs using the signal process only, the VBF $H \to \tau_{\text{had}}\tau_{\text{had}}$ is reweighted and the background histograms are the same for each value of $\tilde{d}$. Therefore, the sensitivity decreases in comparison to GCs using the signal process only.

The GCs in the VBF inclusive region, the VBF inclusive region with mass cut, the VBF high p_T^{Higgs} region and the VBF high p_T^{Higgs} region with mass cut can be found in Figures 8.5-8.8. The GCs in the VBF inclusive region for signal and background processes are asymmetric with respect to $\langle\mathcal{O}_1\rangle = 0$ due to the asymmetric background distribution of the $Z^0 \to \tau\tau$ and W+jets background, see Chapter 7. Within the statistical uncertainty, the GCs in the VBF high p_T^{Higgs} region are consistent with the SM prediction of $\tilde{d} = 0$. Applying a mass cut in the VBF high p_T^{Higgs} region leads to a rejection of many background events but the highly asymmetric W+jets background is not rejected, resulting in an asymmetric GC.

Due to the asymmetric background in the $\mathcal{O}_1$ distributions, the GCs considering both signal and background processes are shifted towards positive values of $\langle\mathcal{O}_1\rangle$. Therefore, a sensitivity estimate using the Neyman construction is biased. In addition, the GCs for $\mathcal{O}_2$ for signal and background processes are expected to be not very sensitive to small values of $\tilde{d}$, which was also observed in the Run 1 analysis [61], and therefore also do not provide the possibility to estimate the 68% CI for $\tilde{d}$ using GCs considering both signal and background processes. Possible improvements of the sensitivity estimate with respect to $\tilde{d}$ using GCs are discussed in Chapter 10.

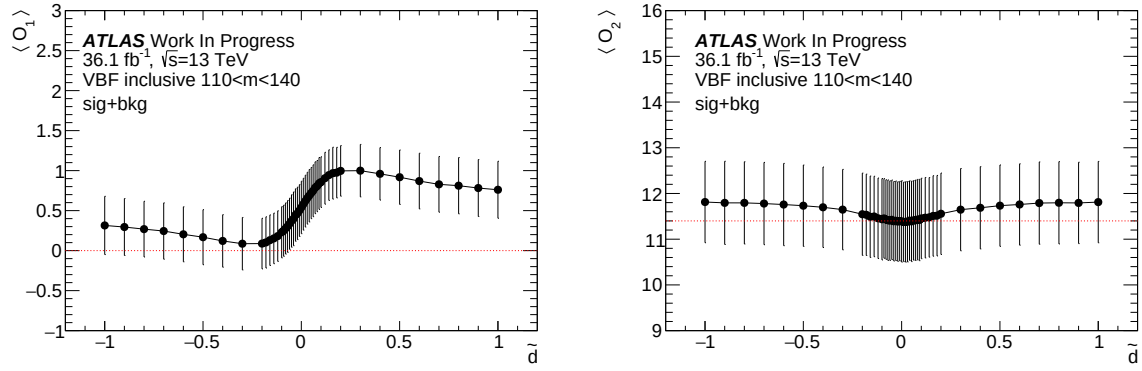

Figure 8.6.: GCs for $\mathcal{O}_1$ (left) and $\mathcal{O}_2$ (right) in the VBF inclusive region in the mass window $[110, 140]$ GeV for signal and background processes and statistical uncertainty only.

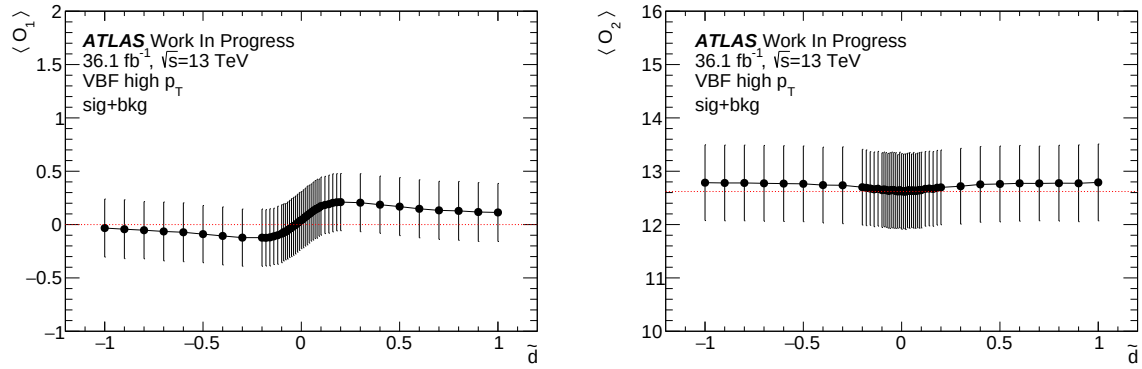

Figure 8.7.: GCs for $\mathcal{O}_1$ (left) and $\mathcal{O}_2$ (right) in the VBF high p_T^{Higgs} region for signal and background processes and statistical uncertainty only.

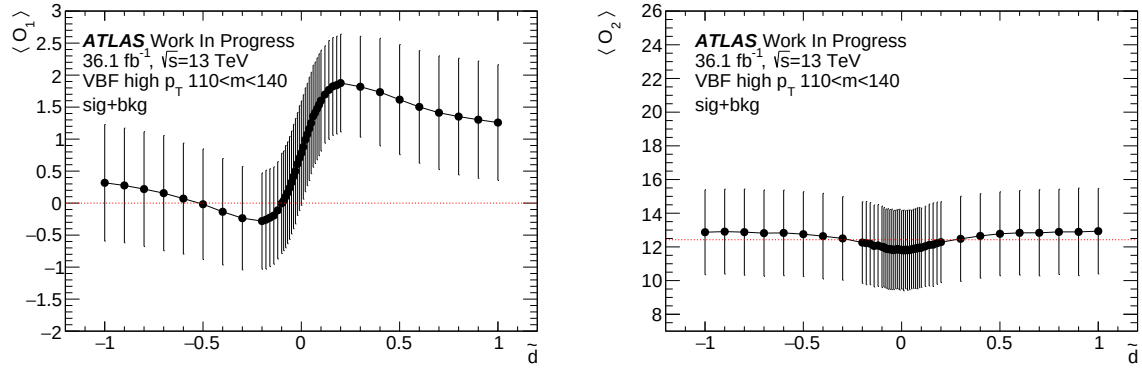

Figure 8.8.: GCs for $\mathcal{O}_1$ (left) and $\mathcal{O}_2$ (right) in the VBF high p_T^{Higgs} region in the mass window $[110, 140]$ GeV for signal and background processes and statistical uncertainty only.

9. Maximum Likelihood Fit

In Chapter 8, gauge curves are used for a sensitivity study with respect to $\tilde{d}$ in VBF Higgs boson production considering statistical uncertainties only. Another possibility to study the sensitivity with respect to $\tilde{d}$ is provided by a method called maximum likelihood (ML). In contrast to the method using gauge curves, the ML method is able to incorporate systematic uncertainties more easily in addition to statistical uncertainties.

9.1. The Maximum Likelihood Method

The ML method is an often used method in statistical data analysis for estimating unknown parameters. The statistical treatment and the general principle of the extended ML method for a binned distribution are explained in this section, while the fitting procedure used in this analysis to estimate the expected sensitivity with respect to $\tilde{d}$ is explained in Section 9.2.

In the following, S and B denote the number of expected signal and background events, respectively. Based on this, the signal strength μ is defined such that $\mu = 1$ if the number of observed events is equal to $S + B$ and $\mu = 0$ if the background only hypothesis is true. Let $f_S(x, \vec{\theta}, \tilde{d})$ and $f_B(x, \vec{\theta})$ be the probability density functions (PDFs) for signal and background, respectively, where x denotes the data sample and $\vec{\theta}$ describe nuisance parameters (NPs). Assuming Poisson distributions for the signal and background PDFs $f_S(x, \vec{\theta}, \tilde{d})$ and $f_B(x, \vec{\theta})$, the probability to observe n events can be obtained from the joint probability of $f_S(x, \vec{\theta}, \tilde{d})$ and $f_B(x, \vec{\theta})$ by

$$\mathcal{P}(x|\mu, \vec{\theta}, \tilde{d}) = \frac{\nu(\mu)^n}{n!} \exp(-\nu(\mu)) \prod_{j=1}^{n} \frac{\mu S f_S(x_j, \vec{\theta}, \tilde{d}) + B f_B(x_j, \vec{\theta})}{\nu(\mu)}, \tag{9.1}$$

where $\nu(\mu) = \mu S + B$ denotes the number of background and signal events scaled by the signal strength μ. In the following, the observed data are assumed to be fixed to estimate the unknown parameters μ and $\vec{\theta}$ from data. In terms of this interpretation, the probability described in Equation (9.1) is transformed into a likelihood function $\mathcal{L}$ defined as a product of conditional probabilities. The extended likelihood function is used for a

binned distribution, e.g. if the number of observed events n is itself a random variable following a Poisson distribution in each bin of a histogram. Using $\nu_i = \nu_i(\mu, \vec{\theta}, \tilde{d}) = \mu s_i(\vec{\theta}, \tilde{d}) + b_i(\vec{\theta})$ to describe the number of signal and background events in bin i, one finds

$$\mathcal{L}(n_i|\mu, \vec{\theta}, \tilde{d}) = \prod_i \frac{1}{n_i!} \nu_i^{n_i} \exp(-\nu_i) \tag{9.2}$$

where i run over the number of bins and n_i is the number of events in bin i. The negative logarithmic likelihood (NLL) function is defined as $-\log \mathcal{L}(n_i|\mu, \vec{\theta})$. In accordance with the ML principle, the best estimation of θ_i, written as $\hat{\theta}_i$, is the value which maximises the likelihood function or rather minimises the NLL function, i.e. $\log \mathcal{L}(\hat{\theta}) = \log \mathcal{L}_{\max}$. Based on the Cramér-Rao inequality, which defines a lower bound for the variance of an estimator of one parameter [103], the variance of a ML estimator $\hat{\theta}$ can be determined from the likelihood function by

$$\log \mathcal{L} = \log \mathcal{L}_{\max} - \frac{(\theta - \hat{\theta})^2}{2\sigma_{\hat{\theta}}^2}. \tag{9.3}$$

Therefore, based on the large sample limit where the NLL function becomes a parabola, the central CI $[\hat{\theta} - N\sigma_{\hat{\theta}}, \hat{\theta} + N\sigma_{\hat{\theta}}]$ for the estimator $\hat{\theta}$ is determined from the NLL function by

$$-\log \mathcal{L}(\hat{\theta} + N\sigma_{\hat{\theta}}) = -\log \mathcal{L}_{\max} + \frac{N}{2}, \tag{9.4}$$

where $N = \pm 1$ corresponds to the 68% CI and $N = \pm 2$ corresponds to the 95% CI for $\hat{\theta}$.

9.2. Fitting Procedure

In the following, the procedure to determine the expected sensitivity with respect to $\tilde{d}$ at 68% CL is described.

The gauge curves presented in Chapter 8 show that $\mathcal{O}_1$ is more sensitive than $\mathcal{O}_2$. In addition, a fit of $\mathcal{O}_2$ would not be a direct CP test since it is a CP-even observable. Therefore, the fit is performed using $\mathcal{O}_1$ as the discriminating variable.

For different BSM VBF signal hypothesis, i.e. for different values of $\tilde{d}$, a fit is performed by fitting the signal, scaled by the signal-strength μ, and the background to the Asimov data, a pseudo-dataset consisting of the sum of the expected background and the expected VBF Higgs boson signal corresponding to the SM CP-even hypothesis with $\tilde{d} = 0$. As mentioned in Chapter 7, real data is not revealed at this stage of the analysis to ensure an unbiased CP analysis. Therefore, an Asimov data set is used for the fit to determine

the expected sensitivity with respect to $\tilde{d}$.

The fit is only based on information given by the shape of the $\mathcal{O}_1$ distribution for each $\tilde{d}$ hypothesis and the analysis does not consider any information of the cross section σ of the investigated BSM scenarios, which is expected to depend quadratically on $\tilde{d}$, since the weighted VBF signal histograms are normalised to the SM prediction and the increasing cross section σ for $\tilde{d} \neq 0$ in comparison to the SM hypothesis may be an artefact of the chosen parametrisation of the effective Lagrangian described in Section 2.5.1.

The likelihood function $\mathcal{L}$ used for the fit can be written as a product of Poisson probabilities P, see Equation 9.2, and factors describing systematic uncertainties G_s by

$$\mathcal{L}(x|\tilde{d}, \mu, \vec{\theta}) = \prod_{ji}(P(N_{ij}|\mu_j S_{ij}(\tilde{d}, \vec{\theta}) + B_{ij}(\vec{\theta})) \prod_s G_s(\vec{\theta}), \tag{9.5}$$

where j runs over the signal and control regions, i runs over the bins of each histogram within the regions, s runs over the different sources of systematic uncertainties, x denotes the data sample, $\vec{\theta}$ are the NPs describing systematic uncertainties, see Section 9.3, and μ is the signal strength normalised to the SM prediction [115]. The systematic uncertainties are explicitly parametrised in $\mathcal{L}$ in terms of standard Gaussian distributions G_s describing the probability for each systematic, described by the corresponding NP, to be pulled away from the value predicted by the nominal histogram. The NLL is minimised with respect to μ and the NPs $\vec{\theta}$. The fake and $Z^0 \to \tau\tau$ background normalisation factors are allowed to freely float in the fit, where the starting values of the normalisation factors are the pre-fit normalisation values, described in Section 5.3. For each fit, the value of the NLL function is determined. It is customary to plot ΔNLL, defined by

$$\Delta\text{NLL} = \text{NLL} - \text{NLL}_{\text{min}}, \tag{9.6}$$

where $\text{NLL}_{\text{min}} = -\log \mathcal{L}_{\text{max}}$, against the underlying value of $\tilde{d}$. Thus, in accordance with Equation 9.4, the 68% CI of $\tilde{d}$ is determined from the curve showing ΔNLL against $\tilde{d}$ by reading off ΔNLL at 0.5.

The signal regions (SRs) are based on the discriminating observable $\mathcal{O}_1$. The CRs are used to constrain the NPs such as the background normalisation of $Z^0 \to \tau\tau$ and the fake background. Since the CRs are supposed to be approximately signal free, the $m_{\tau\tau}^{\text{MMC}}$ histograms in the VBF subchannels with a mass cut $m_{\tau\tau}^{\text{MMC}} < 110$ GeV are used as CRs. The likelihood fit is performed using two different fit regions. One fit is performed using the VBF inclusive region in the mass window $[110, 140]$ with a weight cut $w(\tilde{d}) < 100$ as fit region and the other fit is performed using the VBF subregions in the mass window $[110, 140]$ and with weight cut $w(\tilde{d}) < 100$ as fit region. The SRs and CRs used for the NLL

name	VBF signal region	VBF control region
VBF inclusive	inclusive $[110, 140]$ GeV	inclusive $m_{\tau\tau}^{\text{MMC}} < 110$ GeV
VBF subchannels	high p_T^{Higgs} $[110, 140]$ GeV	high p_T $m_{\tau\tau}^{\text{MMC}} < 110$ GeV
	low p_T^{Higgs} tight $[110, 140]$ GeV	low p_T^{Higgs} tight $m_{\tau\tau}^{\text{MMC}} < 110$ GeV
	low p_T^{Higgs} loose $[110, 140]$ GeV	low p_T^{Higgs} loose $m_{\tau\tau}^{\text{MMC}} < 110$ GeV

Table 9.1.: Signal and control regions used for the NLL fit.

fit are summarised in Table 9.1. In each fit region, a fit considering statistical uncertainties only and a fit considering statistical plus systematic uncertainties is performed.

The input histograms used in the fit are displayed in Figures 9.1 and 9.2. To obtain a high sensitivity with respect to $\tilde{d}$, an efficient binning of the histograms in the SRs and CRs must be used. Information is lost if the binning is too large, in contrast if the binning is too small, the histograms are fragile regarding statistical fluctuations in the data. For the SRs the binning $[-15, -5, -2.5, 0, 2.5, 5, 15]$ in $\tilde{d}$ is used and for the CRs the binning $[0, 65, 70, 75, 90, 95, 110]$ GeV in $m_{\tau\tau}^{\text{MMC}}$ is used.

9.3. Systematic Uncertainties

Uncertainties can in general be divided into statistical uncertainties and systematic uncertainties. The statistical uncertainty of a measurement arises from statistical fluctuations of the measured finite dataset. Thus, statistical fluctuations are usually uncorrelated. Systematic uncertainties are uncertainties arising from the structure of the experiment or uncertainties from theoretical approximations. Therefore, in contrast to statistical uncertainties, systematic uncertainties cannot be minimised directly by repeating the measurement many times.

Systematic uncertainties can be divided into experimental and theoretical systematic uncertainties. The most important experimental systematic uncertainties in association with the presented VBF CP analysis in the $H \to \tau_{\text{had}}\tau_{\text{had}}$ channel are explained in the following:

- Jets: In particular three important jet uncertainties, obtained from comparing 2015 and 2016 data to MC data, must be considered: Jet energy resolution (JER), jet energy scale (JES) and jet efficiency for the jet vertex tagger (JVT). The JVT is preliminary used for the identification and rejection of pile-up events [116]. The uncertainty on JES is derived using MC simulations considering uncertainties of in-situ jet energy calibration, η calibration, flavour composition and pile-up [117]. The

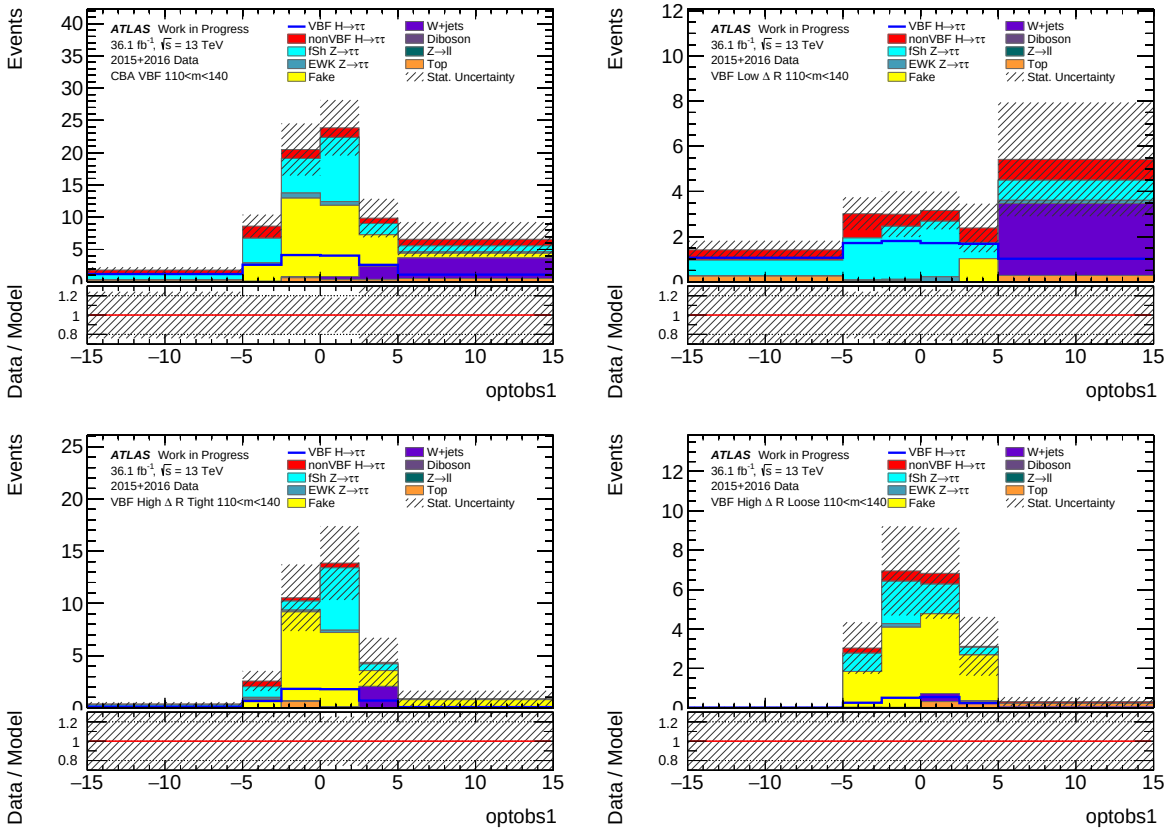

Figure 9.1.: Histograms of $\mathcal{O}_1$ in the SRs with the binning used in the final fit. One fit is performed using VBF inclusive with a mass cut $[110, 140]$ and a weight cut $w(\tilde{d}) < 100$ as fit region, while a second fit is performed in the VBF subregions in each case with a mass cut $[110, 140]$ GeV and a weight cut $w(\tilde{d}) < 100$.

JES depends in particular on p_T and η of the jet. The smallest JES uncertainty of less than 1% is reached in the central calorimeter region $|\eta| < 1.2$ for $p_T \in [100, 500]$ GeV, while the JES uncertainty is up to 3% for jets with high p_T [117].

- τ leptons: Important uncertainties come along with τ leptons such as the τ lepton energy scale uncertainty (TES) as well as the τ lepton identification and reconstruction efficiency uncertainties. The TES depends on the modelling of the ATLAS detector geometry and limited knowledge of the calorimeter response to jets and pions while the τ efficiency depends e.g. on uncertainties of the overlap removal and the $\tau\tau$ trigger system. The uncertainty in TES is asssumed to be 3%. The efficiencies of the τ lepton identification and the τ lepton energy calibration are measured using $Z^0 \to \tau\tau$ tag- and probe-measurements [97].

- MET: Systematic uncertainties arising from scale and resolution of $\not{E}_T$, correspond-

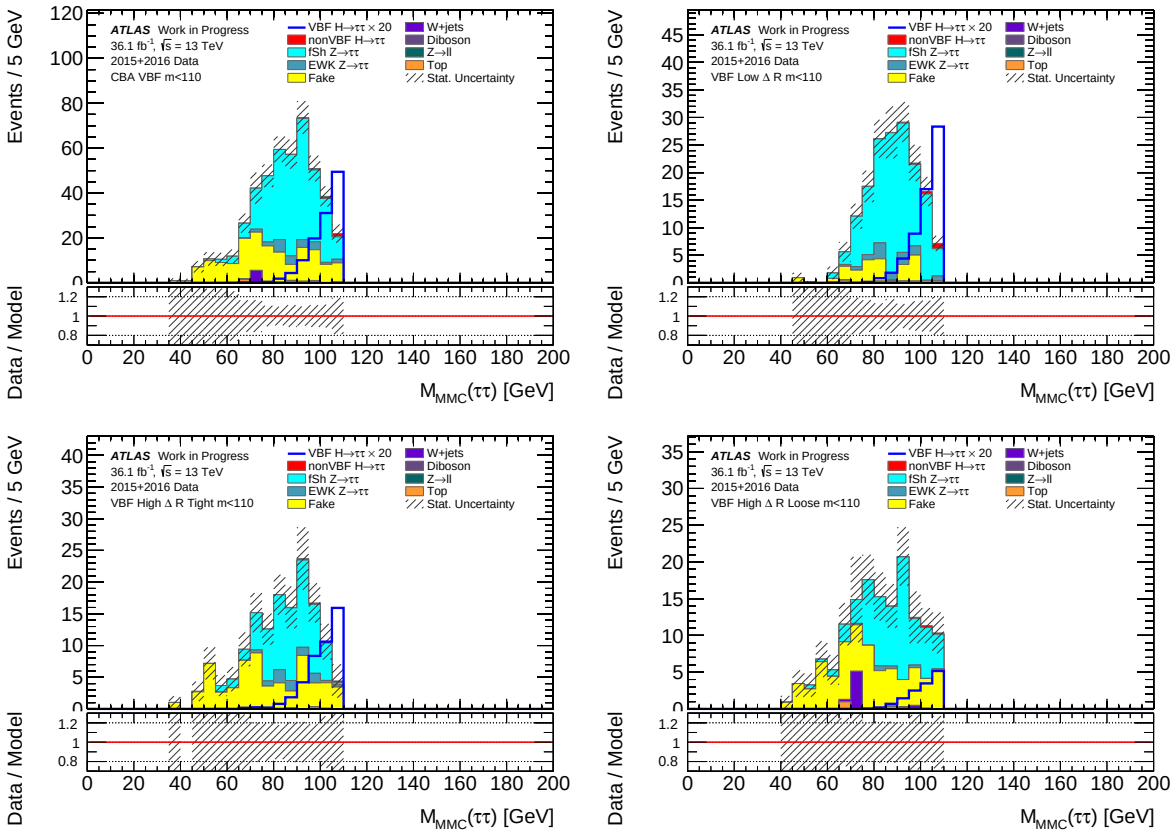

Figure 9.2.: Histograms of $m_{\tau\tau}^{\mathrm{MMC}}$ in the CRs.

ing to produced neutrinos ν in the event, must be considered. This uncertainty is estimated by comparing recorded data from 2015 and 2016 to MC data [118].

- Pile-up and parton shower: Pile-up, described in Section 2.7.3, leads to background in the analysis and must be considered in simulations. Therefore, a pile-up reweighting is performed. The best agreement regarding the number of interactions per bunch crossing of data and MC data is obtained using a correction factor of $1/(1.16^{+0.07}_{-0.16}-1)$. The uncertainties arising from pile-up and parton shower are estimated by a comparison of different MC generators.

- Luminosity: The uncertainty of the integrated luminosity is 2.1 % for data recorded in 2015 and 2016 [119], derived from a calibration of the luminosity scale based on beam-separation scans [120]. Uncertainties of the luminosity calibration arise e.g. from uncertainties of the beam dynamics and instrumental effects.

Important theoretical systematic uncertainties arise from higher order QCD corrections, PDFs, generator modelling, simulation of the underlying event (UE) and parton showers as well as the Higgs boson branching ratio to τ leptons [100].

All considered and neglected systematic uncertainties are listed in Appendix D. The NPs are included in the fit as additional histograms, which correspond to the nominal histogram but on the one hand one standard deviation σ shifted upwards and on the other hand one σ shifted downwards. In general, the NPs can influence the signal and background event yields (normalisation uncertainties) as well as the shape (shape uncertainties) of the distributions in the fit.

9.4. Fit Results

Within the SM, in absence of CP violation at the HVV vertex, the expected minimum of the ΔNLL curve is at $\tilde{d} = 0$ since by construction the ΔNLL curve has its minimum at $\tilde{d} = 0$ where signal and background fit best the Asimov data. Depending on how the shape of the $\mathcal{O}_1$ distribution changes with increasing values of $|\tilde{d}|$, the calculated values of ΔNLL increase, leading to an approximate parabola centred at $\tilde{d} = 0$ for small values of $|\tilde{d}|$. The ΔNLL curve flattens out for $\tilde{d}$-values of $|\tilde{d}| > 0.2$. This is expected since the method of using $\mathcal{O}_1$ as discriminating variable is more sensitive for small values of $\tilde{d}$, as discussed in Section 2.5.4. Another reason is that wider bins are used in the pre-fit histograms of $\mathcal{O}_1$ for $|\mathcal{O}_1| > 5$, leading to a reduced sensitivity for larger values of $|\tilde{d}|$.

In order to determine the 68% CL from reading of the points intersecting with the ΔNLL curve at 0.5, a linear interpolation between the discrete values of $\tilde{d}$, at which a fit is performed, is done. Although the VBF subregions in the mass window $[110, 140]$ GeV are relatively low in statistics, the fits using the VBF subregions determine expected 68% CIs, see Figure 9.3, given by:

- $\tilde{d} \in [-0.11, 0.12]$ at 68% CL for statistical uncertainties only
- $\tilde{d} \notin ([-0.43, -0.17] \cup [0.19, 0.21])$ at 68% CL for statistical and systematic uncertainties

The fits in the VBF inclusive region cannot be used to set a 68% CI with respect to $\tilde{d}$ since the ΔNLL curve flattens out before an intersection with the line at 0.5 happens, see Figure 9.4. The reason for this is a relatively low signal to background ratio in the central bins of the $\mathcal{O}_1$ distribution in the VBF inclusive region, mainly caused by many fake and $Z^0 \to \tau_{\text{had}}\tau_{\text{had}}$ background events. Therefore, only the tails of the $\mathcal{O}_1$ distribution with low statistics are sensitive to BSM VBF signals, reducing the overall sensitivity of the fit in the VBF inclusive region. The consideration of systematic uncertainties in addition to statistical uncertainties leads to larger expected CIs, which is caused by a Gaussian smearing of the bin content of the input histograms implement by NPs in the likelihood

function, giving signal and background more freedom to fit the Asimov data. The fit using the VBF subregions is more sensitive than the fit in the VBF inclusive region. The splitting of the VBF inclusive region results in a VBF high p_T region with a small number of fake background events. Therefore, the high p_T region has a relatively high signal to background ratio also in the central bins of the $\mathcal{O}_1$ distribution and the fit using the VBF subregions is more sensitive regarding anomalous CP couplings at the HVV vertex than using the VBF inclusive region. The determined CIs are summarised in Table 9.2.

For the Asimov fit using the SM VBF signal, the best-fit value of μ for the Asimov data, which are based on the SM hypothesis for $\tilde{d} = 0$, is expected to be one at $\tilde{d} = 0$. The best-fit values of the signal strength μ for the SM hypothesis, are summarised in Table 9.3. The values of the best-fit signal strength μ for the SM prediction are consistent with the expectation of $\mu = 1$ for the Asimov data. The total uncertainty of μ increases when considering systematic uncertainties in addition to statistical uncertainties in the fit.

The post-fit yields of the considered NPs can be found in Appendix D.

region	CI stats only	CI stats+sys
VBF subchannels	$\tilde{d} \in [-0.11, 0.12]$	$\tilde{d} \notin ([-0.43, -0.17] \cup [0.19, 0.21])$
VBF inclusive	$\tilde{d} \in [-\infty, \infty]$	$\tilde{d} \in [-\infty, \infty]$

Table 9.2.: Summary of the determined 68% CIs using the ΔNLL against $\tilde{d}$ curve obtained from using the VBF subchannels and the VBF inclusive region for statistical uncertainties only and for statistical plus systematic uncertainties (stats+sys), respectively.

region	μ stats only	μ stats+sys
VBF subchannels	$1.00^{+0.58}_{-0.57}$	$1.00^{+0.76}_{-0.76}$
VBF inclusive	$1.00^{+0.69}_{-0.68}$	$1.00^{+0.91}_{-0.91}$

Table 9.3.: Summary of the best-fit value of the SM signal strength μ obtained from using the VBF subchannels and the VBF inclusive region for statistical uncertainties (stats) only and for statistical plus systematic uncertainties (stats+sys), respectively.

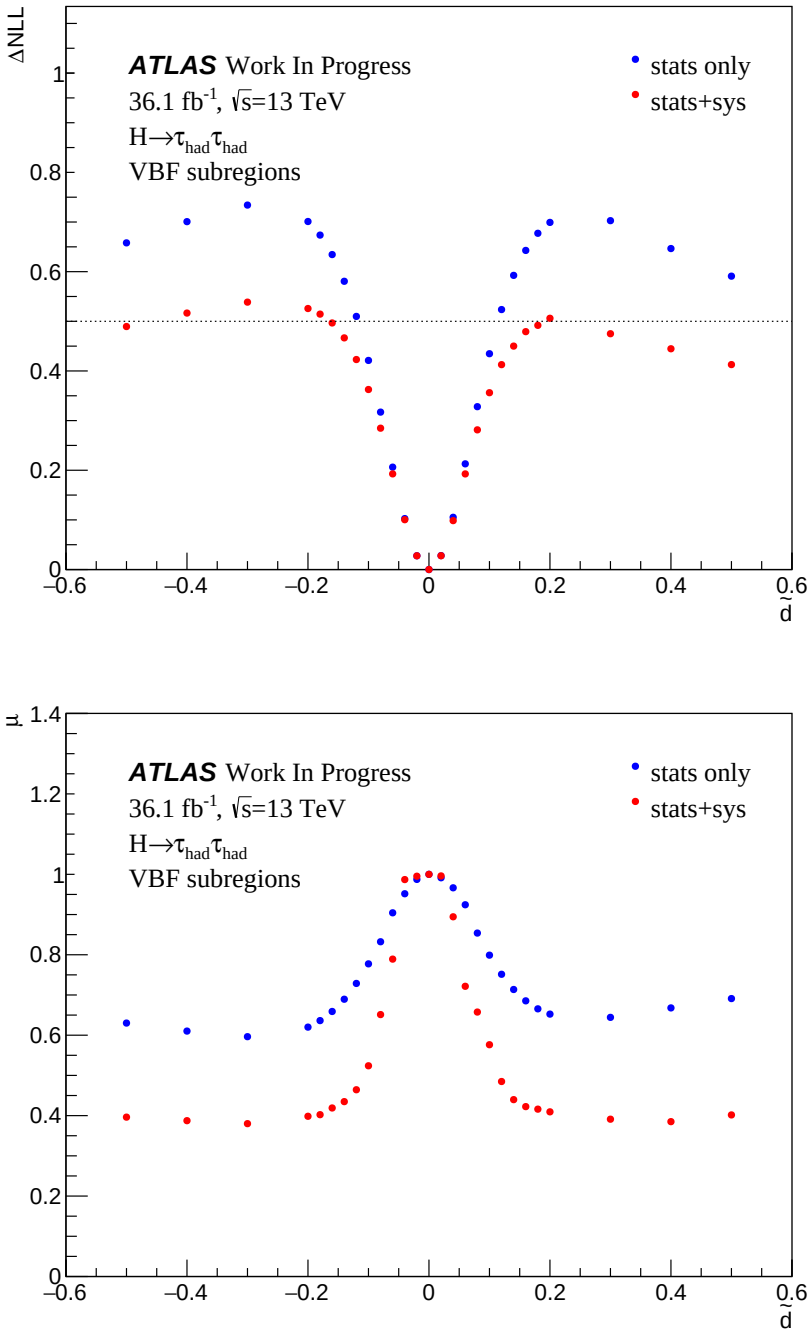

Figure 9.3.: ΔNLL and best-fit signal strength μ as function of $\tilde{d}$ for statistical uncertainty only (blue) and statistical plus systematic uncertainties (red). The corresponding fit is performed in the VBF subchannels using Asimov data.

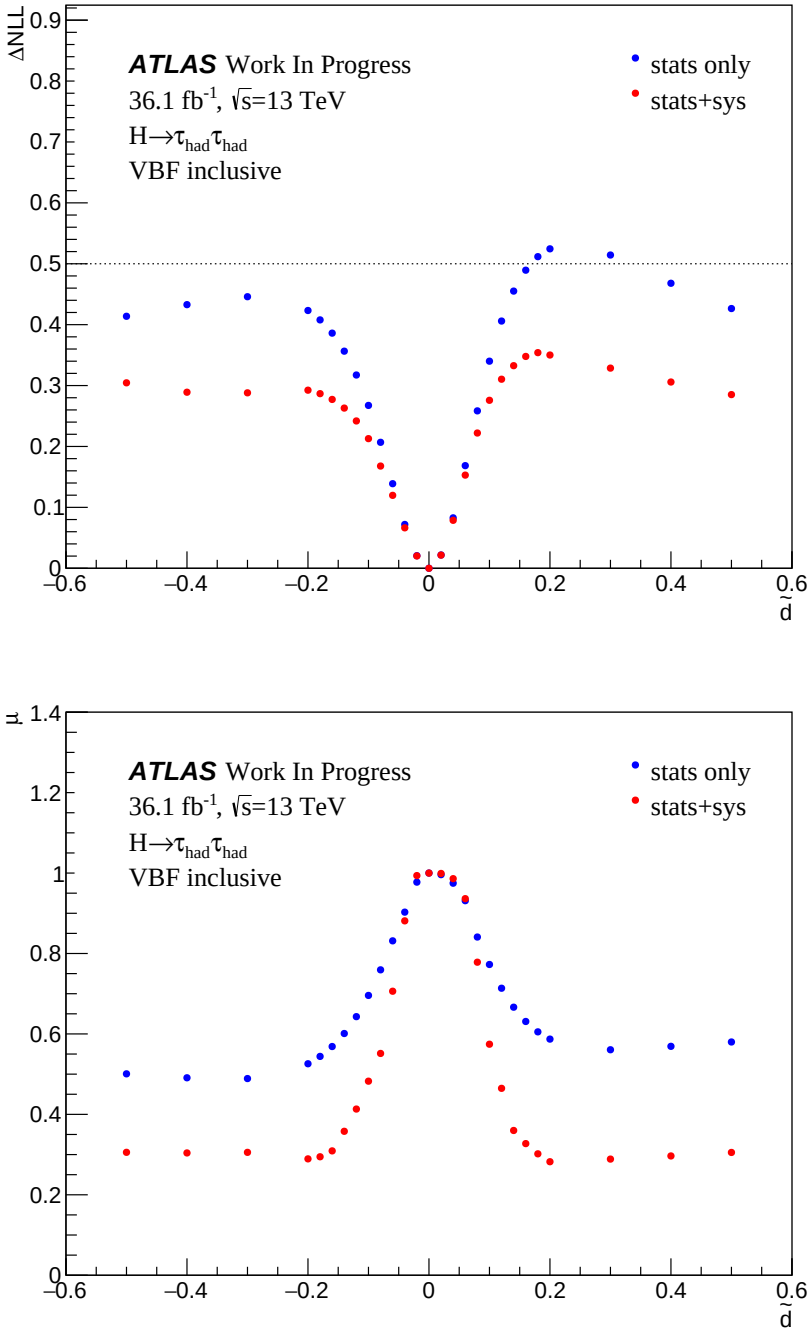

Figure 9.4.: ΔNLL and best-fit signal strength μ as function of $\tilde{d}$ for statistical uncertainty only (blue) and statistical plus systematic uncertainties (red). The corresponding fit is performed in the VBF inclusive region using Asimov data.

10. Conclusions and Outlook

The discovery of the Higgs boson at the LHC in 2012 opened up new opportunities to test the SM and search for BSM physics. The SM predicts a CP-even Higgs boson, while deviations from this would indicate CP violation in the Higgs sector. In this thesis, a method to measure the CP nature of the Higgs boson using the Optimal Observables $\mathcal{O}_{1,2}$ is presented. Assuming $\tilde{d} = \tilde{d}_B$, possible BSM CP scenarios can be parametrised by a single parameter $\tilde{d}$, where $\tilde{d} = 0$ corresponds to the SM prediction. To simulate BSM CP scenarios, a reweighting method is used, i.e. the SM prediction is reweighted corresponding to different values of $\tilde{d}$. The Optimal Observable of first order $\mathcal{O}_1$ is a CP-odd observable, providing information on the CP nature of the Higgs boson, while the Optimal Observable of second order $\mathcal{O}_2$ is CP-even but sensitive to $\tilde{d}^2$.

The measurement of the CP nature at the HVV vertex is performed in the VBF $H \to \tau_{\text{had}}\tau_{\text{had}}$ decay channel and the expected sensitivity with respect to $\tilde{d}$ is determined in terms of a frequentist 68% central confidence interval, containing the true value of $\tilde{d}$ at 68% confidence level. The event selection and categorisation, the object reconstruction and the MC simulations follow closely the SM couplings analysis.

The determination of the expected confidence interval is performed using two methods: gauge curves and a maximum likelihood fit. Gauge curves show the mean value of $\mathcal{O}_{1,2}$ in dependence of the underlying value of $\tilde{d}$. The maximum likelihood fit is performed blinded using an Asimov pseudo-dataset consisting of the sum of the SM VBF Higgs signal and the background. Two fits in two different fit regions are performed, respectively. One fit is done in the VBF inclusive region, while the other fit is performed in the VBF subregions. Each fit is performed considering statistical uncertainties only and considering both statistical and systematic uncertainties.

Due to large statistical fluctuations in the background of the $\mathcal{O}_1$ distribution and small sensitivity of $\mathcal{O}_2$ for small values of $|\tilde{d}|$, gauge curves for signal and background for both $\mathcal{O}_1$ and $\mathcal{O}_2$ are biased and cannot be used for the determination of a confidence interval for $\tilde{d}$. Gauge curves using $\mathcal{O}_1$, which only consider signal processes and statistical uncertainties only, determine the expected sensitivity to

- $\tilde{d} \in [-0.035, 0.047]$ at 68% CL in the VBF inclusive region

- $\tilde{d} \notin ([-\infty, -0.05] \cup [0.05, 0.87])$ at 68% CL in the VBF inclusive region in the mass window $[110, 140]$ GeV
- $\tilde{d} \notin ([-0.92, -0.06] \cup [0.06, 0.73])$ in the VBF high p_T^{Higgs} region
- $\tilde{d} \notin ([-0.68, -0.06] \cup [0.07, 0.058])$ at 68% CL in the VBF high p_T^{Higgs} region in the mass window $[110, 140]$ GeV

The likelihood fit in the VBF subregions (VBF high p_T^{Higgs}, VBF low p_T^{Higgs} tight, VBF low p_T^{Higgs} loose) determines the expected 68% confidence interval with respect to $\tilde{d}$ to

- $\tilde{d} \in [-0.11, 0.12]$ at 68% CL for statistical uncertainties only
- $\tilde{d} \notin ([-0.43, -0.17] \cup [0.19, 0.21])$ at 68% CL for statistical and systematic uncertainties

The likelihood fit in the VBF inclusive region cannot be used to set a 68% confidence interval for $\tilde{d}$.

To improve the measurement using gauge curves, a symmetrisation of the asymmetric background distribution, potentially caused by statistical fluctuation in the MC simulation sample, could be performed. Also an improved modelling of the W+jets background, in particular in the VBF high p_T^{Higgs} region, could potentially increase the expected sensitivity with respect to $\tilde{d}$. Further studies can be done to improve the NLL fit. The binning of the $\mathcal{O}_1$ distribution in the SRs and the binning of $m_{\tau\tau}^{\text{MMC}}$ in the CRs can be optimised. The influence of different fit regions with respect to the sensitivity regarding $\tilde{d}$ could be investigated. A fit using the VBF high p_T^{Higgs} region and an inclusive low p_T^{Higgs} region could be performed. In addition to the fit of $\mathcal{O}_1$, also a fit of $\mathcal{O}_2$ can be performed. Although $\mathcal{O}_2$ does not provide a direct CP-test, it is more sensitive to larger $\tilde{d}$-values than $\mathcal{O}_1$. Also a two-dimensional fit of $\mathcal{O}_1$ against $\mathcal{O}_2$ is an interesting task for the future. In this thesis, a cut-based CP-analysis is performed. Depending on ongoing studies in the SM coupling analysis, a switch to a multivariate analysis can possibly improve the sensitivity with respect to $\tilde{d}$. Finally, the data can be unblinded and the combined fit of the entire $H \to \tau\tau$ channel can be performed using real data instead of the Asimov dataset. In the future, new data collected at the LHC will lead to more statistical precision for this analysis and will lead to a more precise measurement of the CP nature of the Higgs boson.

A. Additional Event Yield Tables

A.1. Cut-Flows with Mass Cuts

The Tables A.1-A.4 present additional cut-flows of the VBF inclusive region and the VBF subregions (high p_T^{Higgs}, low p_T^{Higgs} tight and low p_T^{Higgs} loose) with different mass cuts.

A.2. Cut-Flow of VBF regions with Weight Cut

Table A.5 shows the yields in the different VBF categories after applying a weight cut $w(\tilde{d}) < 100$. Only the VBF Higgs boson signal is affected by a cut on the weight factor since only the VBF signal is reweighted to simulate BSM CP scenarios at the HVV vertex.

Cut	VBF	ggF+ttH+VH	Data	Total Bkg
VBF $w < 100$	23.2±0.2	12.9±0.7	648±26	676±23
VBF LowΔR $w < 100$	11.2±0.2	6.4±0.6	194±14	189±10
VBF HighΔR Tight $w < 100$	9.2±0.2	3.3±0.4	241±16	249±15
VBF HighΔR Loose $w < 100$	2.8±0.1	3.2±0.4	213±15	238±14
VBF $[110, 140]$ GeV $w < 100$	15.7±0.2	8.0±0.6	88.0±9.4	75.6±8.1
VBF LowΔR $[110, 140]$ GeV $w < 100$	8.0±0.1	4.3±0.5	17.0±4.1	15.0±3.1
VBF HighΔR Tight $[110, 140]$ GeV $w < 100$	5.9±0.1	1.8±0.3	43.0±6.6	37.2±6.2
VBF HighΔR Loose $[110, 140]$ GeV $w < 100$	1.8±0.1	1.9±0.3	28.0±5.3	23.4±4.2

Table A.5.: Cut-Flow for the Higgs boson production processes, data and total background with and without a mass cut $110 < m_{\text{MMC}} < 140$ GeV and with a weight cut $w(\tilde{d}) < 100$ applied. Only the VBF Higgs boson signal is affected by a cut on the weight factor.

Cut	Fake	W+jets	Top	$Z^0 \to \tau\tau$	EWK $Z^0 \to \tau\tau$	VV+Z^0 $\ell\ell$	VBF	ggF	ttH+VH	Data	Total Bkg
VBF	281±17	18.9±6.8	10.4±2.0	337±14	25.7±2. 4	3.3±0.4	24.7±0.3	12.1±0.7	0.8±0.6	648±26	677±23
VBF [100,150] GeV	77.3±8.4	7.0±3.4	2.6±0.9	75.7±7.2	4.8±1. 0	0.7±0.2	22.4±0.2	10.4±0.7	0.8±0.6	186±14	168±12
VBF [105,140] GeV	49.8±6.9	5.7±3.2	2.6±0.9	42.4±5.5	3.9±0. 9	0.5±0.1	19.7±0.2	8.8±0.6	0.8±0.6	124±11	104.8±9.4
VBF [105,145] GeV	58.7±7.4	5.7±3.2	2.6±0.9	43.0±5.5	3.9±0. 9	0.5±0.1	20.3±0.2	9.1±0.6	0.8±0.6	129±11	114.3±9.9
VBF [105,150] GeV	60.9±7.5	7.0±3.4	2.6±0.9	42.2±5.8	3.9±0. 9	0.5±0.1	20.7±0.2	9.2±0.6	0.8±0.6	137±12	117±10
VBF [105,155] GeV	64.1±7.7	7.0±3.4	2.6±0.9	43.1±6.0	3.9±0. 9	0.5±0.1	20.9±0.2	9.3±0.6	0.8±0.6	140±12	121±10
VBF [110,135] GeV	35.1±5.8	4.6±3.0	2.0±0.8	23.1±4.0	2.0±0. 7	0.3±0.1	15.7±0.2	6.8±0.6	0.5±0.5	80.0±8.9	67.2±7.7
VBF [110,140] GeV	39.0±6.0	5.7±3.2	2.3±0.8	26.1±4.3	2.2±0. 7	0.3±0.1	17.0±0.2	7.4±0.6	0.6±0.5	88.0±9.4	75.6±8.1
VBF [110,145] GeV	47.9±6.6	5.7±3.2	2.3±0.8	26.7±4.4	2.2±0. 7	0.4±0.1	17.6±0.2	7.7±0.6	0.6±0.5	93.0±9.6	85.1±8.6
VBF [110,150] GeV	50.1±6.8	7.0±3.4	2.3±0.8	25.8±4.7	2.2±0. 7	0.4±0.1	18.0±0.2	7.8±0.6	0.6±0.5	101±10	87.8±9.0
VBF [115,135] GeV	21.1±4.6	4.2±3.0	1.5±0.7	11.4±3.1	1.4±0. 5	0.1±0.1	12.3±0.2	4.9±0.4	0.5±0.5	49.0±7.0	39.7±6.4
VBF [120,130] GeV	11.9±3.6	4.2±3.0	0.6±0.4	5.0±2.3	1.0±0. 5	0.1±0.1	6.6±0.1	2.5±0.3	0.5±0.5 GeV	22.0±4.7	22.9±5.3

Table A.1.: Cut-Flow of the CB VBF inclusive region with $m_{\tau\tau}^{\mathrm{MMC}}$ [GeV] cuts.

Cut	Fake	W+jets	Top	$Z^0 \to \tau\tau$	EWK $Z^0 \to \tau\tau$	VV+$Z^0\ell\ell$	VBF	ggF	ttH+VH	Data	Total Bkg
VBF Low Δ R	24.8±6.8	3.7±2.4	2.2±1.0	142.8±6.8	14.1±1.8	1.7±0.3	12.5±0.2	5.6±0.5	0.8±0.6	194±14	189±10
VBF Low Δ R [100,150] GeV	0.9±1.7	3.2±2.4	0.8±0.5	30.2±3.2	3.1±0.8	0.1±0.1	11.7±0.2	5.1±0.5	0.8±0.6	48.0±6.9	38.3±4.4
VBF Low Δ R [105,140] GeV	0.1±1.0	3.2±2.4	0.8±0.5	14.4±2.0	2.6±0.7	0.1±0.1	10.5±0.2	4.5±0.4	0.8±0.6	26.0±5.1	21.3±3.4
VBF Low Δ R [105,145] GeV	0.1±1.0	3.2±2.4	0.8±0.5	14.4±2.1	2.6±0.7	0.1±0.1	10.7±0.2	4.6±0.4	0.8±0.6	28.0±5.3	21.2±3.4
VBF Low Δ R [105,150] GeV	0.1±1.0	3.2±2.4	0.8±0.5	14.5±2.1	2.6±0.7	0.1±0.1	10.9±0.2	4.6±0.4	0.8±0.6	28.0±5.3	21.3±3.4
VBF Low Δ R [105,155] GeV	0.1±1.0	3.2±2.4	0.8±0.5	14.8±2.1	2.6±0.7	0.1±0.1	10.9±0.2	4.6±0.4	0.8±0.6	28.0±5.3	21.6±3.4
VBF Low Δ R GeV [110,135]	0.4±1.0	2.2±2.2	0.3±0.3	9.2±1.6	1.5±0.6	0.0±0.1	8.5±0.1	3.5±0.4	0.5±0.5	16.0±4.0	13.5±2.9
VBF Low Δ R GeV [110,140]	0.4±1.0	3.2±2.4	0.5±0.4	9.4±1.6	1.5±0.6	0.0±0.1	9.1±0.2	3.8±0.4	0.5±0.5	17.0±4.1	15.0±3.1
VBF Low Δ R GeV [110,145]	0.4±1.0	3.2±2.4	0.5±0.4	9.3±1.7	1.5±0.6	0.0±0.1	9.3±0.2	3.8±0.4	0.5±0.5	19.0±4.4	14.9±3.1
VBF Low Δ R GeV [110,150]	0.4±1.0	3.2±2.4	0.5±0.4	9.4±1.7	1.5±0.6	0.0±0.1	9.5±0.2	3.9±0.4	0.5±0.5	19.0±4.4	15.0±3.2
VBF Low Δ R GeV [115,135]	-0.5±0.3	2.2±2.2	0.0±0.0	3.6±1.1	1.0±0.5	-0.0±0.0	6.7±0.1	2.4±0.3	0.5±0.5	10.0±3.2	6.3±2.5
VBF Low Δ R GeV [120,130]	-0.1±0.2	2.2±2.2	0.0±0.0	1.4±0.6	0.9±0.4	0.0±0.0	3.6±0.1	1.2±0.2	0.5±0.5	5.0±2.2	4.3±2.3

Table A.2.: Cut-Flow of the CB VBF high p_T^{Higgs} regions with $m_{\tau\tau}^{\mathrm{MMC}}$ [GeV] cuts.

Cut	Fake	W+jets	Top	$Z^0 \to \tau\tau$	EWK $Z^0 \to \tau\tau$	VV+$Z^0\ell\ell$	VBF	ggF	ttH+VH	Data	Total Bkg
VBF High Δ R Tight	129±11	5.9±3.0	3.8±1.1	99.9±9.0	9.7±1.5	0.8±0.2	9.3±0.2	3.3±0.4	0.0±0.0	241±16	249±15
VBF High Δ R Tight [100,150] GeV	42.2±6.3	3.4±2.4	0.6±0.4	22.2±5.4	1.3±0.5	0.3±0.1	8.2±0.1	2.6±0.4	0.0±0.0	79.0±8 .9	69.9±8.6
VBF High Δ R Tight [105,140] GeV	29.1±5.4	2.1±2.1	0.6±0.4	14.1±4.1	0.9±0.4	0.2±0.1	7.0±0.1	2.2±0.4	0.0±0.0	59.0±7 .7	47.0±7.1
VBF High Δ R Tight [105,145] GeV	34.2±5.8	2.1±2.1	0.6±0.4	13.8±4.1	0.9±0.4	0.2±0.1	7.3±0.1	2.3±0.4	0.0±0.0	60.0±7 .7	51.9±7.4
VBF High Δ R Tight [105,150] GeV	34.9±5.8	3.4±2.4	0.6±0.4	13.0±4.4	0.9±0.4	0.2±0.1	7.5±0.1	2.4±0.4	0.0±0.0	64.0±8 .0	53.1±7.7
VBF High Δ R Tight [105,155] GeV	37.4±6.0	3.4±2.4	0.6±0.4	13.7±4.4	0.9±0.4	0.2±0.1	7.6±0.1	2.4±0.4	0.0±0.0	66.0±8 .1	56.2±7.9
VBF High Δ R Tight [110,135] GeV	19.3±4.4	2.1±2.1	0.6±0.4	8.8±3.3	0.4±0.3	0.2±0.1	5.5±0.1	1.5±0.3	0.0±0.0	36.0±6 .0	31.4±5.8
VBF High Δ R Tight [110,140] GeV	23.2±4.7	2.1±2.1	0.6±0.4	10.6±3.5	0.6±0.3	0.2±0.1	6.0±0.1	1.8±0.3	0.0±0.0	43.0±6 .6	37.2±6.2
VBF High Δ R Tight [110,145] GeV	28.4±5.1	2.1±2.1	0.6±0.4	10.3±3.6	0.6±0.3	0.2±0.1	6.4±0.1	1.9±0.4	0.0±0.0	44.0±6 .6	42.1±6.6
VBF High Δ R Tight [110,150] GeV	29.1±5.2	3.4±2.4	0.6±0.4	9.5±3.9	0.6±0.3	0.2±0.1	6.5±0.1	2.0±0.4	0.0±0.0	48.0±6 .9	43.3±7.0
VBF High Δ R Tight [115,135] GeV	9.8±3.4	2.1±2.1	0.6±0.4	4.7±2.6	0.2±0.2	0.1±0.1	4.4±0.1	0.9±0.2	0.0±0.0	26.0±5 .1	17.5±4.8
VBF High Δ R Tight [120,130] GeV	5.0±2.7	2.1±2.1	0.3±0.3	0.7±2.0	0.0±0.0	0.1±0.1	2.3±0.1	0.5±0.1	0.0±0.0	13.0±3 .6	8.1±3.9

Table A.3.: Cut-Flow table of the CB VBF low p_T^{Higgs} tight region with $m_{\tau\tau}^{\text{MMC}}$ [GeV] cuts.

Cut	Fake	W+jets	Top	$Z^0 \to \tau\tau$	EWK $Z^0 \to \tau\tau$	VV+$Z^0\ell\ell$	VBF	ggF	ttH+VH	Data	Total Bkg
VBF High Δ R Loose	128±11	9.3±5.6	4.5±1.4	94.4±7.8	1.9±0.6	0.9±0.2	2.8±0.1	3.2±0.4	0.0±0.0	213±15	239±15
VBF High Δ R Loose [110,150] GeV	34.2±5.4	0.4±0.4	1.1±0.6	23.3±3.6	0.4±0.3	0.3±0.1	2.5±0.1	2.7±0.3	0.0±0.0	59.0±7 .7	59.6±6.5
VBF High Δ R Loose [105,140] GeV	20.6±4.2	0.4±0.4	1.1±0.6	13.9±3.0	0.4±0.3	0.1±0.1	2.2±0.1	2.1±0.3	0.0±0.0	39.0±6 .2	36.5±5.3
VBF High Δ R Loose [105,145] GeV	24.4±4.6	0.4±0.4	1.1±0.6	14.8±3.1	0.4±0.3	0.2±0.1	2.2±0.1	2.2±0.3	0.0±0.0	41.0±6 .4	41.2±5.6
VBF High Δ R Loose [105,150] GeV	25.8±4.7	0.4±0.4	1.1±0.6	14.7±3.1	0.4±0.3	0.2±0.1	2.3±0.1	2.2±0.3	0.0±0.0	45.0±6 .7	42.5±5.7
VBF High Δ R Loose [105,155] GeV	26.6±4.8	0.4±0.4	1.1±0.6	14.6±3.4	0.4±0.3	0.2±0.1	2.3±0.1	2.3±0.3	0.0±0.0	46.0±6 .8	43.3±5.9
VBF High Δ R Loose [110,135] GeV	15.4±3.7	0.4±0.4	1.1±0.6	5.2±1.8	0.2±0.2	0.1±0.1	1.7±0.1	1.8±0.3	0.0±0.0	28.0±5 .3	22.4±4.2
VBF High Δ R Loose [110,140] GeV	15.4±3.7	0.4±0.4	1.1±0.6	6.1±1.8	0.2±0.2	0.1±0.1	1.8±0.1	1.9±0.3	0.0±0.0	28.0±5.3	23.4±4.2
VBF High Δ R Loose [110,145] GeV	19.2±4.1	0.4±0.4	1.1±0.6	7.1±1.9	0.2±0.2	0.1±0.1	1.9±0.1	1.9±0.3	0.0±0.0	30.0±5 .5	28.1±4.6
VBF High Δ R Loose [110,150] GeV	20.6±4.2	0.4±0.4	1.1±0.6	6.9±2.0	0.2±0.2	0.1±0.1	2.0±0.1	2.0±0.3	0.0±0.0	34.0±5 .8	29.4±4.7
VBF High Δ R Loose [115,135] GeV	11.7±3.2	0.0±0.0	0.8±0.5	3.2±1.3	0.2±0.2	0.0±0.0	1.3±0.1	1.5±0.3	-0.0±0.0	13.0±3 .6	16.0±3.5
VBF High Δ R Loose [120,130] GeV	7.1±2.4	0.0±0.0	0.3±0.3	2.8±1.0	0.2±0.2	0.0±0.0	0.7±0.0	0.8±0.2	0.0±0.0	4.0±2.0	10.4±2.7

Table A.4.: Cut-Flow of the CB VBF low p_T^{Higgs} loose region with $m_{\tau\tau}^{\text{MMC}}$ [GeV] cuts.

B. Optimisation of the Mass Cut

This chapter presents the full tables of the mass window optimisation regarding the Asimov significance Z_{asim} for the VBF inclusive region, the VBF high p_T^{Higgs} region, the VBF low p_T^{Higgs} tight region and the VBF low p_T^{Higgs} loose region as discussed in Section 5.5. The tables show in each case the number of signal S and background events B with statistical error, δS and δB, respectively, extracted from the corresponding cut-flow table, see Appendix A.2, of the considered VBF region and the calculated Asimov significances Z_{asim} with total statistical error δZ_{asim}. The total statistical uncertainty of the Asimov significance δZ_{asim} is calculated by

$$\delta Z_{asim} = \sqrt{(Z_{asim}^{\delta S})^2 + (Z_{asim}^{\delta B})^2}, \tag{B.1}$$

where $Z_{asim}^{(\delta S,\delta B)}$ is the statistical uncertainty of the Asimov significance calculated using the uncertainty of the number of signal events δS and background events δB only. Systematic uncertainties are not considered in the optimisation of the mass window. The Asimov signficance is used to determine the significance instead of $\frac{S}{\sqrt{B}}$ since the Asimov significance produce more precise results by incorporating statistical uncertainties if the number of signal and background events are of same order [103]. In the limit $S \ll B$, the Asimov significance Z_{asim} reduces to $\frac{S}{\sqrt{B}}$.

mass window [GeV]	S	δS	B	δB	Z_{asim}	$\delta Z^{\delta S}_{asim}$	$\delta Z^{\delta B}_{asim}$	δZ_{asim}
$[0, 200]$	24.7	0.3	677	23	0.94	$^{+0.01}_{-0.01}$	$^{+0.02}_{-0.02}$	$^{+0.02}_{-0.02}$
$[100, 150]$	22.4	0.2	168	12	1.69	$^{+0.02}_{-0.02}$	$^{+0.05}_{-0.06}$	$^{+0.06}_{-0.06}$
$[105, 140]$	19.7	0.2	104.8	9.4	1.87	$^{+0.02}_{-0.02}$	$^{+0.07}_{-0.09}$	$^{+0.08}_{-0.09}$
$[105, 145]$	20.3	0.2	114.3	9.9	1.85	$^{+0.02}_{-0.02}$	$^{+0.07}_{-0.08}$	$^{+0.07}_{-0.08}$
$[105, 150]$	20.7	0.2	117	10	1.86	$^{+0.02}_{-0.02}$	$^{+0.07}_{-0.08}$	$^{+0.08}_{-0.08}$
$[105, 155]$	20.9	0.2	121	10	1.85	$^{+0.02}_{-0.02}$	$^{+0.07}_{-0.08}$	$^{+0.07}_{-0.08}$
$[110, 135]$	15.7	0.2	67.2	7.7	1.85	$^{+0.02}_{-0.02}$	$^{+0.09}_{-0.11}$	$^{+0.10}_{-0.11}$
$[110, 140]$	17.0	0.2	75.6	8.1	1.89	$^{+0.02}_{-0.02}$	$^{+0.09}_{-0.10}$	$^{+0.09}_{-0.11}$
$[110, 145]$	17.6	0.2	85.1	8.6	1.85	$^{+0.02}_{-0.02}$	$^{+0.08}_{-0.09}$	$^{+0.08}_{-0.10}$
$[110, 150]$	18.0	0.2	87.7	9.0	1.86	$^{+0.02}_{-0.02}$	$^{+0.08}_{-0.10}$	$^{+0.09}_{-0.10}$
$[115, 135]$	12.3	0.2	39.7	6.4	1.86	$^{+0.03}_{-0.03}$	$^{+0.12}_{-0.16}$	$^{+0.13}_{-0.16}$
$[120, 130]$	6.6	0.1	22.9	5.3	1.32	$^{+0.02}_{-0.02}$	$^{+0.12}_{-0.17}$	$^{+0.12}_{-0.17}$

Table B.1.: Asimov significances Z_{asim} with statistical error δZ_{asim} in VBF inclusive region with different mass cuts.

mass window [GeV]	S	δS	B	δB	Z_{asim}	$\delta Z^{\delta S}_{asim}$	$\delta Z^{\delta B}_{asim}$	δZ_{asim}
$[0, 200]$	12.5	0.2	189	10	0.90	$^{+0.01}_{-0.01}$	$^{+0.02}_{-0.02}$	$^{+0.03}_{-0.03}$
$[100, 150]$	11.7	0.2	38.3	4.4	1.80	$^{+0.03}_{-0.03}$	$^{+0.09}_{-0.10}$	$^{+0.09}_{-0.11}$
$[105, 140]$	10.5	0.2	21.3	3.4	2.12	$^{+0.04}_{-0.04}$	$^{+0.13}_{-0.17}$	$^{+0.14}_{-0.17}$
$[105, 145]$	10.7	0.2	21.2	3.4	2.17	$^{+0.04}_{-0.04}$	$^{+0.14}_{-0.17}$	$^{+0.14}_{-0.17}$
$[105, 150]$	10.9	0.2	21.3	3.4	2.19	$^{+0.04}_{-0.04}$	$^{+0.14}_{-0.17}$	$^{+0.14}_{-0.18}$
$[105, 155]$	10.9	0.2	21.6	3.4	2.18	$^{+0.04}_{-0.04}$	$^{+0.14}_{-0.17}$	$^{+0.14}_{-0.17}$
$[110, 135]$	8.5	0.1	13.5	2.9	2.12	$^{+0.02}_{-0.02}$	$^{+0.17}_{-0.23}$	$^{+0.17}_{-0.23}$
$[110, 140]$	9.1	0.2	15.0	3.1	2.16	$^{+0.04}_{-0.04}$	$^{+0.17}_{-0.22}$	$^{+0.17}_{-0.23}$
$[110, 145]$	9.3	0.2	14.9	3.1	2.21	$^{+0.04}_{-0.04}$	$^{+0.17}_{-0.23}$	$^{+0.18}_{-0.23}$
$[110, 150]$	9.5	0.2	15.0	3.2	2.25	$^{+0.04}_{-0.04}$	$^{+0.18}_{-0.24}$	$^{+0.18}_{-0.24}$
$[115, 135]$	6.7	0.1	6.3	2.5	2.33	$^{+0.03}_{-0.03}$	$^{+0.29}_{-0.49}$	$^{+0.30}_{-0.49}$
$[120, 130]$	3.6	0.1	4.3	2.3	1.55	$^{+0.04}_{-0.04}$	$^{+0.26}_{-0.53}$	$^{+0.26}_{-0.53}$

Table B.2.: Asimov significances Z_{asim} with statistical error δZ_{asim} in VBF high p_T^{Higgs} region with different mass cuts.

mass window [GeV]	S	δS	B	δB	Z_{asim}	$\delta Z_{asim}^{\delta S}$	$\delta Z_{asim}^{\delta B}$	δZ_{asim}
$[0, 200]$	9.3	0.2	249	15	0.59	$^{+0.01}_{-0.01}$	$^{+0.02}_{-0.02}$	$^{+0.02}_{-0.02}$
$[100, 150]$	8.2	0.1	69.9	8.6	0.96	$^{+0.01}_{-0.01}$	$^{+0.05}_{-0.06}$	$^{+0.05}_{-0.06}$
$[105, 140]$	7.0	0.1	47.0	7.1	0.99	$^{+0.01}_{-0.01}$	$^{+0.07}_{-0.08}$	$^{+0.07}_{-0.08}$
$[105, 145]$	7.3	0.1	51.9	7.4	0.99	$^{+0.01}_{-0.01}$	$^{+0.06}_{-0.08}$	$^{+0.06}_{-0.08}$
$[105, 150]$	7.5	0.1	53.1	7.7	1.01	$^{+0.01}_{-0.01}$	$^{+0.06}_{-0.08}$	$^{+0.07}_{-0.08}$
$[105, 155]$	7.6	0.1	56.2	7.9	0.99	$^{+0.01}_{-0.01}$	$^{+0.06}_{-0.07}$	$^{+0.06}_{-0.08}$
$[110, 135]$	5.5	0.1	31.4	5.8	0.96	$^{+0.02}_{-0.02}$	$^{+0.07}_{-0.10}$	$^{+0.08}_{-0.10}$
$[110, 140]$	6.0	0.1	37.2	6.2	0.96	$^{+0.02}_{-0.02}$	$^{+0.07}_{-0.09}$	$^{+0.07}_{-0.09}$
$[110, 145]$	6.4	0.1	42.1	6.6	0.96	$^{+0.02}_{-0.02}$	$^{+0.07}_{-0.08}$	$^{+0.07}_{-0.08}$
$[110, 150]$	6.5	0.1	43.3	7.0	0.97	$^{+0.01}_{-0.02}$	$^{+0.07}_{-0.08}$	$^{+0.07}_{-0.07}$
$[115, 135]$	4.4	0.1	17.5	4.8	1.01	$^{+0.02}_{-0.02}$	$^{+0.11}_{-0.16}$	$^{+0.11}_{-0.16}$
$[120, 130]$	2.3	0.1	8.1	3.9	0.77	$^{+0.03}_{-0.03}$	$^{+0.13}_{-0.27}$	$^{+0.13}_{-0.27}$

Table B.3.: Asimov significances Z_{asim} with statistical error δZ_{asim} in VBF low p_T^{Higgs} tight region with different mass cuts.

mass window [GeV]	S	δS	B	δB	Z_{asim}	$\delta Z_{asim}^{\delta S}$	$\delta Z_{asim}^{\delta B}$	δZ_{asim}
$[0, 200]$	2.8	0.1	239	15	0.18	$^{+0.01}_{-0.01}$	$^{+0.01}_{-0.01}$	$^{+0.01}_{-0.01}$
$[100, 150]$	2.5	0.1	59.6	6.5	0.32	$^{+0.01}_{-0.01}$	$^{+0.02}_{-0.02}$	$^{+0.02}_{-0.02}$
$[105, 140]$	2.2	0.1	36.5	5.3	0.36	$^{+0.02}_{-0.02}$	$^{+0.02}_{-0.03}$	$^{+0.03}_{-0.03}$
$[105, 145]$	2.2	0.1	41.2	5.6	0.34	$^{+0.02}_{-0.02}$	$^{+0.02}_{-0.03}$	$^{+0.03}_{-0.03}$
$[105, 150]$	2.2	0.1	42.5	5.7	0.34	$^{+0.02}_{-0.02}$	$^{+0.02}_{-0.03}$	$^{+0.03}_{-0.03}$
$[105, 155]$	2.3	0.1	43.3	5.9	0.35	$^{+0.02}_{-0.02}$	$^{+0.02}_{-0.03}$	$^{+0.03}_{-0.03}$
$[110, 135]$	1.7	0.1	22.4	4.2	0.36	$^{+0.03}_{-0.03}$	$^{+0.03}_{-0.04}$	$^{+0.04}_{-0.05}$
$[110, 140]$	1.8	0.1	23.4	4.2	0.37	$^{+0.02}_{-0.02}$	$^{+0.03}_{-0.04}$	$^{+0.04}_{-0.04}$
$[110, 145]$	1.9	0.1	28.1	4.6	0.35	$^{+0.02}_{-0.02}$	$^{+0.03}_{-0.03}$	$^{+0.03}_{-0.04}$
$[110, 150]$	2.0	0.1	29.4	4.7	0.37	$^{+0.02}_{-0.02}$	$^{+0.02}_{-0.03}$	$^{+0.03}_{-0.04}$
$[115, 135]$	1.3	0.1	16.0	3.5	0.32	$^{+0.02}_{-0.02}$	$^{+0.03}_{-0.04}$	$^{+0.04}_{-0.05}$
$[120, 130]$	0.7	0.0	10.4	2.7	0.22	$^{+0.00}_{-0.00}$	$^{+0.02}_{-0.03}$	$^{+0.02}_{-0.03}$

Table B.4.: Asimov significances Z_{asim} with statistical error δZ_{asim} in VBF low p_T^{Higgs} loose region with different mass cuts.

C. Input Variables of the Optimal Observable Calculation

C.1. Input Variables in the Preselection 2 with Jets Region

In this section, plots of input variables of $\mathcal{O}_{1,2}$ in the preselection with two jets region are presented.

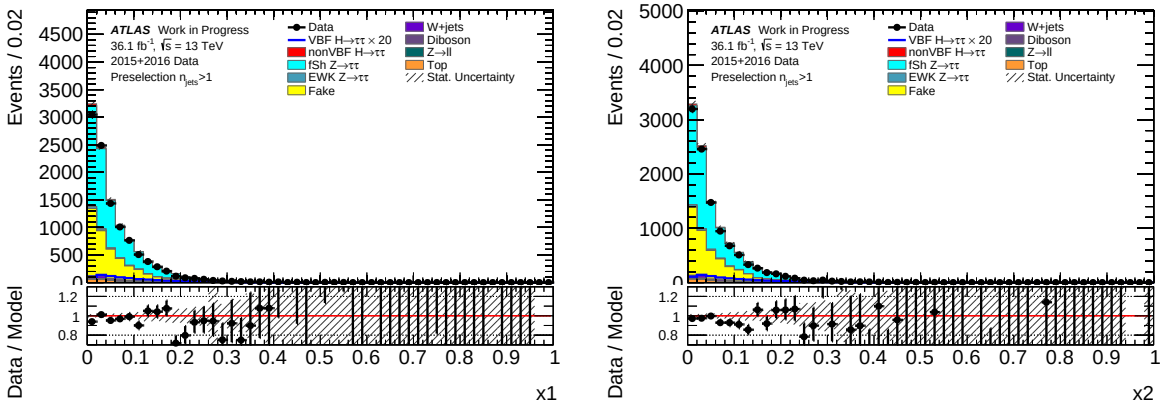

Figure C.1.: Distribution of Bjorken $x_{1,2}$ in the preselection with two jets region.

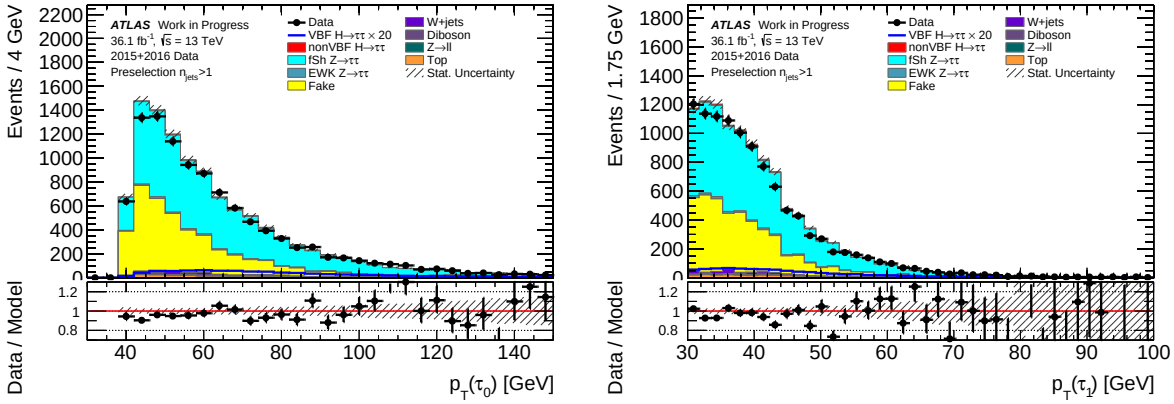

Figure C.2.: Distribution of the transverse momentum p_T of the leading and subleading τ leptons in the preselection with two jets region.

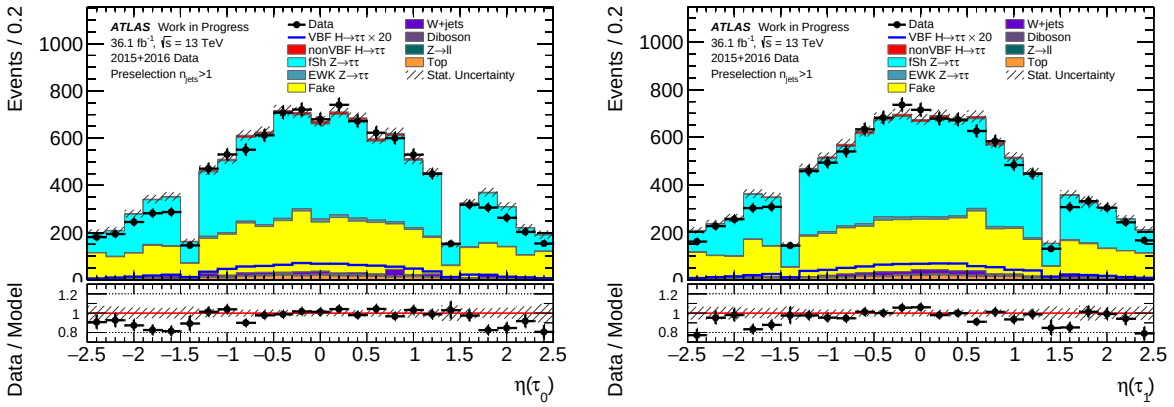

Figure C.3.: Distribution of the pseudorapidity η of the leading and subleading τ leptons in the preselection with two jets region.

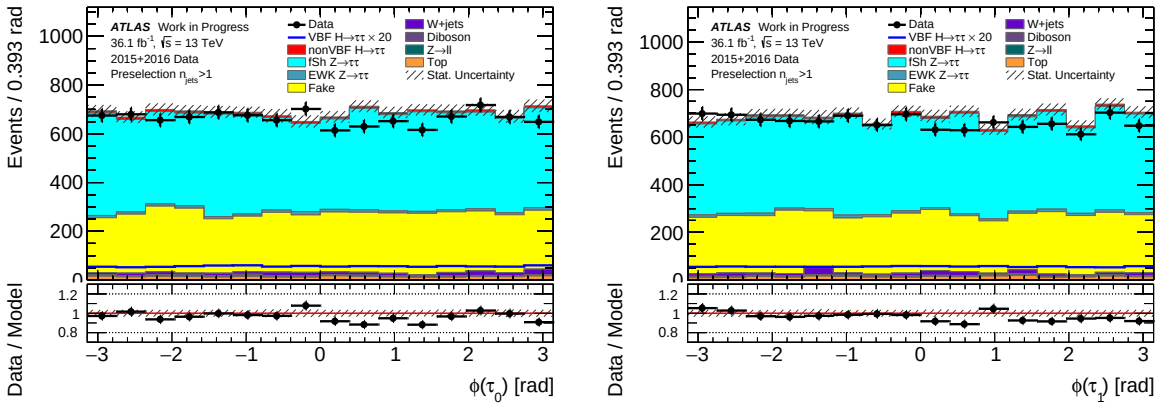

Figure C.4.: Distribution of the azimuthal angle ϕ of the leading and subleading τ leptons in the preselection with two jets region.

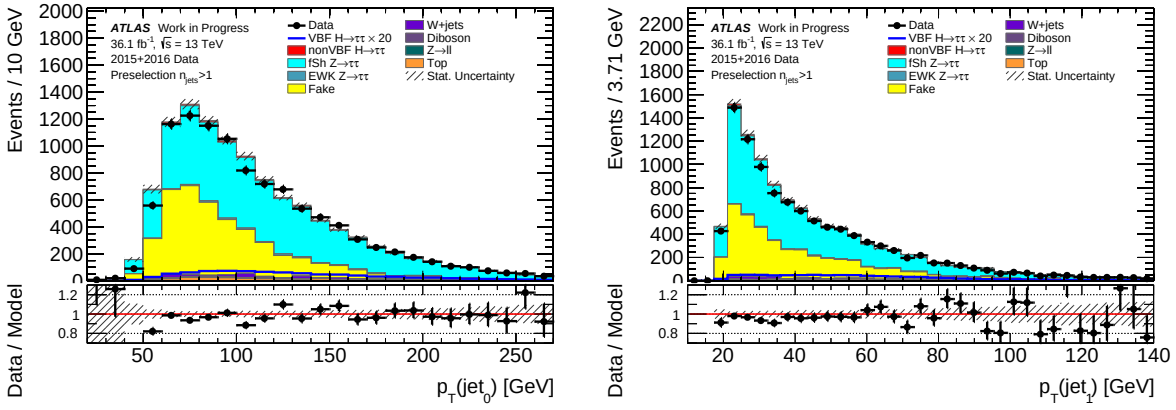

Figure C.5.: Distribution of the transverse momentum p_T of the leading and subleading jets in the preselection with two jets region.

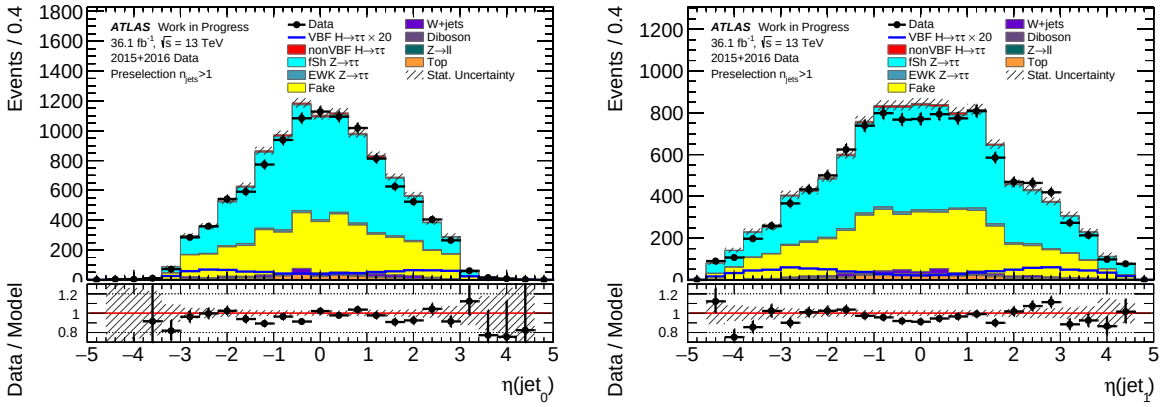

Figure C.6.: Distribution of the pseudorapidity η of the leading and subleading jets in the preselection with two jets region.

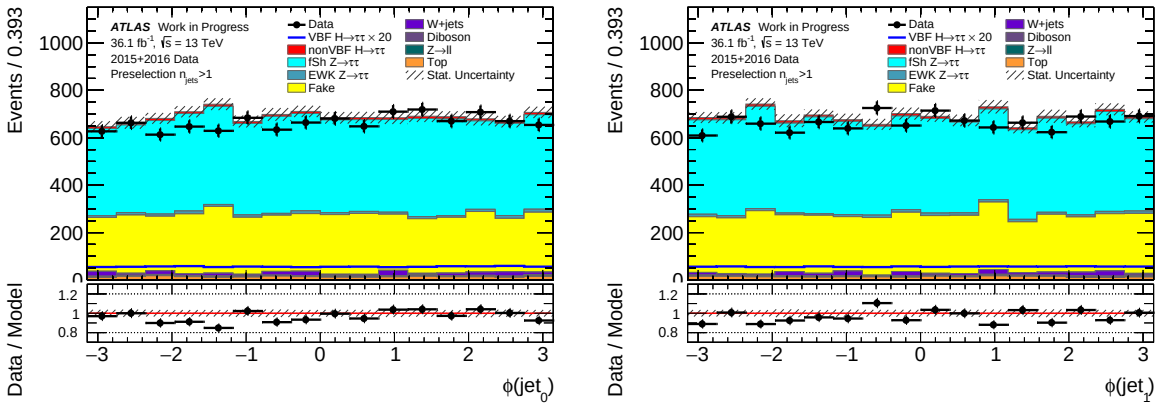

Figure C.7.: Distribution of the azimuthal angle ϕ of the leading and subleading jets in the preselection with two jets region.

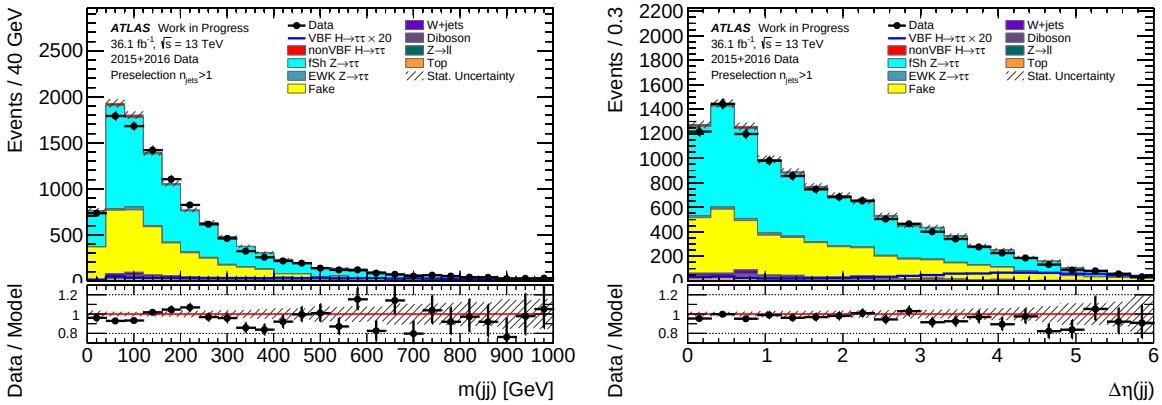

Figure C.8.: Distribution of m_{jet_0,jet_1} and $|\Delta\eta_{jet_0,jet_1}|$ in the VBF preselection with two jets region.

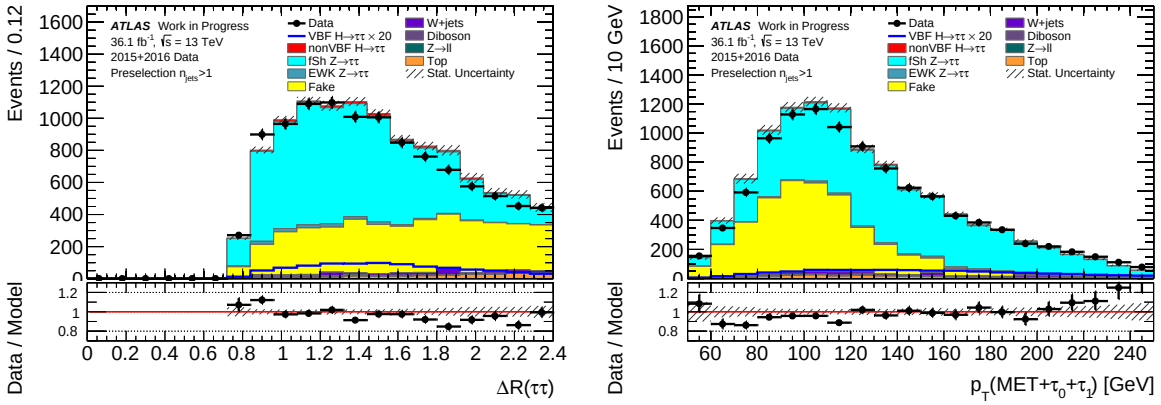

Figure C.9.: Distribution of $\Delta R_{\tau_0,\tau_1}$ and p_T^{Higgs} in the preselection with two jets region.

C.2. Input Variables in the VBF Inclusive Region

In this section, the distributions of important input variables for the calculation of $\mathcal{O}_{1,2}$ in the VBF inclusive region are presented.

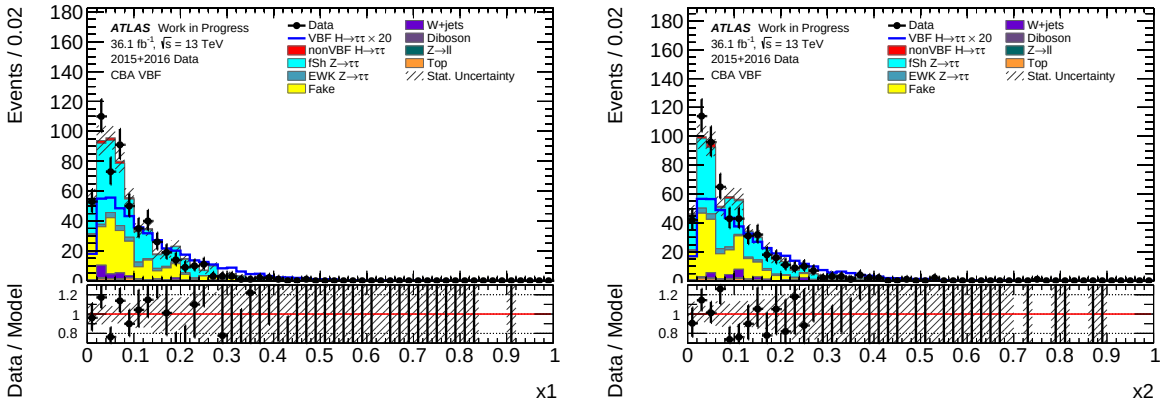

Figure C.10.: Distribution of Bjorken x_1 and Bjorken x_2 in the VBF inclusive region.

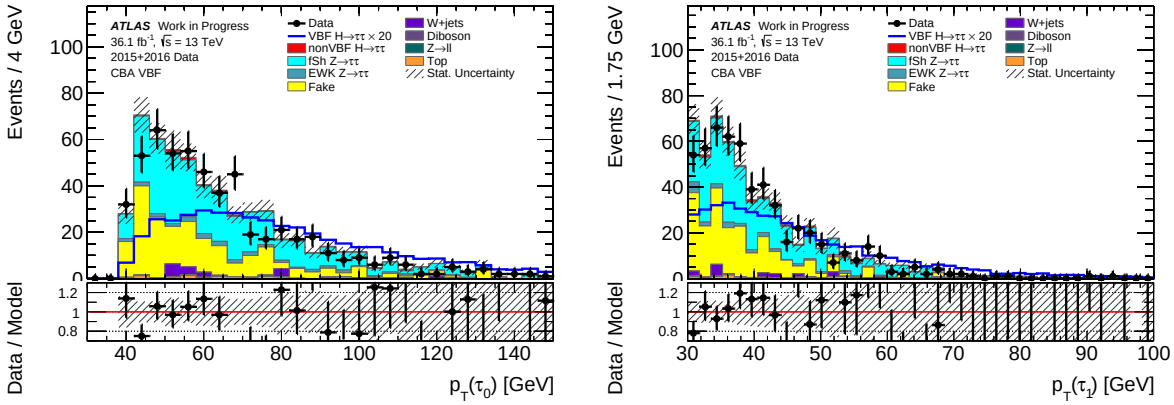

Figure C.11.: Distribution of transverse momentum p_T of the leading and subleading τ leptons in the VBF inclusive region.

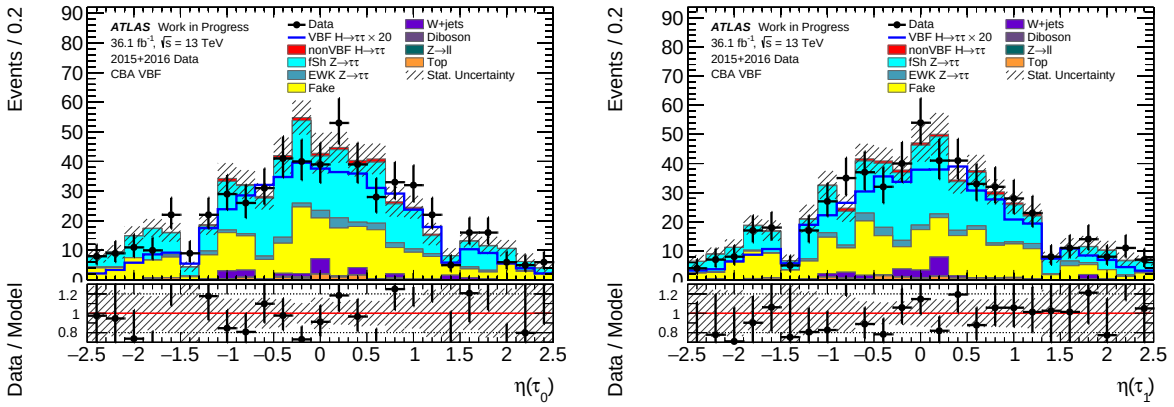

Figure C.12.: Distribution of the pseudorapidity η of the leading and subleading τ leptons in the VBF inclusive region.

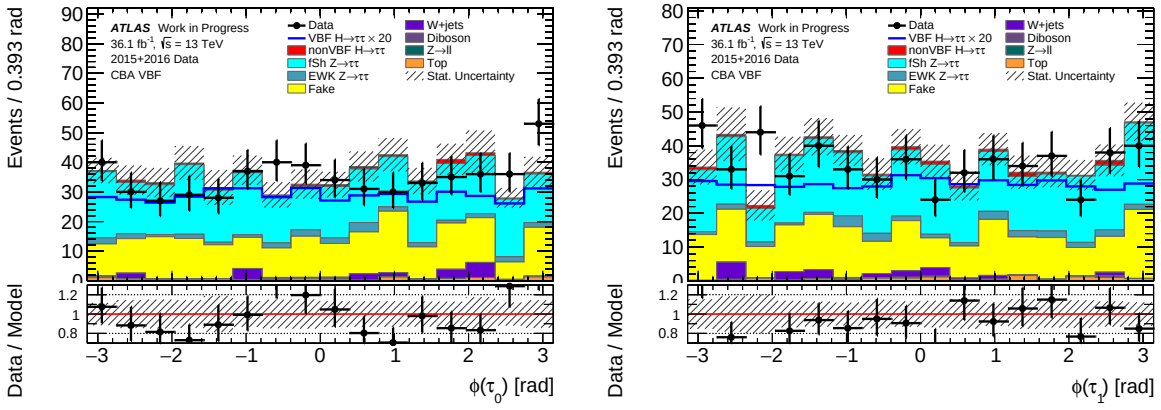

Figure C.13.: Distribution of the azimuthal angle ϕ of the leading and subleading τ leptons in the VBF inclusive region.

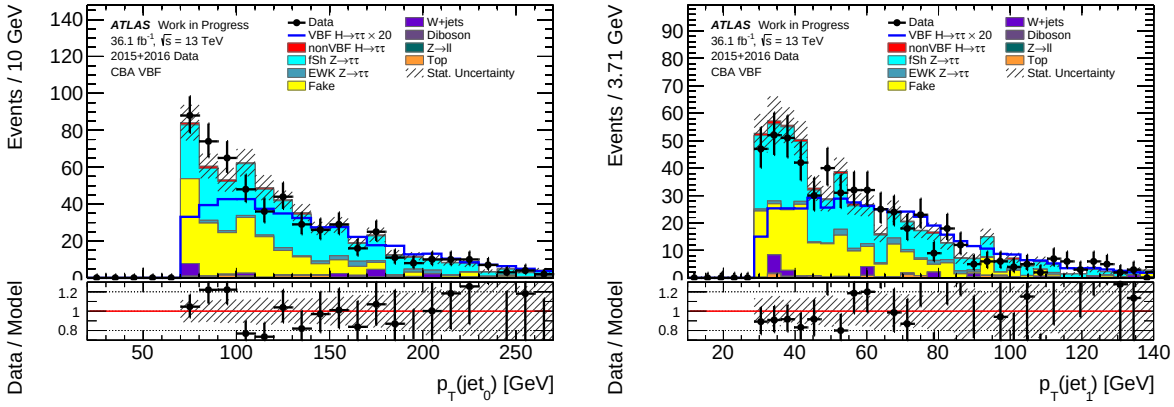

Figure C.14.: Distribution of the transverse momentum p_T of the leading and subleading jets in the VBF inclusive region.

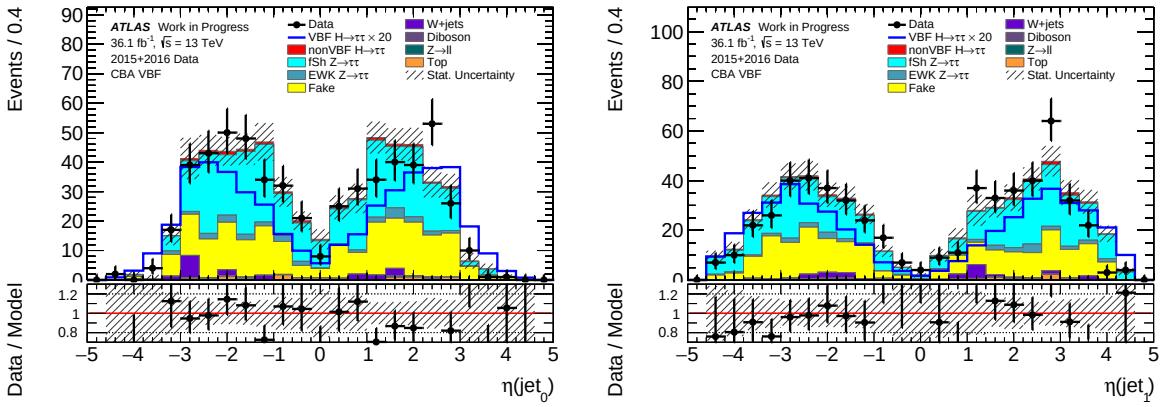

Figure C.15.: Distribution of the pseudorapidity η of the leading and subleading jets in the VBF inclusive region.

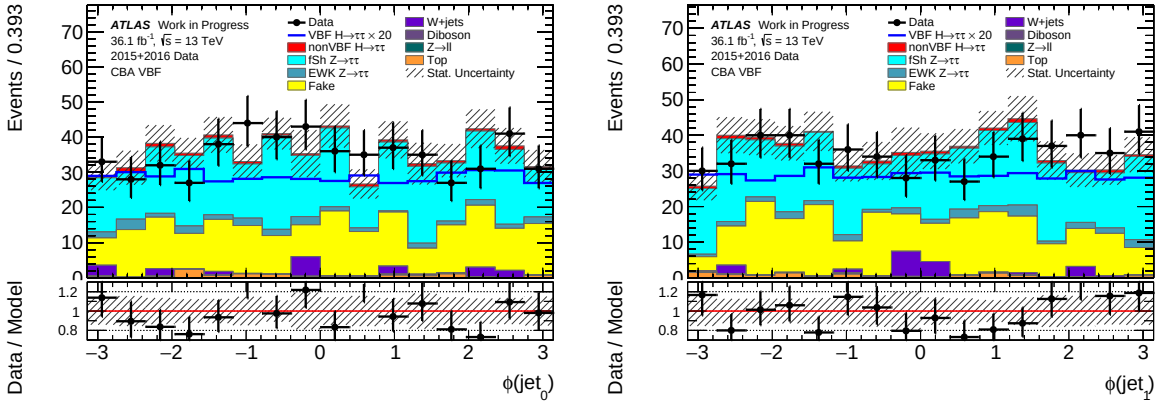

Figure C.16.: Distribution of the azimuthal angle ϕ of the leading and subleading jets in the VBF inclusive region.

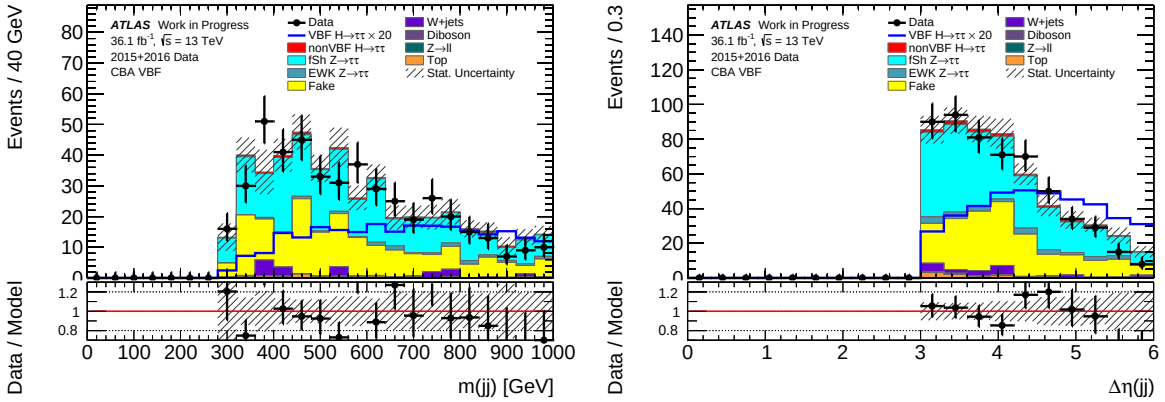

Figure C.17.: Distribution of m_{jet_0,jet_1} and $|\Delta\eta_{jet_0,jet_1}|$ in the VBF inclusive region.

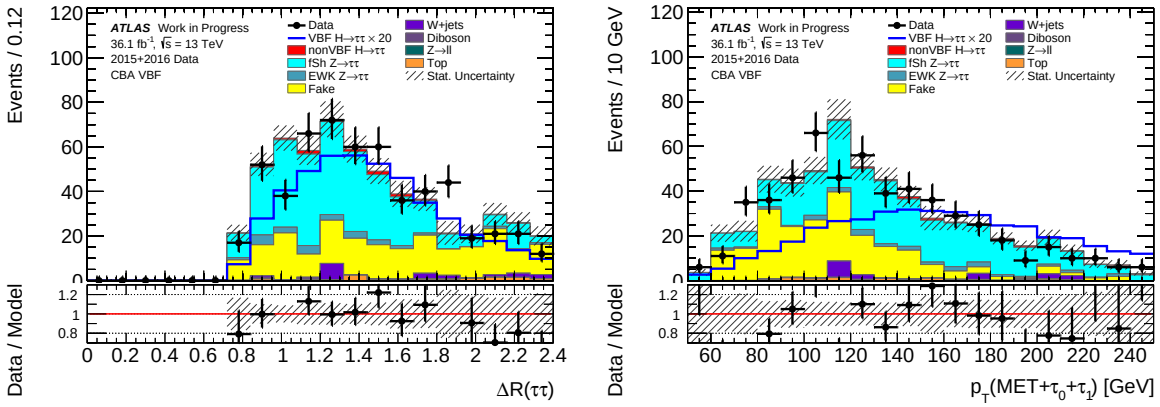

Figure C.18.: Distribution of $\Delta R_{\tau_0,\tau_1}$ and p_T^{Higgs} in the VBF inclusive region.

D. Systematic Uncertainties

D.1. List of Nuisance Parameters

A list of the systematic uncertainties which are considered in the fit and a short description is given in Table D.2. Based on the systematic uncertainties included in the $H \to \tau_{\text{had}}\tau_{\text{had}}$ SM couplings analysis (status from July 2017), the list of systematic uncertainties given in Table D.1 are not considered in the presented VBF $H \to \tau_{\text{had}}\tau_{\text{had}}$ CP analysis. In addition, no systematic uncertainties which were implemented into the SM coupling analysis after the presented VBF CP analysis results were produced, such as systematic uncertainties regarding the $\Delta\phi(\tau_0, \tau_1)$-reweighting, are considered in the fit model.

θ	description of uncertainty
pdf_higgs_[gg,gg]_Accept	acceptance changes due to PDF uncertainties
ATLAS_UE_[gg,qq]	modelling of underlying event
QCD_scale_[ggH_m12,qqH,VH]	missing higher orders in QCD corrections
theory_ztt_mur_muf_envelop	effects due to renormalization und factorization in $Z \to \tau\tau$

Table D.1.: List of NPs describing theoretical systematic uncertainties which are not considered in the presented VBF $H \to \tau_{\text{had}}\tau_{\text{had}}$ CP analysis but are included in the $H \to \tau_{\text{had}}\tau_{\text{had}}$ SM couplings analysis (status from July 2017).

θ	description of uncertainty
Forward_JVT JVT	efficiency for jet vertex tagger
JER	jet energy resolution
JES_EffectiveNP_[1-6] JES_EtaInter_Model JES_EtaInter_NonClosure JES_EtaInter_Stat JES_Flavor_Comp JES_Flavor_Resp JES_PU_OffsetMu JES_PU_OffsetNPV JES_PU_PtTerm JES_PU_Rho JES_PunchTrough	jet energy scale
MET_SoftTrk_ResoPara MET_SoftTrk_resoPara	missing transverse energy resolution
MET_SoftTrk_Scale	missing transverse energy scale
PRW_DATASF	pile-up reweighting
TAU_EFF_ELEORL_TRUEELE TAU_EFF_ELEORL_TRUEHDTAU TAU_EFF_ID_HIGHPT TAU_EFF_ID_TOTAL TAU_EFF_RECO_HIGHPT TAU_EFF_RECO_TOTAL TAU_EFF_TRIG_STATDATA[2015,2016] TAU_EFF_TRIG_STATMC[2015,2016] TAU_EFF_TRIG_SYST[2015,2016]	τ lepton reconstruction efficiency
TAU_TES_DETECTOR TAU_TES_INSITU TAU_TES_MODEL	τ lepton energy scale
LuminosityUncCombined	luminosity
BR_tautau	branching ratio $H \to \tau\tau$, $\pm 5.7\%$
NLO_EW_Higgs pdf_Higgs_[gg,qq]	missing higher orders in NLO electroweak corrections PDF parametrisation and cross section
Theo_Ztt_PDF Z_EWK_proportion	Z^0 background modelling
hh_fake_contamination hh_fake_extrapolation	fake background modelling

Table D.2.: List of dominant NPs that enter the likelihood function with short description.

D.2. Post-Fit values of the Nuisance Parameters for SM Fit

The Tables D.3 and D.4 show the post-fit yields of the NPs.

θ	post-fit value
μ	$1^{+0.76}_{-0.76}$
ATLAS_BR_tautau	$3.39e\text{-}06^{+0.99}_{-0.99}$
ATLAS_Forward_JVT	$0^{+0.99}_{-0.99}$
ATLAS_JER	$7.47e\text{-}06^{+0.63}_{-0.63}$
ATLAS_JES_EffectiveNP_1	$1.63e\text{-}05^{+0.91}_{-0.91}$
ATLAS_JES_EffectiveNP_2	$7.28e\text{-}06^{+0.96}_{-0.96}$
ATLAS_JES_EffectiveNP_3	$-1.68e\text{-}05^{+0.96}_{-0.96}$
ATLAS_JES_EffectiveNP_4	$-2.06e\text{-}06^{+0.95}_{-0.95}$
ATLAS_JES_EffectiveNP_5	$-3.13e\text{-}06^{+0.99}_{-0.99}$
ATLAS_JES_EffectiveNP_6	$-8.1e\text{-}06^{+0.98}_{-0.98}$
ATLAS_JES_EtaInter_Model	$1.67e\text{-}05^{+0.94}_{-0.94}$
ATLAS_JES_EtaInter_NonClosure	$-5.54e\text{-}06^{+0.96}_{-0.96}$
ATLAS_JES_EtaInter_Stat	$-9.41e\text{-}06^{+0.93}_{-0.93}$
ATLAS_JES_Flavor_Comp	$1.45e\text{-}05^{+0.85}_{-0.85}$
ATLAS_JES_Flavor_Resp	$1.27e\text{-}06^{+0.96}_{-0.96}$
ATLAS_JES_PU_OffsetMu	$3.61e\text{-}07^{+0.90}_{-0.90}$
ATLAS_JES_PU_OffsetNPV	$1.44e\text{-}05^{+0.97}_{-0.97}$
ATLAS_JES_PU_PtTerm	$-1.41e\text{-}05^{+0.99}_{-0.99}$
ATLAS_JES_PU_Rho	$-1.27e\text{-}05^{+0.93}_{-0.93}$
ATLAS_JES_PunchThrough	$-4.51e\text{-}08^{+0.99}_{-0.99}$
ATLAS_JVT	$0^{+0.99}_{-0.99}$
ATLAS_MET_SoftTrk_ResoPara	$-8.02e\text{-}06^{+0.82}_{-0.82}$
ATLAS_MET_SoftTrk_ResoPerp	$-6.28e\text{-}06^{+0.84}_{-0.84}$
ATLAS_MET_SoftTrk_Scale	$-8.79e\text{-}06^{+0.94}_{-0.94}$
ATLAS_PRW_DATASF	$-1.37e\text{-}05^{+0.95}_{-0.95}$
ATLAS_TAU_EFF_ELEORL_TRUEELE	$0^{+0.99}_{-0.99}$
ATLAS_TAU_EFF_ELEORL_TRUEHADTAU	$8.91e\text{-}06^{+0.99}_{-0.99}$
ATLAS_TAU_EFF_ID_HIGHPT	$-4.59e\text{-}12^{+0.99}_{-0.99}$
ATLAS_TAU_EFF_ID_TOTAL	$1.27e\text{-}05^{+0.83}_{-0.83}$
ATLAS_TAU_EFF_RECO_HIGHPT	$0^{+0.99}_{-0.99}$
ATLAS_TAU_EFF_RECO_TOTAL	$1.44e\text{-}05^{+0.95}_{-0.95}$
ATLAS_TAU_EFF_TRIG_STATDATA2015	$3.37e\text{-}07^{+0.99}_{-0.99}$
ATLAS_TAU_EFF_TRIG_STATDATA2016	$1.44e\text{-}05^{+0.98}_{-0.98}$
ATLAS_TAU_EFF_TRIG_STATMC2015	$5.88e\text{-}10^{+0.99}_{-0.99}$
ATLAS_TAU_EFF_TRIG_STATMC2016	$1.37e\text{-}05^{+0.99}_{-0.99}$
ATLAS_TAU_EFF_TRIG_SYST2015	$8.93e\text{-}10^{+0.99}_{-0.99}$
ATLAS_TAU_EFF_TRIG_SYST2016	$8.79e\text{-}06^{+0.99}_{-0.99}$
ATLAS_TAU_TES_DETECTOR	$8.13e\text{-}06^{+0.96}_{-0.96}$
ATLAS_TAU_TES_INSITU	$1.46e\text{-}05^{+0.87}_{-0.87}$
ATLAS_TAU_TES_MODEL	$2.4e\text{-}06^{+0.96}_{-0.96}$
LuminosityUncCombined	$5.27e\text{-}06^{+0.99}_{-0.99}$
NLO_EW_Higgs	$0^{+0.99}_{-0.99}$
Theo_Ztt_PDF	$1.01e\text{-}05^{+0.94}_{-0.94}$
Z_EWK_proportion	$5.77e\text{-}06^{+0.99}_{-0.99}$
hh_fake_contamination	$-2.72e\text{-}06^{+0.99}_{-0.99}$
hh_fake_extrapolation	$-2.18e\text{-}06^{+0.83}_{-0.83}$
pdf_Higgs_gg	$3.85e\text{-}06^{+0.99}_{-0.99}$
pdf_Higgs_qq	$0^{+0.99}_{-0.99}$

Table D.3.: Post-fit values in σ-units for the NPs θ considered in the final fit in the VBF subregions.

θ	post-fit value
μ	$1^{+0.90}_{-0.90}$
ATLAS_BR_tautau	$3.8e\text{-}06^{+0.99}_{-0.99}$
ATLAS_Forward_JVT	$0^{+0.99}_{-0.99}$
ATLAS_JER	$1.32e\text{-}05^{+0.86}_{-0.86}$
ATLAS_JES_EffectiveNP_1	$2.41e\text{-}05^{+0.95}_{-0.95}$
ATLAS_JES_EffectiveNP_2	$1.3e\text{-}05^{+0.98}_{-0.98}$
ATLAS_JES_EffectiveNP_3	$-2.55e\text{-}05^{+0.98}_{-0.98}$
ATLAS_JES_EffectiveNP_4	$4.45e\text{-}06^{+0.97}_{-0.97}$
ATLAS_JES_EffectiveNP_5	$-1.01e\text{-}06^{+0.99}_{-0.99}$
ATLAS_JES_EffectiveNP_6	$-1.73e\text{-}05^{+0.99}_{-0.99}$
ATLAS_JES_EtaInter_Model	$4.88e\text{-}05^{+0.97}_{-0.97}$
ATLAS_JES_EtaInter_NonClosure	$-3.61e\text{-}06^{+0.99}_{-0.99}$
ATLAS_JES_EtaInter_Stat	$-1.4e\text{-}05^{+0.96}_{-0.96}$
ATLAS_JES_Flavor_Comp	$3.1e\text{-}05^{+0.89}_{-0.89}$
ATLAS_JES_Flavor_Resp	$1.32e\text{-}05^{+0.97}_{-0.97}$
ATLAS_JES_PU_OffsetMu	$-4.28e\text{-}05^{+0.94}_{-0.94}$
ATLAS_JES_PU_OffsetNPV	$4.27e\text{-}06^{+0.99}_{-0.99}$
ATLAS_JES_PU_PtTerm	$-1.88e\text{-}05^{+0.99}_{-0.99}$
ATLAS_JES_PU_Rho	$-3.44e\text{-}05^{+0.96}_{-0.96}$
ATLAS_JES_PunchThrough	$2.63e\text{-}08^{+0.99}_{-0.99}$
ATLAS_JVT	$0^{+0.99}_{-0.99}$
ATLAS_MET_SoftTrk_ResoPara	$-6.81e\text{-}06^{+0.89}_{-0.89}$
ATLAS_MET_SoftTrk_ResoPerp	$-8.84e\text{-}06^{+0.99}_{-0.99}$
ATLAS_MET_SoftTrk_Scale	$-6.26e\text{-}06^{+0.99}_{-0.99}$
ATLAS_PRW_DATASF	$-1.38e\text{-}05^{+0.98}_{-0.98}$
ATLAS_TAU_EFF_ELEORL_TRUEELE	$0^{+0.99}_{-0.99}$
ATLAS_TAU_EFF_ELEORL_TRUEHADTAU	$9.93e\text{-}06^{+0.99}_{-0.99}$
ATLAS_TAU_EFF_ID_HIGHPT	$1.25e\text{-}09^{+0.99}_{-0.99}$
ATLAS_TAU_EFF_ID_TOTAL	$1.54e\text{-}05^{+0.86}_{-0.86}$
ATLAS_TAU_EFF_RECO_HIGHPT	$6.21e\text{-}10^{+0.99}_{-0.99}$
ATLAS_TAU_EFF_RECO_TOTAL	$1.69e\text{-}05^{+0.95}_{-0.95}$
ATLAS_TAU_EFF_TRIG_STATDATA2015	$1.87e\text{-}09^{+0.99}_{-0.99}$
ATLAS_TAU_EFF_TRIG_STATDATA2016	$2.02e\text{-}05^{+0.98}_{-0.98}$
ATLAS_TAU_EFF_TRIG_STATMC2015	$4e\text{-}10^{+0.99}_{-0.99}$
ATLAS_TAU_EFF_TRIG_STATMC2016	$1.85e\text{-}05^{+0.99}_{-0.99}$
ATLAS_TAU_EFF_TRIG_SYST2015	$2.02e\text{-}09^{+0.99}_{-0.99}$
ATLAS_TAU_EFF_TRIG_SYST2016	$1.17e\text{-}05^{+0.99}_{-0.99}$
ATLAS_TAU_TES_DETECTOR	$2.02e\text{-}05^{+0.98}_{-0.98}$
ATLAS_TAU_TES_INSITU	$1.14e\text{-}05^{+0.94}_{-0.94}$
ATLAS_TAU_TES_MODEL	$-7.61e\text{-}06^{+0.99}_{-0.99}$
LuminosityUncCombined	$5.53e\text{-}06^{+0.99}_{-0.99}$
NLO_EW_Higgs	$0^{+0.99}_{-0.99}$
Theo_Ztt_PDF	$1.39e\text{-}05^{+0.94}_{-0.94}$
Z_EWK_proportion	$6.09e\text{-}06^{+0.99}_{-0.99}$
hh_fake_contamination	$-4.71e\text{-}06^{+0.99}_{-0.99}$
hh_fake_extrapolation	$-2.59e\text{-}06^{+0.85}_{-0.85}$
pdf_Higgs_gg	$4.4e\text{-}06^{+0.99}_{-0.99}$
pdf_Higgs_qq	$0^{+0.99}_{-0.99}$

Table D.4.: Post-fit values in σ-units for the NPs θ considered in the final fit in the VBF inclusive region.

Bibliography

[1] S. Weinberg, *A Model of Leptons*, Phys. Rev. Lett. **19**, 1264 (1967)

[2] A. Salam, *Weak and Electromagnetic Interactions*, ed. Nobel Symposium No. 8 (Almqvist & Wiksell, Stockholm, 1968)

[3] S. L. Glashow, J. Iliopoulos, L. Maiani, *Weak Interactions with Lepton-Hadron Symmetry*, Phys. Rev. D **2**, 1285 (1970)

[4] H. Georgi, S. L. Glashow, *Unified Weak and Electromagnetic Interactions without Neutral Currents*, Phys. Rev. Lett. **28**, 1494 (1972)

[5] H. D. Politzer, *Reliable Perturbative Results for Strong Interactions*, Phys. Rev. Lett. **30**, 1346 (1973)

[6] H. D. Politzer, *Asymptotic Freedom: An Approach to Strong Interactions*, Phys. Rept. **14**, 129 (1974)

[7] D. J. Gross, F. Wilczek, *Asymptotically Free Gauge Theories*, Phys. Rev. D **8**, 3633 (1973)

[8] P. W. Higgs, *Broken Symmetries, Massless Particles and Gauge Fields*, Phys. Lett. **12**, 132 (1964)

[9] F. Englert, R. Brout, *Broken Symmetry and the Mass of Gauge Vector Mesons*, Phys. Rev. Lett. **13**, 321 (1964)

[10] G. S. Guralnik, C. R. Hagen, T. W. B. Kibble, *Global Conservation Laws and Massless Particles*, Phys. Rev. Lett. **13**, 585 (1964)

[11] ATLAS Collaboration, *Observation of a new particle in the search for the Standard Model Higgs boson with the ATLAS detector at the LHC*, Phys. Lett. **B716**, 1 (2012)

[12] CMS Collaboration, *Observation of a new boson at a mass of 125 GeV with the CMS experiment at the LHC*, Phys. Lett. **B716**, 30 (2012)

[13] A. D. Sakharov, *Violation of CP Invariance, c Asymmetry, and Baryon Asymmetry of the Universe*, Pisma Zh. Eksp. Teor. Fiz. **5**, 32 (1967), [Usp. Fiz. Nauk161,61(1991)]

[14] ATLAS Collaboration, *Test of CP Invariance in vector-boson fusion production of the Higgs boson using the Optimal Observable method in the ditau decay channel with the ATLAS detector*, Eur. Phys. J. **C76(12)**, 658 (2016)

[15] G. 't Hooft, *Renormalizable Lagrangians For Massive Yang-Mills Fields*, Nucl. Phys. B **35**, 167 (1971)

[16] G. 't Hooft, M. Veltmann, *Regularization And Renormalization Of Gauge Fields*, Nucl. Phys. B **44**, 189 (1972)

[17] G. 't Hooft, M. Veltmann, *Combinatorics of gauge fields*, Nucl. Phys. B **50**, 318 (1972)

[18] J. Schwinger, *On Quantum-Electrodynamics and the Magnetic Moment of the Electron*, Physical Review **73**, 416 (1948)

[19] J. Schwinger, *Quantum Electrodynamics. I. A Covariant Formulation*, Physical Review **74**, 1439 (1948)

[20] R. P. Feynman, *Space-Time Approach to Quantum Electrodynamics*, Physical Review **76**, 769 (1949)

[21] R. P. Feynman, *The Theory of Positrons*, Physical Review **76**, 749 (1949)

[22] R. P. Feynman, *Mathematical Formulation of the Quantum Theory of Electromagnetic Interaction*, Physical Review **80**, 440 (1950)

[23] N. Cabbibo, *Unitary Symmetry and Leptonic Decays*, Phys. Rev. Lett. **10**, 531 (1963)

[24] M. Kobayashi, T. Maskawa, *CP Violation in the Renormalizable Theory of Weak Interaction*, Prog. Theor. Phys. **49**, 652 (1973)

[25] A. H. G. Peter, *Dark Matter: A Brief Review*, ArXiv e-prints (2012)

[26] Supernova Search Team, *Observational evidence from supernovae for an accelerating universe and a cosmological constant*, Astron. J. **116**, 1009 (1998)

[27] F. Jegerlehner, *The hierarchy problem of the electroweak Standard Model revisited*, arxiv E-prints (2013)

[28] E. Noether, *Invariante Variationsprobleme*, Nachr. D. König. Gesellsch. D. Wiss. Zu Göttingen, Math-phys. Klasse, S.235-257 (1918)

[29] Planck Collaboration, *Planck 2015 results. XIII. Cosmological parameters*, Astron. Astrophys. **594**, A13 (2016)

[30] A. G. Cohen, A. De Rujula, S. L. Glashow, *A Matter - antimatter universe?*, Astrophys. J. **495**, 539 (1998)

[31] A. D. Sakharov, *Baryon asymmetry of the universe*, Sov. Phys. Usp. **34**, 417 (1991)

[32] R. H. Cyburt, B. D. Fields, K. A. Olive, *Primordial nucleosynthesis in light of WMAP*, Phys. Lett. **B567**, 227 (2003)

[33] C. Wu, E. Ambler, R. Hayward, *Experimental Test of Parity Conservation in Beta Decay*, Physical Review. 105 (4): 1413–1415. (1957)

[34] J. H. Christenson, J. W. Cronin, V. L. Fitch, R. Turlay, *Evidence for the* 2π *Decay of the* K_2^0 *Meson*, Phys. Rev. Lett. **13**, 138 (1964)

[35] Belle Collaboration, *Observation of Large CP Violation in the Neutral B Meson System*, Phys. Rev. Lett. **87**, 091802 (2001)

[36] ATLAS Collaboration, *Measurements of Higgs boson production and couplings in diboson final states with the ATLAS detector at the LHC*, Phys. Lett. **B726**, 88 (2013), [Erratum: Phys. Lett.B734,406(2014)]

[37] ATLAS Collaboration, *Study of the spin and parity of the Higgs boson in diboson decays with the ATLAS detector*, Eur. Phys. J. **C75(10)**, 476 (2015), [Erratum: Eur. Phys. J.C76,no.3,152(2016)]

[38] ATLAS Collaboration, *Evidence for the spin-0 nature of the Higgs boson using ATLAS data*, Physics Letters B **726(1–3)**, 120 (2013)

[39] CMS Collaboration, *Study of the Mass and Spin-Parity of the Higgs Boson Candidate Via Its Decays to Z Boson Pairs*, Phys. Rev. Lett. **110(8)**, 081803 (2013)

[40] C. N. Yang, *Selection Rules for the Dematerialization of a Particle into Two Photons*, Phys. Rev. **77**, 242 (1950)

[41] J. Beringer, et al. (Particle Data Group), *Review of Particle Physics*, Phys. Rev. D **86**, 010001 (2012)

[42] *Evidence for Higgs Boson Decays to the $\tau^+\tau^-$ Final State with the ATLAS Detector*, Technical Report ATLAS-CONF-2013-108, CERN, Geneva (2013)

[43] ATLAS Collaboration, *Identification and energy calibration of hadronically decaying tau leptons with the ATLAS experiment in pp collisions at $\sqrt{s}$=8 TeV*, Eur. Phys. J. **C75(7)**, 303 (2015)

[44] A. V. Manohar, *Effective field theories*, Lect. Notes Phys. **479**, 311 (1997)

[45] J. R. Andersen, et al. (LHC Higgs Cross Section Working Group), *Handbook of LHC Higgs Cross Sections: 3. Higgs Properties* (2013)

[46] B. Grzadkowski, M. Iskrzynski, M. Misiak, J. Rosiek, *Dimension-Six Terms in the Standard Model Lagrangian*, JHEP **10**, 085 (2010)

[47] C. G. Krause, *Higgs Effective Field Theories - Systematics and Applications*, Ph.D. thesis, Munich U. (2016)

[48] H. Belusca-Maito, *Effective Higgs Lagrangian and Constraints on Higgs Couplings*, Journees des Jeunes Chercheurs (2014)

[49] V. Hankele, G. Klamke, D. Zeppenfeld, T. Figy, *Anomalous Higgs boson couplings in vector boson fusion at the CERN LHC*, Phys. Rev. **D74**, 095001 (2006)

[50] OPAL Collaboration, *Measurement of W boson polarizations and CP violating triple gauge couplings from W+W- production at LEP*, Eur. Phys. J. **C19**, 229 (2001)

[51] P. Achard, et al. (L3), *Search for anomalous couplings in the Higgs sector at LEP*, Phys. Lett. **B589**, 89 (2004)

[52] F. de Campos, et al., *Probing Higgs couplings in ee->3gamma*, Physics Letters B **389(1)**, 93 (1996)

[53] M. Diehl, O. Nachtmann, *Anomalous three gauge couplings in e+ e- —> W+ W- and 'optimal' strategies for their measurement*, Eur. Phys. J. **C1**, 177 (1998)

[54] D. Atwood, A. Soni, *Analysis for magnetic moment and electric dipole moment form factors of the top quark via $e^+e^-\to tt^-$*, Phys. Rev. D **45**, 2405 (1992)

[55] M. Davier, L. Duflot, F. Le Diberder, A. Rouge, *The Optimal method for the measurement of tau polarization*, Phys. Lett. **B306**, 411 (1993)

[56] C. Schillo, *Search for the Standard Model Higgs Boson and Test of CP Invariance in Vector-Boson Fusion Production of the Higgs Boson in the Fully Leptonic $H\to\tau\tau\to ll4\nu$ Final State in Proton-Proton Collisions with the ATLAS Detector at the LHC*, Ph.D. thesis, Universität Freiburg (2016)

[57] OPAL Collboration, *W^+W^- production and triple gauge boson couplings at LEP energies up to 183-GeV*, Eur. Phys. J. **C8**, 191 (1999)

[58] H. Voss, N. Wermes, I. Brock, *Messung der Drei-Eichboson-Kopplungen in $W^+W^-\to q\bar{q}l\overline{\nu}_l$ Ereignissen mit optimalen Observablen bei OPAL*, Ph.D. thesis, Universität Bonn (2000)

[59] M. Diehl, O. Nachtmann, F. Nagel, *Triple gauge couplings in polarized e- e+ —> W- W+ and their measurement using optimal observables*, Eur. Phys. J. **C27**, 375 (2003)

[60] A. Loesle, *Study of CP Properties of the Higgs Boson produced in Gluon Fusion with two Jets in Proton - Proton Collisions at $\sqrt{s} = 8$ TeV with the ATLAS Experiment*, Master's thesis, Albert-Ludiwgs-Universtitaet Freiburg (2015)

[61] M. Spangenberg, *Test of CP-invariance in Vector Boson Fusion production of the Higgs boson using the Optimal Observable method in the di-tau decay channel with the ATLAS Detector*, Ph.D. thesis, University of Warkwick (2016)

[62] V. Croft, *A Tauists Hunt for Higgles*, Ph.D. thesis, Radboud Universiteit Nijmegen (2017)

[63] R. P. Feynman, *Very High-Energy Collisions of Hadrons*, Phys. Rev. Lett. **23**, 1415 (1969)

[64] J. D. Bjorken, E. A. Paschos, *Inelastic Electron-Proton and γ-Proton Scattering and the Structure of the Nucleon*, Phys. Rev. **185**, 1975 (1969)

[65] A. D. Martin, W. J. Stirling, R. S. Thorne, G. Watt, *Parton distributions for the LHC*, Eur. Phys. J. **C63**, 189 (2009)

[66] S. D. Drell, T.-M. Yan, *Partons and their applications at high energies*, Annals of Physics **66(2)**, 578 (1971)

[67] ATLAS Collaboration, *Performance of pile-up mitigation techniques for jets in pp collisions at $\sqrt{s} = 8$ TeV using the ATLAS detector*, Eur. Phys. J. **C76(11)**, 581 (2016)

[68] L. R. Evans, *The Large Hadron Collider (LHC)*, IEEE Trans. Appl. Supercond. **14**, 147 (2004)

[69] ALICE Collaboration, *The ALICE experiment at the CERN LHC*, JINST **3**, S08002 (2008)

[70] ATLAS Collaboration, *The ATLAS Experiment at the CERN Large Hadron Collider*, JINST **3**, S08003 (2008)

[71] CMS Collaboration, *The CMS Experiment at the CERN LHC*, JINST **3**, S08004 (2008)

[72] LHCb Collaboration, *The LHCb Detector at the LHC*, JINST **3**, S08005 (2008)

[73] ATLAS Collaboration, *ATLAS Insertable B-Layer Technical Design Report*, Technical Report CERN-LHCC-2010-013. ATLAS-TDR-19 (2010)

[74] F. Hugging, *The ATLAS Pixel Detector*, IEEE Transactions on Nuclear Science **53**, 1732 (2006)

[75] ATLAS Collaboration, *Operation and performance of the ATLAS semiconductor tracker*, JINST **9**, P08009 (2014)

[76] ATLAS Collaboration, *The ATLAS Inner Detector commissioning and calibration*, Eur. Phys. J. **C70**, 787 (2010)

[77] P. Francavilla, *The ATLAS Tile Hadronic Calorimeter performance at the LHC*, Journal of Physics: Conference Series **404(1)**, 012007 (2012)

[78] M. Elsing, T. Schoerner-Sadenius, *Configuration of the ATLAS Trigger System*, ArXiv Physics e-prints (2003)

[79] ATLAS Collaboration, *The Run-2 ATLAS Trigger System*, Technical Report ATL-DAQ-PROC-2016-003, CERN, Geneva (2016)

[80] ATLAS Collaboration, *The ATLAS Simulation Infrastructure*, Eur. Phys. J. **C70**, 823 (2010)

[81] P. Nason, *A New method for combining NLO QCD with shower Monte Carlo algorithms*, JHEP **11**, 040 (2004)

[82] S. Frixione, P. Nason, C. Oleari, *Matching NLO QCD computations with Parton Shower simulations: the POWHEG method*, JHEP **11**, 070 (2007)

[83] S. Alioli, P. Nason, C. Oleari, E. Re, *A general framework for implementing NLO calculations in shower Monte Carlo programs: the POWHEG BOX*, JHEP **06**, 043 (2010)

[84] E. Bagnaschi, G. Degrassi, P. Slavich, A. Vicini, *Higgs production via gluon fusion in the POWHEG approach in the SM and in the MSSM*, JHEP **02**, 088 (2012)

[85] T. Sjostrand, S. Mrenna, P. Z. Skands, *A Brief Introduction to PYTHIA 8.1*, Comput. Phys. Commun. **178**, 852 (2008)

[86] T. Gleisberg, S. Hoeche, F. Krauss, A. Schaelicke, S. Schumann, J. Winter, *Event generator for LHC*, Nucl. Instrum. Methods A **559** (2006)

[87] T. Gleisberg, S. Hoeche, F. Krauss, A. Schälicke, S. Schumann, J. Winter, *SHERPA 1.α, a proof-of-concept version*, J. High Energy Phys. **0402**, 056 (2004)

[88] T. Gleisberg, S. Hoeche, F. Krauss, A. Schälicke, S. Schumann, G. Soff, J. Winter, *Predictions for multi-particle final states with SHERPA*, Talk at Physics at LHC, Vienna, Austria, 2004, (2004)

[89] T. Gleisberg, S. Hoeche, F. Krauss, M. Schonherr, S. Schumann, F. Siegert, J. Winter, *Event generation with SHERPA 1.1*, JHEP **02**, 007 (2009)

[90] S. Agostinelli, et al. (GEANT4), *GEANT4: A Simulation toolkit*, Nucl. Instrum. Meth. **A506**, 250 (2003)

[91] M. Cacciari, G. P. Salam, G. Soyez, *The Anti-k(t) jet clustering algorithm*, JHEP **04**, 063 (2008)

[92] A. Elagin, P. Murat, A. Pranko, A. Safonov, *A New Mass Reconstruction Technique for Resonances Decaying to di-tau*, Nucl. Instrum. Meth. **A654**, 481 (2011)

[93] ATLAS Collaboration, *Expected Performance of the ATLAS Experiment - Detector, Trigger and Physics* (2009)

[94] D. Zanzi, *Search for the Standard Model Higgs Boson in Hadronic $\tau^+\tau^-$ Decays with the ATLAS Detector*, Ph.D. thesis, Munich, Max Planck Inst. (2014-05-05)

[95] ATLAS Collaboration, *Performance of Missing Transverse Momentum Reconstruction in Proton-Proton Collisions at 7 TeV with ATLAS*, Eur. Phys. J. **C72**, 1844 (2012)

[96] L. Breiman, J. H. Friedman, R. A. Olshen, C. J. Stone, *Classification and Regression Trees*, Chapman & Hall, New York (1984)

[97] ATLAS Collaboration, *Measurement of the tau lepton reconstruction and identification performance in the ATLAS experiment using pp collisions at* $\sqrt{s} = 13$ *TeV*, Technical Report ATLAS-CONF-2017-029, CERN, Geneva (2017)

[98] ATLAS Collaboration, *Measurement of the* $H \to \tau^+\tau^-$ *cross-section in* 13 *TeV Collisions with the ATLAS Detector*, Technical Report ATL-COM-PHYS-2017-446, CERN, Geneva (2017)

[99] S. Jadach, J. H. Kühn, Z. Was, *TAUOLA: a library of Monte Carlo programs to simulate decays of polarized* τ *leptons*, Comput. Phys. Commun. **64(CERN-TH-5856-90)**, 275 (1990)

[100] D. de Florian, et al. (LHC Higgs Cross Section Working Group), *Handbook of LHC Higgs Cross Sections: 4. Deciphering the Nature of the Higgs Sector* (2016)

[101] S. Catani, L. Cieri, G. Ferrera, D. de Florian, M. Grazzini, *Vector boson production at hadron colliders: a fully exclusive QCD calculation at NNLO*, Phys. Rev. Lett. **103**, 082001 (2009)

[102] A. Murrone, *Study of the use of Optimal Observables for the Higgs Boson CP determination in the vector boson fusion process*, Master's thesis, Universita degli studi di Milano (2015)

[103] G. Cowan, K. Cranmer, E. Gross, O. Vitells, *Asymptotic formulae for likelihood-based tests of new physics*, Eur. Phys. J. **C71**, 1554 (2011), [Erratum: Eur. Phys. J.C73,2501(2013)]

[104] M. Ciccolini, A. Denner, S. Dittmaier, *Strong and electroweak corrections to the production of Higgs + 2jets via weak interactions at the LHC*, Phys. Rev. Lett. **99**, 161803 (2007)

[105] M. Ciccolini, A. Denner, S. Dittmaier, *Electroweak and QCD corrections to Higgs production via vector-boson fusion at the LHC*, Phys. Rev. **D77**, 013002 (2008)

[106] A. Denner, S. Dittmaier, S. Kallweit, A. Muck, *Electroweak corrections to Higgs-strahlung off W/Z bosons at the Tevatron and the LHC with HAWK*, JHEP **03**, 075 (2012)

[107] A. Denner, S. Dittmaier, S. Kallweit, A. Mück, *HAWK 2.0: A Monte Carlo program for Higgs production in vector-boson fusion and Higgs strahlung at hadron colliders*, Comput. Phys. Commun. **195**, 161 (2015)

[108] K. Arnold, et al., *VBFNLO: A Parton level Monte Carlo for processes with electroweak bosons*, Comput. Phys. Commun. **180**, 1661 (2009)

[109] J. Alwall, M. Herquet, F. Maltoni, O. Mattelaer, T. Stelzer, *MadGraph 5 : Going Beyond*, JHEP **06**, 128 (2011)

[110] S. Ördek, *Investigation of the CP Nature of the Higgs Boson in VBF $H \to \tau\tau$ Events at $\sqrt{s} = 13$ TeV*, Master's thesis, Georg-August-Universität Göttingen (2016)

[111] C. Patrignani, et al., *Review of Particle Physics*, Chin. Phys. **C40(10)** (2016)

[112] L. D'Errico, P. Richardson, *A Positive-Weight Next-to-Leading-Order Monte Carlo Simulation of Deep Inelastic Scattering and Higgs Boson Production via Vector Boson Fusion in Herwig++*, Eur. Phys. J. **C72**, 2042 (2012)

[113] P. Artoisenet, et al., *A framework for Higgs characterisation*, JHEP **11**, 043 (2013)

[114] J. Neyman, *Outline of a Theory of Statistical Estimation Based on the Classical Theory of Probability*, Philosophical Transactions of the Royal Society of London Series A **236**, 333 (1937)

[115] ATLAS Collaboration, *Observation and measurement of Higgs boson decays to WW^* with the ATLAS detector*, Phys. Rev. **D92(1)**, 012006 (2015)

[116] *Forward Jet Vertex Tagging: A new technique for the identification and rejection of forward pileup jets*, Technical Report ATL-PHYS-PUB-2015-034, CERN, Geneva (2015)

[117] ATLAS Collaboration, *Jet energy scale measurements and their systematic uncertainties in proton-proton collisions at $\sqrt{s} = 13$ TeV with the ATLAS detector*, Phys. Rev. **D96(7)**, 072002 (2017)

[118] ATLAS collaboration, *Jet Calibration and Systematic Uncertainties for Jets Reconstructed in the ATLAS Detector at* $\sqrt{s} = 13$ *TeV*, Technical Report ATL-PHYS-PUB-2015-015, CERN, Geneva (2015)

[119] ATLAS Collaboration, *Measurement of the luminosity with the new LUCID-2 detector in 2015*, Technical Report ATL-COM-FWD-2016-008, CERN, Geneva (2016)

[120] ATLAS Collaboration, *Luminosity determination in pp collisions at* $\sqrt{s} = 8$ *TeV using the ATLAS detector at the LHC*, Eur. Phys. J. **C76(12)**, 653 (2016)

Erklärung nach §17(9) der Prüfungsordnung für den Bachelor-Studiengang Physik und den Master-Studiengang Physik an der Universität Göttingen:

Hiermit erkläre ich, dass ich diese Abschlussarbeit selbständig verfasst habe, keine anderen als die angegebenen Quellen und Hilfsmittel benutzt habe und alle Stellen, die wörtlich oder sinngemäß aus veröffentlichten Schriften entnommen wurden, als solche kenntlich gemacht habe.
Darüberhinaus erkläre ich, dass diese Abschlussarbeit nicht, auch nicht auszugsweise, im Rahmen einer nichtbestandenen Prüfung an dieser oder einer anderen Hochschule eingereicht wurde.

Göttingen, den 3. Mai 2018

(Arthur Linß)